STUDY OF $B_s \to \mu^+\mu^-$ AND $B^+ \to K^{*+}\mu^+\mu^-$ USING CMS DATA AT 7/8 TEV

By

Niladribihari Sahoo

PHYS11201004012

National Institute of Science Education and Research

Bhubaneswar

A thesis submitted to the

Board of Studies in Physical Sciences

In partial fulfillment of requirements

For the Degree of

DOCTOR OF PHILOSOPHY

of

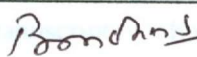**HOMI BHABHA NATIONAL INSTITUTE**

November, 2017

Homi Bhabha National Institute

Recommendations of the Viva Voce Board
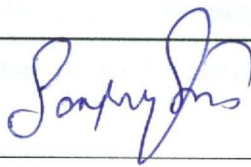
As members of the Viva Voce Board, we certify that we have read the dissertation prepared by Niladribihari Sahoo entitled "STUDY OF $B_s \to \mu^+\mu^-$ AND $B^+ \to K^{*+}\mu^+\mu^-$ USING CMS DATA AT 7/8 TEV" and recommend that it may be accepted as fulfilling the dissertation requirement for the Degree of Doctor of Philosophy.

Chairman: Prof. Bedangadas Mohanty	*Bondhus*	Date: 29/11/2017
Convener: Dr. Sanjay Kumar Swain	*Sanjay Jms*	Date: 29/11/2017
Examiner: Prof. Basanta Kumar Nandi	*Bland*	Date: 29/11/2017
Member 1: Dr. Subhasish Basak	*Subhasish Basak*	Date: 29/11/17
Member 2: Dr. Prolay Kumar Mal	*PMal*	Date: Nov 29, 2017
Member 3: Dr. Aruna Kumar Nayak	*Aruna Kumar Nayak*	Date: 29·11·2017
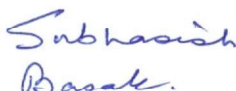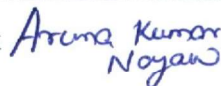
Final approval and acceptance of this dissertation is contingent upon the candidate's submission of the final copies of the dissertation to HBNI.

I hereby certify that I have read this dissertation prepared under my direction and recommend that it may be accepted as fulfilling the dissertation requirement.

Date: 29/11/2017

Place: NISER

(Dr. Sanjay Kumar Swain)

STATEMENT BY AUTHOR

This dissertation has been submitted in partial fulfillment of requirements for an advanced degree at Homi Bhabha National Institute (HBNI) and is deposited in the Library to be made available to borrowers under rules of the HBNI.

Brief quotations from this dissertation are allowable without special permission, provided that accurate acknowledgement of source is made. Requests for permission for extended quotation from or reproduction of this manuscript in whole or in part may be granted by the Competent Authority of HBNI when in his or her judgement the proposed use of the material is in the interests of scholarship. In all other instances, however, permission must be obtained from the author.

Niladribihari Sahoo

DECLARATION

I, Niladribihari Sahoo, hereby declare that the investigation presented in the thesis has been carried out by me. The work is original and has not been submitted earlier as a whole or in part for a degree/diploma at this or any other Institution/University.

Niladribihari Sahoo

List of Publications arising from the thesis

Journal

- **Published**

  1. S. Chatrchyan *et al.* [CMS Collaboration], *"Measurement of the $B_s \to \mu^+\mu^-$ branching fraction and search for $B^0 \to \mu^+\mu^-$ with the CMS Experiment"*, Phys. Rev. Lett. **111**, 101804 (2013)

  2. V. Khachatryan *et al.* [CMS & LHCb collaboration], *"Observation of the rare $B_s^0 \to \mu^+\mu^-$ decay from the combined analysis of CMS and LHCb data"*, Nature **522**, 68–72 (2015)

- **Under Review**

  1. CMS collaboration, *"Angular Analysis for $B^+ \to K^{*+}\mu^+\mu^-$ at $\sqrt{s} = 8$ TeV"*

Conferences

1. "Rare B decays at CMS", 9th International Workshop on the CKM Unitarity Triangle (CKM2016), Mumbai, 28 Nov - 3 Dec 2016, PoS(CKM2016)054

Workshops & Schools

1. Workshop on Physics at the LHC Run II, SINP, Kolkata, 26-28 August 2016

2. Workshop on Upgrade of the CMS Calorimeter, TIFR, Mumbai, 23-24 November 2015

3. 2014 Asia-Europe-Pacific School of High Energy Physics (AEPSHEP2014), Puri, 4-17 November 2014

4. CMS Data Analysis School, SINP, Kolkata, 7-11 November 2013

5. 8th CERN-FERMILAB Hadron Collider Physics Summer School, CERN, 28 Aug
   - 6 Sep 2013

Niladribihari Sahoo

*Dedicated
to
My Family and Friends*

ACKNOWLEDGEMENTS

topics. I also thank all my juniors for all excellent discussions. Thanks to Ankit, Ashu, Manoj, Tapas, Tapan, Sushri, Sanjima, Niru, Koushik, Protick, Sukanta, Chandi, Biswa, Tapu and many others (I can't list them all, it'll be a long list) for making my days at NISER pleasant and enjoyable.

Finally, I offer my respect and gratitude to my parents, brother and sister-in-law for being the guiding hands when I needed them the most. Their love, support and blessings are my greatest resources of inspirations and will be in future too. I dedicate this thesis to my family and friends.

Contents

SYNOPSIS

In the Standard Model(SM) of particle physics, matter is made up of two elementary particles: quarks and leptons collectively called *fermions*. Both quarks and leptons come in six flavors and can be arranged into three families(generations) differing by their masses and other quantum numbers. The elementary particles of the first generation constitute the matter in our universe. The quarks of the first family (up and down quarks) form the building blocks of the atomic nuclei. Together with electron they constitute the atoms. In nature we have never found quarks separated from each other. Five of the six known quarks always form composite particles called *hadrons*. The most massive known elementary particle,i.e. the top quark decays weakly on a time scale which is very short for the top quark to form a hadron. In the third generation, the partner of top quark is the bottom quark. Hadrons containing a bottom quark are the heaviest that are experimentally studied. One of the goals of the b hadron system or *B*-physics is to test the consistency of the standard model as well as to study the New Physics(NP) effects. There are two ways to search for new physics beyond the standard model. First, the *direct* search in which the new heavy particles beyond the standard model have to be produced in the collider experiments although the production cross-section is too small. This gives a direct indication of physics processes beyond the standard model. Second, the *indirect* search in which the observables of interest (for example branching ratio) of a standard model process is measured in the experiment. Any significant deviation of the experimental measurement from the SM prediction would be a hint for NP. Rare B decays (BF is too small, of order 10^{-8}-10^{-9}) provide a unique opportunity to probe physics processes beyond standard model. In my thesis work, I have worked on two such rare decay processes which can give a hint about NP.

The first part of my thesis is based upon the search for a typical rarest decay where B_s, a pseudo-scalar meson, decays to a muon pair with data collected at a centre of mass

energy 7 and 8TeV in CMS detector at Large Hadron Collider(LHC), CERN, Switzerland. This decay has a highly suppressed rate in the standard model (SM) since it involves a $b \rightarrow s$ transition. In SM, these flavor changing neutral current (FCNC) transitions are forbidden at tree level, and only proceed through higher order diagrams, described by electroweak penguin and box diagrams at the loop level. These decays are also helicity suppressed in the SM. This opens up the possibility for contributions from the non-SM particles. In the SM, this rare FCNC decay has a small branching fraction [1,2]. There are several extensions of the SM which predict the enhancements to the branching fractions for these rare decays [3–6]. The decay rates can also be suppressed for specific choices of model parameters [7]. This thesis presents the first measurement of branching fraction of the $B_s \rightarrow \mu^+\mu^-$ decay in CMS corresponding to full LHC data in 2011 and 2012 for proton-proton collisions at centre of mass energy 7 and 8TeV respectively. The result is in agreement with the expectations from the SM and the recent measurements of the LHCb collaboration. My contribution to this analysis was mainly the study of fake rate, rare background contribution, data-MC comparisons and few systematic studies which are briefly described below.

The particles other than muons (i.e. π, K, p) may be wrongly identified as muons in the detector. The main sources of misidentification are (i) *hadron punch-through* in which the hadron shower remnants penetrate through the calorimeter and reach the muon system, (ii) *hadron decay-in-flight* as pion decays to muon and (anti)neutrino where (anti)neutrino goes undetected through the detector and the left out particle is the muon. It is possible to measure these contributions with resonances decaying in kaons, pions and protons, such as $K_s \rightarrow \pi^+\pi^-$, $\Lambda \rightarrow p\pi^-$ and $\phi \rightarrow K^+K^-$. With such samples, it's easy to measure the muon misidentification as the fraction of tracks identified as reconstructed muons. In this study, the fake rate is measured as function of transverse momentum (p_T) of track in both barrel and end cap region. The rate ranges from $(0.5 - 1.3) \times 10^{-3}$, $(0.8 - 2.2) \times 10^{-3}$ and $(0.4 - 1.5) \times 10^{-3}$ for pions, kaons and protons respectively depending on whether the particle is in the barrel or end cap region and the particle's transverse momentum.

The signal topology for this decay is simple: two muons originating from a common vertex. However, there are various background sources which can mimic like a signal event. That's why understanding the background is very important to this kind of analysis. In this study, the contribution from rare single B decays have been studied. These backgrounds can be further divided into (i) *peaking* and (ii) *non-peaking* backgrounds. The *peaking* background includes decays like $B_s \to K^+K^-$ and $B^0 \to K^+\pi^-$ where these sources yield a B mass peak like the signal but slightly shifted towards the lower mass region because of wrong mass hypothesis of the particles. In case of the *non-peaking* background, one (soft) particle is missing in the reconstruction. These are decays like $\Lambda_b \to p\mu\nu$. They don't yield a mass peak rather they have an upper bound in the spectrum depending upon the mother particle's mass. This study is done both in barrel and end cap regions respectively.

The analysis is validated by looking at few selection cut variables' distributions by comparing data with simulation in both normalisation $B^+ \to J/\psi K^+$ and control $B_s \to J/\psi\phi$ channels. All the distributions are sideband subtracted. They showed good agreement for each variable.

Many possible sources of systematic uncertainties are checked and estimated for the final results of the analysis. The uncertainty on the acceptance of the signal has contributions from the detector response and also from the uncertainty of production mechanisms that influence the phase space distribution of muons and thus resulting in the overall geometrical acceptance. Particularly the contribution from production mechanism is studied here. The three main QCD processes responsible for b pair production are (i) *pair creation*, (ii) *flavor excitation* and (iii) *gluon splitting*. An estimation on the impact of the different production mechanism is performed by studying the acceptance as a function of the PYTHIA b pair production η range for each of the three production mechanisms. The maximum variation of the acceptance ratio between the signal and normalisation is taken as the estimation of systematic uncertainty, 3.5% for the barrel and 5.0% percentage for

the end cap categories.

The second part of the thesis presents the angular analysis of flavor changing current (FCNC) decay $B^+ \to K^{*+}\mu^+\mu^-$ which is basically $b \to sl^+l^-$ decay. In this decay, B^+ decays to a muon pair and $K^*(892)$ meson which subsequently decays to K_s and a charged pion. Two important observables of interest for this decay are the Forward-backward Asymmetry of the muons, A_{FB}, and the longitudinal polarization fraction of $K^*(892)$, F_L. To better understand this, these observables are measured as a function of the dimuon invariant mass squared (q^2) and compared to SM predictions. New Physics may modify any of these quantities [8–24] relative to their SM values [8], [25–31]. Deviations from the SM may indicate the new physics phenomena. This thesis presents the measurement of A_{FB} and F_L for $B^+ \to K^{*+}\mu^+\mu^-$ decay in several q^2 bins using data collected from proton-proton collisions at a centre of mass energy 8TeV by the CMS experiment at LHC, CERN. In this analysis, I solely contributed towards the event selection(optimization of variables) and systematic studies whereas partially towards the angular fitting procedure which are briefly mentioned below.

The data contains both signal and background events. The aim is to pick up the signal events and throw the background events as much as possible. For that, we have to pick up those variables where the discrimination of signal and background distributions can be easily observed. Then we optimize those variables to find out the best optimized value for each variable by maximizing the Figure Of Merit (FOM) value. This study is completely data-driven.

The main goal of this analysis is to measure the forward-backward asymmetry of the muons, A_{FB}, and the fraction of longitudinal polarization of $K^*(892)$, F_L as function of dimuon mass squared (q^2). The above two interesting observables are extracted from un-binned fits by using an extended maximum likelihood estimator. The probability density function (PDF) consists of components from signal, peaking and combinatorial background. The fits are performed in stages during which some components are determined

from simulation whereas the rest of the components are determined directly from data. And finally the 3D fit is performed in data to obtain the physical observables A_{FB} and F_L in several q^2 bins.

The final measurement for physical observables A_{FB}, F_L should include systematic errors in addition to statistical errors. That's why different possible sources of systematic uncertainties are studied for this analysis. For example, how much the final physical observable (central) values are changed if we change the signal and background shapes in comparison to the original values extracted from the final 3D fitting. The discrepancy is considered as the systematic uncertainty due to that particular source. Similarly, other systematic uncertainty contributions are calculated for different possible sources.

Bibliography

[1] A. J. Buras *et al.*, Eur. Phys. J. C **72**, 2172 (2012).

[2] K. De Bruyn *et al.*, Phys. Rev. Lett. **109**, 041801 (2012).

[3] J. R. Ellis *et al.*, J. High Energy Phys. **05** (2006) 063.

[4] S. Davidson and S. Descotes-Genon, J. High Energy Phys. **11** (2010) 073.

[5] S. R. Choudhury *et al.*, Int. J. Mod. Phys. A **21**, 2617 (2006).

[6] J. K. Parry, Nucl. Phys. B760, **38** (2007).

[7] J. R. Ellis, J. S. Lee, and A. Pilaftsis, Phys. Rev. D **76**, 115011 (2007).

[8] W. Altmannshofer *et al.*, J. High Energy Phys. **01** (2009) 019.

[9] D. Melikhov, N. Nikitin, and S. Simula, Phys. Lett. B **442** (1998) 381.

[10] A. Ali, P. Ball, L. T. Handoko, and G. Hiller, Phys. Rev. D **61**, 074024 (2000).

[11] Q.-S. Yan, C.-S. Huang, W. Liao, and S.-H. Zhu, Phys. Rev. D **62**, 094023 (2000).

[12] G. Buchalla, G. Hiller, and G. Isidori, Phys. Rev. D **63**, 014015 (2000).

[13] T. Feldmann and J. Matias, J. High Energy Phys. **01** (2003) 074.

[14] G. Hiller and F. Kruger, Phys. Rev. D **69**, 074020 (2004).

[15] F. Kruger and J. Matias, Phys. Rev. D **71**, 094009 (2005).

[16] W.-S. Hou, A. Hovhannisyan, and N. Mahajan, Phys. Rev. D **77**, 014016 (2008).

[17] U. Egede *et al.*, J. High Energy Phys. **11** (2008) 032.

[18] T. Hurth, G. Isidori, J. F. Kamenik, and F. Mescia, Nucl. Phys. B **808** (2009) 326.

[19] A. K. Alok et al., J. High Energy Phys. **02** (2010) 053.

[20] A. K. Alok et al., J. High Energy Phys. **11** (2011) 121.

[21] Q. Chang, X.-Q. Li, and Y.-D. Yang, J. High Energy Phys. **04** (2010) 052.

[22] S. Descotes-Genon, D. Ghosh, J. Matias, and M. Ramon, J. High Energy Phys. **06** (2011) 099.

[23] J. Matias, F. Mescia, M. Ramon, and J. Virto, J. High Energy Phys. **04** (2012) 104.

[24] S. Descotes-Genon, J. Matias, M. Ramon, and J. Virto, J. High Energy Phys. **01** (2013) 048.

[25] C. Bobeth, G. Hiller, and D. van Dyk, J. High Energy Phys. **07** (2010) 098.

[26] C. Bobeth, G. Hiller, D. van Dyk, and C. Wacker, J. High Energy Phys. **01** (2012) 107.

[27] C. Bobeth, G. Hiller, and D. van Dyk, Phys. Rev. D **87**, 034016 (2012).

[28] A. Ali, G. Kramer, and G. Zhu, Eur. Phys. J. C **47**, 625 (2006).

[29] W. Altmannshofer, P. Paradisi, and D. M. Straub, J. High Energy Phys. **04** (2012) 008.

[30] S. Jager and J. Martin Camalich, J. High Energy Phys. **05** (2013) 043.

[31] S. Descotes-Genon, T. Hurth, J. Matias, and J. Virto, J. High Energy Phys. **05** (2013) 137.

List of Figures

List of Tables

Chapter 1

Prologue

1.1 Introduction

From the start of mankind, human beings are inquisitive and always seeking to understand the mystery of the world around them. This intrinsic curiosity leads to categorization among the human beings. With commonality and organization comes rules. In this way, order is brought to the chaos. However, it is when the rules are broken that the mystery is solved.

There had been many experiments performed by mankind to review the mystery,e.g, in 1911, an alpha particle did not pass straight through a gold foil. The unexpected behavior led Rutherford to think that atoms existed in distinct sections: a very small positive central charge with a negative outer region. The experimental outcome did not match prediction, i.e. it broke the rules. In the study of physics and science in general, a set of rules that well-describes all known experimental results and also makes testable predictions is called a theory. When new evidence is found that doesn't fit with the rules, the theory must be altered to accommodate the new facts. This openness to new information allows science to adapt while keeping a rigorous requirement on the integrity of new information and continuously challenging mankind to attempt to break the rules.

1.2 The Standard Model

The goal of elementary particle physics is to identify the basic constituents of matter and to understand their properties and interactions. From the past studies we know that protons and neutrons are not fundamental particles as electrons, since they consist of point like particles namely quarks. These constituent quarks are held together by the exchange of gluons. Collectively these quarks and gluons are called "partons". The Standard Model (SM) was proposed by Glashow, Salam and Weinberg to explain the fundamental structure of matter as well as the fundamental interactions [1]. The gravitational interaction, however, has not yet been incorporated in this model. According to this model, all the elementary particles are divided into three groups namely, Quarks, Leptons and Gauge Bosons [2]. All the quarks and leptons are spin half particles, i.e., fermions and the gauge bosons are the mediator of the interaction between quarks and leptons. All together they represent three of the four fundamental forces in nature: the strong force, the weak force, the electromagnetic force and the gravitational force. The six different gauge bosons are: the massless photons (γ) and gluons (g), the massive $W^{\pm}$ and Z^0 bosons and gravitons. The SM also predicts the existence of Higgs boson (*H*) which has been discovered very recently [3,4]. The leptons are divided into three generations: (i) the electron and electron neutrino, (ii) the muon and muon neutrino and (iii) the tau and tau neutrino. The leptons interact among each other via the electromagnetic and the weak interaction. There are also three generations of quarks in the SM, namely, (i) up (u), down (d) quarks, (ii) charm (c), strange (s) and (iii) top (t) and bottom (b) quarks. Figure 1.1 shows all the fundamental particles in the SM.

1.3 The Particle Interactions

The quarks, leptons and their anti-particles combine to make up all the visible matter in the universe. Most of the everyday world is made from the up and down quark and the electron. For example, the proton is a combination of two up quarks and a down quark
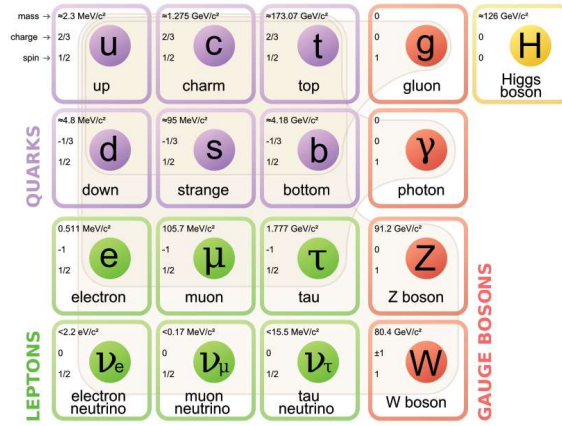
Figure 1.1: The Standard Model describes particle interactions using 12 fundamental particles, the quarks and leptons, and 4 force carriers.

(*uud*). Neutrons are a *ddu*. Protons, neutrons and electrons combine to form atoms. Atoms combine to form molecules and compounds, which in turn combine to form the paper or computer screen this is written on. A group of bound quarks or anti-quarks is referred to as a hadron. A baryon is a bound state of three quarks (qqq) or anti-quarks ($\bar{q}\bar{q}\bar{q}$)) into a particle. Quark anti-quark pairings($q\bar{q}$) create a meson. Bound states of quarks are held together by the strong force, which is mediated by gluons (g). The SM has 8 varieties of gluons, which carry a color/anti-color combination. Only color neutral particles can't bind together. The color charge values are red (R), blue (B), and green (G). Anti-quarks have anti-color values of cyan ($\bar{R}$), yellow ($\bar{B}$) and magenta ($\bar{G}$). A baryon is the color singlet with the wavefunction $\frac{1}{\sqrt{6}}[RBG + BGR + GRB - RGB - BRG - GBR]$. Mesons have a neutral color wavefunction of $\frac{1}{3}[R\bar{R} + B\bar{B} + G\bar{G}]$. Quarks only bind to each other because of the color charge, however, they interact with other particles through the other bosons. The strong interaction is a short range force that only couples to quarks, anti- quarks and gluons since the gluons are self interacting due to color charge. The strong force is the glue that holds together hadrons. The photon (γ) mediates electromagnetic interactions. Since the photon is massless and not self interacting, the electromagnetic force has infinite range. The $W^{\pm}$ and Z bosons, which are massive, mediate weak interactions and couple to all fermions. The weak force is of shorter range and weaker than the strong force due

3

to the exchange of the heavy vector bosons. Properties of the force carriers are shown in Table 1.1.

Interaction	Carriers	Mass (GeV)	Charge	Range (m)
Gravitational	Gravitons	0	0	∞
Weak	$W^{\pm}, Z$	80.4, 91.2	$\pm 1, 0$	10^{-17}-10^{-16}
Electromagnetic	Photons (γ)	0	0	∞
Strong	Gluons (g)	0	0	10^{-15}

Table 1.1: The four fundamental forces and its carriers.

The weak interaction is responsible for flavor change, changing one type of quark or lepton to another [1]. For example, it is responsible for radioactive decay, in which a neutron changes to a proton emitting an electron and an electron anti-neutrino, ($udd \rightarrow uud + e + \bar{\nu}_e$). The weak force is particular in its coupling to particles of certain helicity. Helicity is a particle property related to spin and momentum. If the spin and direction a particle is traveling is aligned, the particle is said to be right-handed. If these qualities are opposite, the particle is left-handed. The weak force preferentially couples to left-handed fermions and right-handed anti-fermions. The weak force is also needed to have flavor changing neutral current (FCNC) processes. FCNC decays change the flavor of the fermion without changing the charge. These types of processes are forbidden at first order in the SM but are possible through higher-order processes such as box and penguin diagrams at loop level.

1.4   Beyond the standard model

The Standard Model is a well defined theory. It predicted the mass and properties of the $W^{\pm}$ and Z bosons as part of the unification of the electromagnetic and weak forces. These particles were discovered at CERN by UA1 collaboration [5], [6] and UA2 collaborations [7], [8]. It also predicted the top quark, which was discovered at Fermilab in 1995 [9]. Despite the remarkable strength of the SM, it is incomplete. The incompleteness of the SM is related to the many free parameters in the theory: masses, coupling

constants, flavor mixing matrix elements, etc. For example, the SM assumes neutrinos are massless. However, neutrinos oscillate between flavors so they must have mass, even if it is small. The SM allows for matter/anti-matter asymmetry through the quark mixing matrix, but the measured values of these parameters are not large enough to account for the asymmetry seen in the universe. The Higgs boson is another area where the SM is not completely confirmed. The SM calls for a scalar which couples to particles to give them mass. This particle is an excitation of the field that is required to have massive bosons for the weak force. A Higgs boson consistent with the SM has been observed at the Large Hadron Collider in CERN, but further testing is needed to determine if the particle is in fact "the" Higgs boson. In an attempt to improve upon the SM to solve these issues, many formulations Beyond the Standard Model (BSM) have been drafted by theorists. Since these models must still explain the experimental results that are seen, they have testable properties. New particles are often predicted in BSM scenarios. This is one way to test the models and search for new physics. Another method to test both the SM and BSM scenarios is to compare predicted and observed properties. Upto today, no BSM predictions have been observed.

The $B_s \to \mu^+\mu^-$ branching fraction (BF) is one of the most promising channels for the search of new physics. Similarly observables like A_{FB} and F_L in $B^+ \to K^{*+}\mu^+\mu^-$ decay can also be measured in angular analysis to compare with SM predictions and give a hint for New Physics (NP).

1.5 $B_s \to \mu^+\mu^-$ search motivation

The B_s meson is composed of a $\bar{b}s$ quark pair, and the $\bar{B}_s$ is a $\bar{s}b$ combination. The B_s can interchange to a $\bar{B}_s$ and back, a process called mixing, through double W exchange. The mass eigenstates of the meson are the light $(B_s + \bar{B}_s)$ and heavy $(B_s - \bar{B}_s)$ combination, which have different lifetimes. The decay $B_s \to \mu^+\mu^-$ proceeds by a FCNC process illustrated by the Feynman diagram in Figure 1.2. In the Standard Model, FCNC decays

are heavily suppressed. $B_s \rightarrow \mu^+\mu^-$ is further suppressed by the helicity requirements of the final state. Branching fractions are a measurement of the rate at which a particular event/decay occurs. The SM branching fraction is predicted to be $(3.57 \pm 0.30) \times 10^{-9}$ [10, 11]. where the branching ratio has been corrected to account for the different lifetimes of the heavy and light mass eigenstates. In BSM physics, the decay of the B_s can proceed through new particles in the W loop. In the Minimal Supersymmetric Standard Model (MSSM), for example, the decay can proceed with a light Higgs boson, as shown in Figure 1.2. Any new particle that can enter in the loops can have a significant effect on the branching fraction. Many BSM scenarios, including MSSM, predict substantial enhancement as well as supression to the branching fraction of the $B_s \rightarrow \mu^+\mu^-$ [12–16].
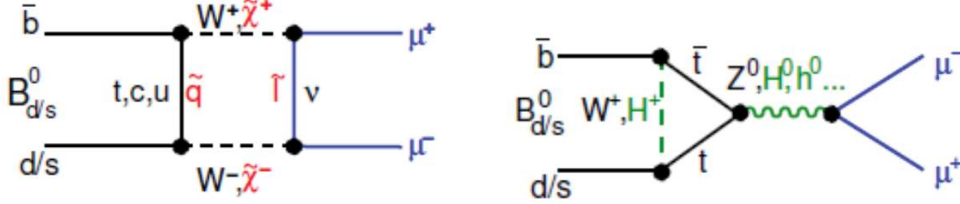
Figure 1.2: Illustration of the rare decays $B_{s(d)} \rightarrow \mu^+\mu^-$. In the SM, these decays proceed through $W^\pm$ and Z^0 bosons in a box diagram (left) and Z-penguin (right) interactions. The box diagram is suppressed by a factor of $m_W^2/m_t^2 \approx 0.2$ with respect to the Z-penguin diagram. In SM extensions (*e.g.*, in the MSSM) new particles (*e.g.*, charginos $\widetilde{\chi}^\pm$, Higgs bosons and supersymmetric partners of the quarks and leptons) can contribute to the process and thereby can increase the expected branching fraction by orders of magnitude.

Measuring the branching fraction of $B_s \rightarrow \mu^+\mu^-$ allows limits to be placed on the physics models. The results from other experiments have already excluded some of the models. Thus, accurately measuring $B_s \rightarrow \mu^+\mu^-$ BF is an excellent way to look for new physics. This thesis represents the first measurement of $B_s \rightarrow \mu^+\mu^-$ BF using the full Run1 data collected by CMS detector at CERN.

1.6 $B^+ \rightarrow K^{*+}\mu^+\mu^-$ angular analysis motivation

Like $B_s \rightarrow \mu^+\mu^-$ decay, the $B^+ \rightarrow K^{*+}\mu^+\mu^-$ is also a rare decay. This decay also proceeds by the FCNC process as illustrated by the Feynman diagram in Figure 1.3. Two important observables of interest for this decay are the Forward-backward Asymmetry of the muons, A_{FB}, and the longitudinal polarization fraction of $K^*(892)$, F_L. To have a better understanding, these observables are measured as a function of the dimuon invariant mass squared (q^2) and compared to SM predictions. New Physics may modify any of these quantities relative to their SM values. Deviations from the SM may indicate the new physics phenomena. This thesis presents the measurement of A_{FB} and F_L for this rare decay in several q^2 bins using data collected at 8 TeV centre of mass energy by CMS detector.
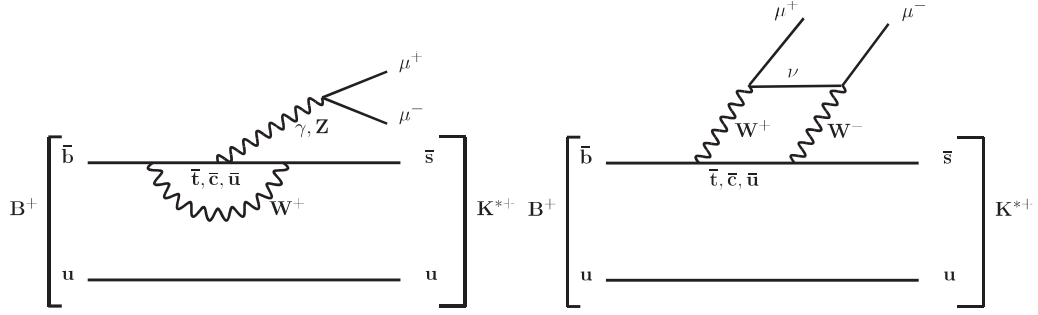
Figure 1.3: Standard Model Feynman diagrams for the decay $B^+ \rightarrow K^{*+}\mu^+\mu^-$. The first one is the penguin diagram (left) whereas the second is the box diagram (right).

Chapter 2

The CMS Experiment at LHC

2.1 Introduction

CERN (European Organization for Nuclear Research) is the world's largest center for research in particle physics. It is an international laboratory founded in 1954 and is located on the French-Swiss border near Geneva. It provides suitable infrastructure and scientific instruments such as high-energy particle accelerators and detectors to the particle physicists around the globe. The most notable among them is the Large Hadron Collider (LHC), the highest energy proton-proton collider which houses four gigantic particle detectors. This chapter dwells on the LHC and assorted experiments.

2.2 The Large Hadron Collider

The LHC at CERN is the largest and highest energy particle accelerator ever built to carry out the particle physics research. It is a two-ring-superconducting hadron accelerator and collider installed within an existing tunnel of 26.7 km circumference at a depth ranging from 50 to 150 m underground, where the LEP collider was operated earlier between 1989 and 2000 [17]. The discovery of new physics requires both high energy and high intensity

beams. The number of events produced per second in LHC collisions is

$$N = \sigma \times L \tag{2.1}$$

where σ is production cross section of the event and L is the luminosity delivered by the LHC machine. The luminosity depends on the beam parameters and is given by:

$$L = \frac{\gamma f k_B N_p^2 F}{4\pi \epsilon_n \beta^\star} , \tag{2.2}$$

where γ is the Lorentz factor, f is the revolution frequency, k_B is the number of bunches per beam, N_p is the number of protons per bunch, ϵ_n is the normalized transverse emittance, $\beta^\star$ is the beta function at the interaction point (IP), and F is the geometric luminosity reduction factor due to the crossing angle at IP and given by:

$$F = \left[1 + \left(\frac{\theta_c \sigma_z}{2\sigma^\star} \right)^2 \right]^{-1/2} , \tag{2.3}$$

where θ_c is the crossing angle at the IP, σ_z the RMS bunch length, and $\sigma^\star$ the transverse RMS beam size at the IP. The above expression assumes round beams, with $\sigma_z \ll \beta$, and with equal beam parameters for both beams.

The LHC has been designed to provide proton-proton (pp) collisions with center-of-mass energy $\sqrt{s} = 14$ TeV with a peak luminosity of $10^{34}\mathrm{cm}^{-2}\mathrm{s}^{-1}$ and lead-lead (Pb-Pb) collisions with $\sqrt{s} = 5.2$ TeV with peak luminosity $10^{27}\mathrm{cm}^{-2}\mathrm{s}^{-1}$. An overview of the LHC design parameters is given in Table 2.2. The nominal magnitude of the center-of-mass energy of pp collision is substantially higher than those corresponding to the previous generation of accelerators such as Tevatron at Fermilab which operated at $\sqrt{s} = 1.96$ TeV. Thus, the LHC will allow us to probe unexplored physics ranging from the origin of mass to the search for physics beyond the SM. These nominal values were achieved when the Run2 data taking started in 2015 with center-of-mass energy $\sqrt{s} = 13$ TeV after Long Shutdown (LS1). In 2009, the LHC collided pp with $\sqrt{s} = 1.18$ TeV while during 2011

Quantity	Value	Unit
Centre-of-mass (COM) collision energy	14	TeV
Luminosity	10^{34}	$cm^{-2}s^{-1}$
Number of bunches per beam	2828	-
Number of protons per bunch	1.15×10^{11}	-
Bunch spacing (time between bunches)	25	ns
Number of superconducting magnets	1232	-
Operating temperature of the magnets	2	°K
Magnetic field	8.33	T

Table 2.1: The LHC designed parameters.

and 2012 it was operating at $\sqrt{s} = 7$ TeV and 8 TeV, respectively.

The proton beams colliding at LHC are not continuous, rather separated into bunches having a large number of protons in each bunch. The superconducting magnets keep the protons on their circular track. A pre-accelerator chain speeds up the protons before they are finally injected into the LHC main ring. The protons are first accelerated by a linear accelerator (LINAC2) by the Proton Synchrotron (PS), then they are injected at the Super Proton Synchrotron (SPS) where they reach an energy of 450 GeV. Before filling the LHC with protons, 24 cycles from the SPS are required. A schematic overview of the LHC accelerator complex is shown in Figure 2.1.

2.2.1   LHC Detectors

The LHC collisions take place at four different points. The four major particle detectors namely ALICE [18], ATLAS [19], CMS [20] and LHCb [21] are installed in the caverns at these collision points. LHCf and TOTEM are the two additional, smaller experiments installed in the caverns of ATLAS and CMS, respectively. Besides CMS (Compact Muon Solenoid) experiment, which will be described in a greater detail on the next section, the other experiments have also a wider physics program, and are based on similar or complementary technologies. The location and collision points of these detectors are schematically shown in Figure 2.2.
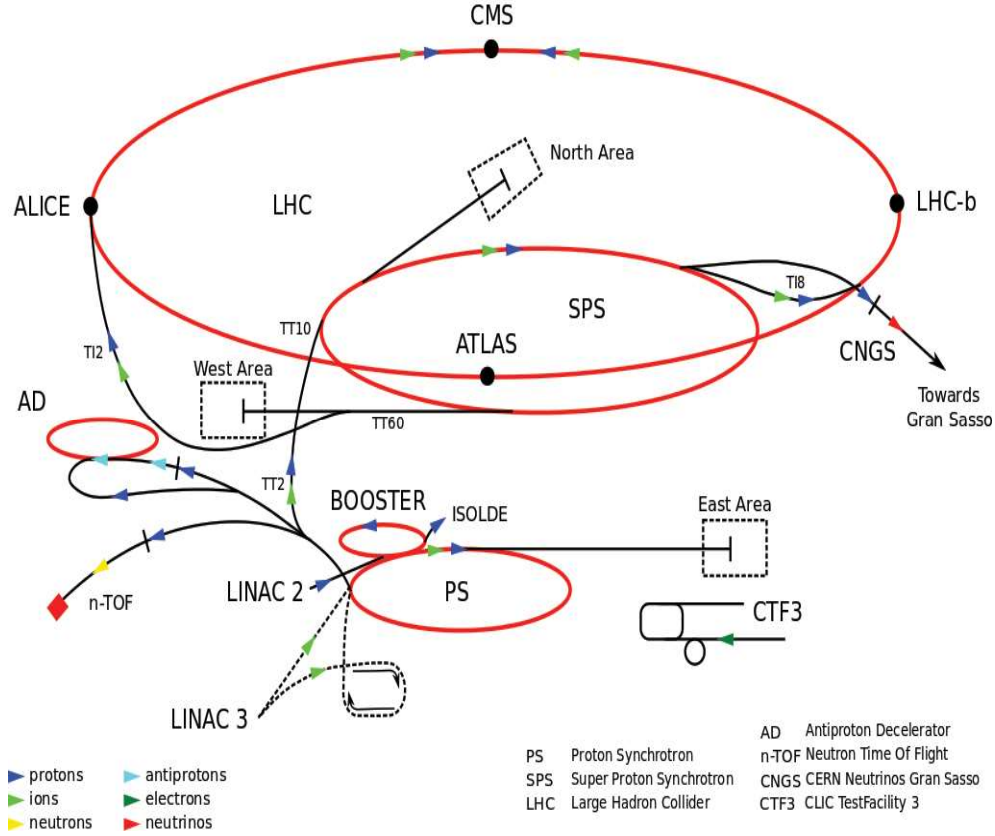
Figure 2.1: A schematic overview of the CERN accelerator complex, showing the large LHC ring, its four major experiments and the smaller accelerator facilities.

2.3 The CMS Experiment

The Compact Muon Solenoid (CMS) experiment [20] is one of the two general purpose experiments located at the Point 5 of LHC. It is designed to investigate a broad range of physics starting with the precision measurement of SM parameters to the search of the Higgs boson, the search for supersymmetric particles, extra spatial dimensions and dark matter candidates. Although it has the similar physics goals as the ATLAS experiment, it uses different technology and has a different magnet system.

2.3.1 Detector Overview

The CMS detector is 28.7 m long with a diameter of 15 m and a weight of 14 Kilotons, making it smaller but heavier than ATLAS. The main design features of the detector are its

Figure 2.2: Different collision points at the LHC accelerator

muon detector, which contributes to the goal of excellent performance in muon detection, the fully silicon-based inner tracker, the PbWO$_4$ crystal electromagnetic calorimeter, and the hadronic calorimeter inside the magnetic coil [22, 23].

The CMS detector is built around a huge solenoid magnet. This takes the form of a cylindrical coil of superconducting cable that generates a magnetic field of 3.8 Tesla, about 100,000 times that of the earth. The field is confined by a steel yoke that forms the bulk of the detector's weight. An unusual feature of the CMS detector is that instead of being built in-situ like the other giant detectors of the LHC experiments, it was constructed in 15 sections at the ground level before being lowered into an underground cavern near the Point 5.

A more detailed description of CMS detector with its individual detector components is given in the following sections and shown in Figure 2.3. A transverse slice of the CMS

detector with how particles interact with its various components are shown in Figure 2.4.
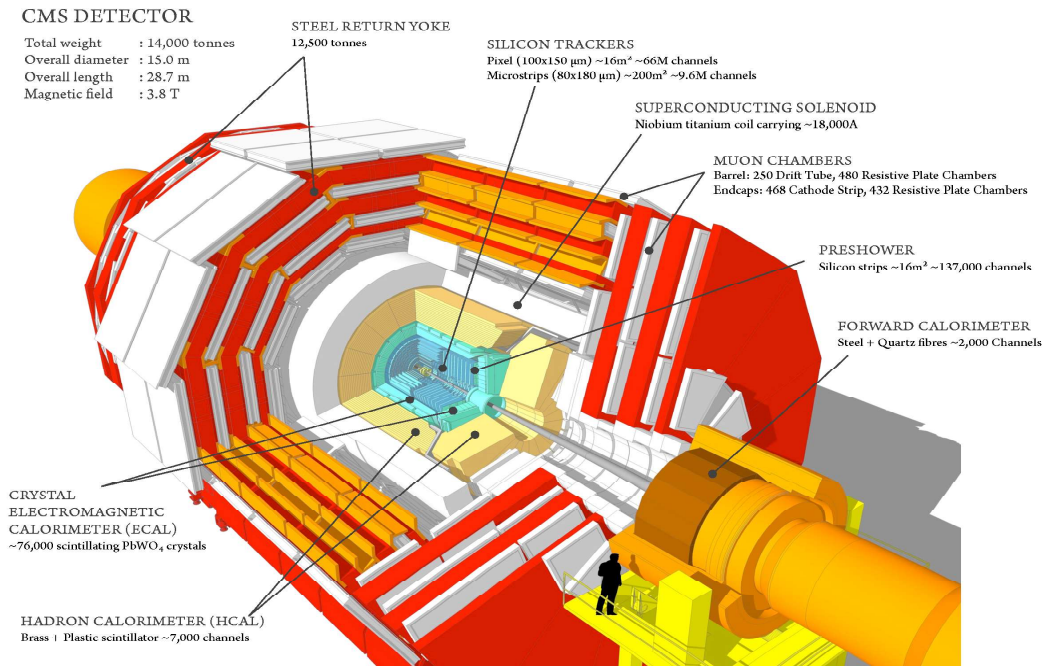
Figure 2.3: A sectional view of the CMS detector. The LHC beams travel in opposite directions along the central axis of the CMS cylinder colliding at the middle of the CMS detector.

2.3.2 The CMS Coordinate System

The CMS detector uses a right-handed cartesian coordinate system with different axes pointing as below:

1. X-axis: Points inwards to the centre of the LHC ring, perpendicular to the beam axis.

2. Y-axis: Points upwards to the surface, perpendicular to the beam axis.

3. Z-axis: Points along the beam pipe in the westward direction.

Here the Z-axis is parallel to the beam pipe in anticlockwise direction, and the X and Y-axis span a perpendicular to the beam pipe. In a spherical coordinate system, the azimuthal angle ϕ is measured from the X-axis in the XY plane, and the radial coordinate

13
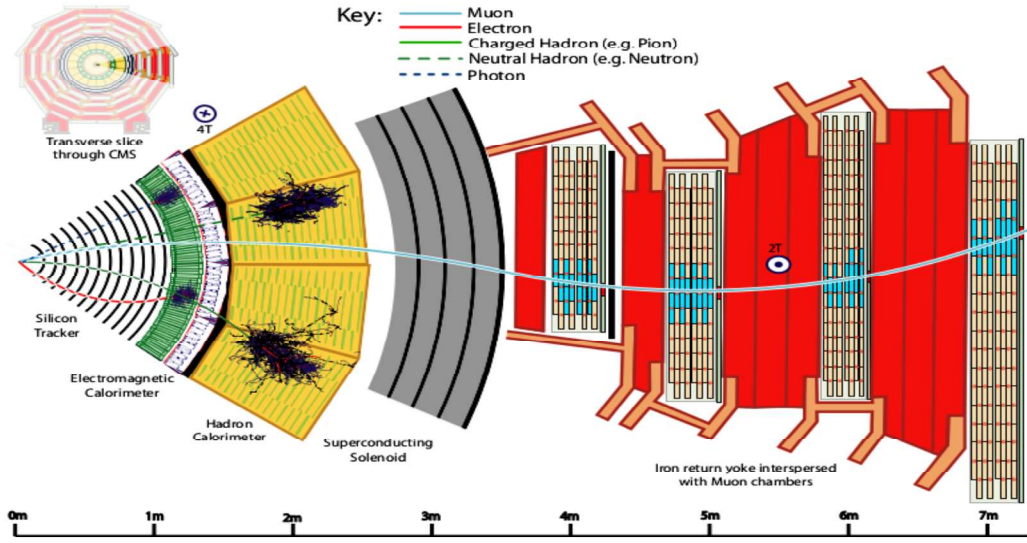
Figure 2.4: A transverse slice of the CMS detector showing its components, particle tracks, and how the various components detect different types of particles.

in this plane is denoted by r. The polar angle θ is defined in the rz plane while the pseudorapidity is denoted by η. The momentum component transverse to the beam direction, denoted by p_T, is calculated from the X and Y-components and the transverse energy is defined as $E_T = E \sin\theta$.

Rapidity and Pseudorapidity: Rapidity is a common quantity used in high energy physics and defined as:

$$y = \frac{1}{2} \ln\left(\frac{E + p_z c}{E - p_z c}\right) \tag{2.4}$$

Where p_z is the momentum component along the beam axis. In hadron collider experiments the particle flux is nearly constant as a function of rapidity. Pseudorapidity is identical to rapidity in the limit $m \to 0$. It has an advantage of being independent of the mass of a particle, only depending on the polar angle θ.

$$\eta = -\ln\left(\tan\frac{\theta}{2}\right) \tag{2.5}$$

A common quantity in CMS used for measuring the distance between two objects is ΔR

14

and defined as $\Delta R = \sqrt{\Delta\eta^2 + \Delta\phi^2}$.

2.3.3 The Superconducting Solenoid

The most striking feature of CMS is the object that gives the detector its name, the solenoid. A superconducting solenoid magnet with a maximum field of 3.8 T provides a large bending power to the high-energy charged particles enabling a precision measurement of their momenta in the tracking detectors. The magnetic coil is 13 m long, has an inner diameter of 6 m, and accommodates the tracking and a major part of the calorimeter detectors. With these dimensions the CMS solenoid is the largest superconducting magnet ever built. The magnetic flux is returned through a 10 Kilotons iron yoke in which the muon detector chambers are integrated. The CMS solenoid was fully tested and commissioned at the surface of experimental hall during 2006 [22, 23].

2.3.4 The Tracker

The CMS tracking system is designed to meet two important goals: (a) to provide a precise and efficient trajectory measurement for charged particles emanating from LHC collisions, and (b) to provide a precise reconstruction of the resulting secondary vertices. The CMS tracker comprises two types of silicon layers: silicon pixel detectors and silicon strip detectors, and it covers an acceptance of $|\eta| < 2.5$.

2.3.4.1 Silicon Pixel Detector

It is the closest sub-detector to the beam pipe. Its configuration allows to reach a 15 μm spatial resolution. Such high accuracy is essential in the reconstruction of high momentum particles namely muons, electrons and charged hadrons, as well as the secondary vertex from relatively long-lived particles like bottom (b) and charm (c) hadrons and tau (τ) leptons.

15

2.3.4.2 Silicon Strip Detector

The silicon strip tracker is the outer layers of the tracker, and it has a length of 5.4 m and a radius of 1.1 m. It is made up of single-sided silicon microstrip sensors. There are 10 layers in the barrel region and 9 disks at each endcap resulting in a minimum of 12 measurement points per charged track over a wide range of pseudorapidity. The expected hit resolution for the silicon strip tracker is $\sigma_{r\phi} = 10 - 60\,\mu m$ and $\sigma_{rz} = 500\,\mu m$. Combining these numbers, the expected CMS tracking resolution ranges from 0.015 mm for $|\eta| < 1.6$ up to 0.06 mm for $|\eta| < 2.5$. So, a muon with a p_T of 100 GeV/c can be measured with an accuracy of 1.5 for $|\eta| < 1.6$.

2.3.5   The Electromagnetic Calorimeter

The electromagnetic calorimeter (ECAL) measures the energy and direction of the particles such as electrons, positrons and photons. The CMS ECAL is composed of approximately 80,000 Lead Tungstate ($PbWO_4$) crystals. When a high energy electron or photon passes through the $PbWO_4$ crystal, it produces a shower of electrons, positrons and photons. The scintillation light from this shower is amplified and collected by an avalanche photodiode in the barrel region or by a vacuum phototriode in the two endcap regions. $PbWO_4$ crystals are used because of their radiation tolerance and light response. Further they have a high density (8.28 g/cm^3), an extremely short radiation length of 0.89 cm and a very small Moliere radius (2.2 cm). The geometry of the crystals is designed to utilize these characteristics, with typical sizes being 22× 22 mm at the front face, 26× 26 mm at the rear face and 230 mm in length. So most of the particles interact somewhere along the crystal length (traversing roughly 26 radiation lengths), with the resulting showers leaking minimally out of one or two crystals. The crystals have an excellent spatial resolution and a fast response. The scintillation decay time is sufficiently short so that roughly 80% of the light is emitted within the 25 ns corresponding to the nominal LHC bunch-crossing.

The ECAL is composed of three subcomponents. These are the barrel (EB), the endcap

(EE), and the preshower (ES). The EB covers the area within $|\eta| < 1.479$ and contains the bulk (61,200) of the PbWO$_4$ crystals. The EE covers the two forward regions, with a pseudorapidity coverage of $1.56 < |\eta| < 3.0$ and contains 7324 PbWO$_4$ crystals in each endcap. The ES sits just in front of the endcap crystals, providing an $|\eta|$ coverage from 1.653 to 2.6. It is composed of a layer of lead radiators to produce electromagnetic showers, with silicon millistrip sensors behind to measure the deposits. The purpose of the ES is to primarily detect forward neutral pions in order to distinguish them from isolated photons. The layout of ECAL is shown in Figure 2.5.
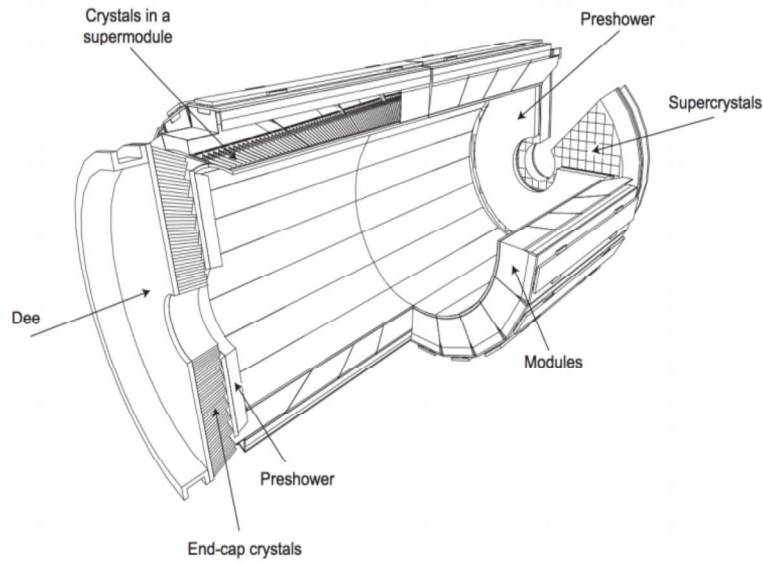
Figure 2.5: The CMS ECAL showing the crystals, modular structure, and an overall layout of the EB, EE, and ES subcomponents.

Because of its high granularity, the ECAL provides an excellent spatial resolution. However, the crystal beam-facing orientation combined with the lack of a segmented depth setup means that there is no information provided about the angle of the particles as they enter the calorimeter. Thus, the positional information is limited to the size of the crystals themselves. The radiation due to the large flux of particles through the detector results in degrading the overall transparency of the crystals. As a result, the energy measurements tend to drift over the time, resulting in a systematic deviation of energy measurement (and larger variations in response from crystal to crystal). This is handled using an in-situ laser calibration system, which provides a set of corrections and calibrations that evolve over

the length of a run. The energy resolution of the ECAL barrel can be parametrized by the following expression :

$$\left(\frac{\sigma}{E}\right)^2 = \left(\frac{S}{\sqrt{E}}\right)^2 + \left(\frac{N}{E}\right)^2 + C^2 \tag{2.6}$$

where S is the stochastic term, N is the noise term and C is the constant term. In an electron test beam measurement, the values of these three parameters were determined and they are $S = 0.028 \text{ GeV}^{\frac{1}{2}}$, $N = 0.12 \text{ GeV}$ and $C = 0.003$ respectively.

2.3.6 The Hadronic Calorimeter

The Hadronic Calorimeter (HCAL), which sits outside of the ECAL, is built with an intent to measure the energy of hadronic jets. The CMS HCAL is also important in measuring the missing transverse energy (MET), which is the energy carried away by the non-interacting particles such as neutrinos. In addition to providing these key measurements, the HCAL also provides a useful layer of discrimination for potentially fake electromagnetic particles. If an ECAL deposit is associated with an HCAL deposit, there is a good chance that the particle is a hadron which interacted with a nucleus in the ECAL (truly electromagnetic particles like the electron will deposit almost 100% of their energy in the ECAL).

In addition to its major usage for jet and MET study, the HCAL plays a key role in measuring the amount of pileup present in a collision. As most analyses at CMS are sensitive to the number of soft interactions and pileup, it is important to account and correct for the energies and compositions of these pileup events. The HCAL with its wide coverage in $|\eta|$ provides critical measurements in these corrections.

The HCAL is a sampling calorimeter, meaning the shower-inducing and energy measurement components are physically separated. Like the ECAL, it is also split into barrel and endcap regions called the HB and the HE. Also, there is a forward hadronic calorimeter (HF), which sits 11 m forward of the interaction point. Radially, the HCAL fits between the ECAL and the solenoid, extending from a radius of 1.77 m to 2.95 m. The HB cover-

age extends to $|\eta| < 1.305$, while the HE covers $1.305 < |\eta| < 3.0$. The HF covers the most forward regions of the detector, covering $3.0 < |\eta| < 5.0$. The geometry of the HCAL is shown in Figure 2.6.
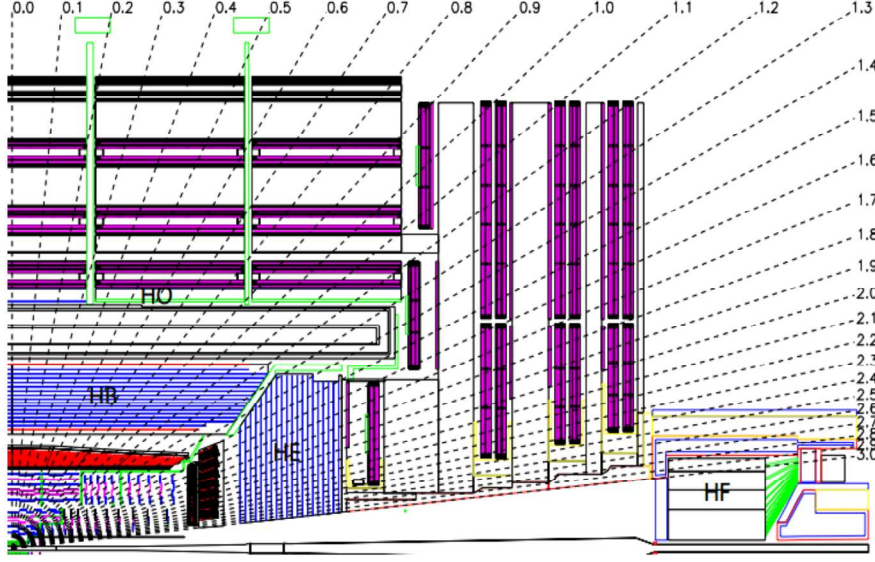
Figure 2.6: A longitudinal slice of the CMS HCAL.

The HB and HE subcomponents use interspersed sections of brass (to induce hadronic showers) and plastic scintillators to measure the resulting energy. In the forward HF, where the radiation is of great concern, the sampling is done using steel plates and energy measurements in quartz fibers. The interaction length, λ_i, of the brass is 16.42 cm. The amount of material increases with the azimuthal angle so that the number of interaction lengths through the entire HCAL increases from 5.82 λ_i to 10.6 λ_i at an $|\eta|$ of 1.3. The HE has similar coverage, with about 10 λ_i of total material.

2.3.7 The Muon System

The muon detector is the outermost part of the CMS detector. As its name implies, it is very important part of the CMS detector. The CMS muon system is made up with three different types of gas-based detectors. They are the drift tube (DT), cathode strip chambers (CSC) and the resistive plate chambers (RPC). The CMS muon system consists

of 250 DT chambers, 540 CSCs and 610 RPCs. The positions of the muon detector are illustrated in Figure 2.3.

The DT chambers are used in the barrel region, where both the muon rate and the neutron induced background are small while the magnetic field is very low. However, in the endcaps the muon and the background flux is much higher. Therefore, the muon detector endcaps are built from the CSCs that provide a faster response and a better resistance against radiation.

A DT cell is a 4 cm wide gas tube with a positively charged stretched wire inside. Each DT chamber, on an average 2×2.5 m^2 in size, consists of 12 layers of DT cells, arranged in three groups of four. The middle group measures the z coordinate while the two outer groups measure the $r\phi$ coordinate. In the barrel, four DT chambers are interspersed with the layers of the flux return yoke in each ϕ sector. The outermost muon station is equipped with DT chambers that contain 8 layers of DT cells and determine the muon position in the $r\phi$ plane. The barrel part of the muon system covers the region $|\eta| < 1.2$.

The CSCs are trapezoidal shaped multiwire proportional chambers that consist of 6 anode wire planes crossed with 7 copper strips cathode panels in a gas volume. They provide a two-dimensional position measurement, where the r and ϕ coordinates are determined by the copper strips and the anode wires, respectively. The muon detector endcaps consist of 4 CSC stations on each side, and identify muons in a pseudorapidity range of $0.9 < |\eta| < 2.4$.

The RPCs are made from two high resistive plastic plates with an electric voltage applied and separated by a gas volume. The signal generated by the muon when passing through the gas volume is picked up by readout strips mounted on the top of one of the plastic plates. The RPCs used in the muon system have a fast response. They have a timing resolution of 1 ns. Six layers of RPCs are installed in the barrel muon system and one layer of RPC is built into each of the first three stations of the endcap.
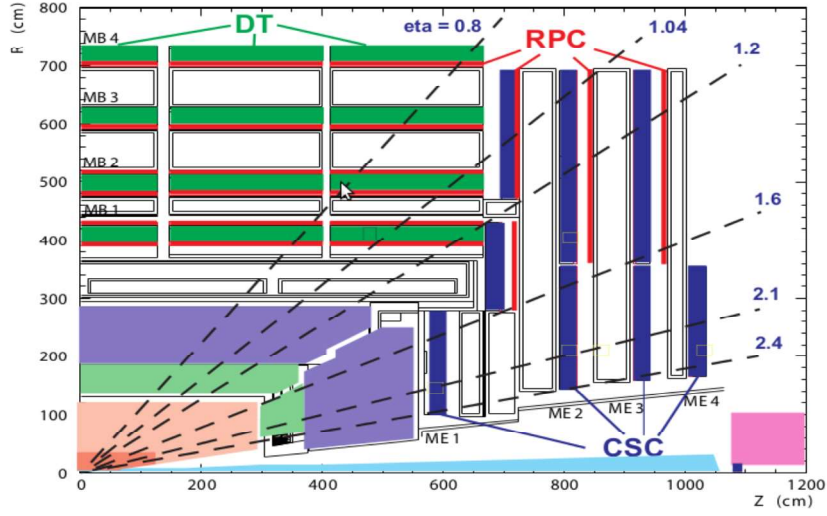
Figure 2.7: A quadrant of the CMS detector showing different muon detectors.

In Figure 2.7, the shaded areas in the lower left corner show position and size of the other detector components, such as the pixel and strip tracker, the ECAL and the HCAL. The magenta square in the lower right corner represents the HF. The η ranges of the different components of the muon system can be viewed from dashed lines.

2.3.8   The CMS Trigger System

The LHC provides collisions at high interaction rates, with beam crossing intervals of 25 ns corresponding to a crossing frequency of 40 MHz at its design setting. As the instantaneous luminosity of pp collision increases, the amount of events recorded by the CMS detector becomes very large. As all the events are not interesting from the physics point of view and it is also impossible to read out millions of channels and to store the huge amount of data produced, a substantial reduction of the event rate has to be achieved. This is accomplished in CMS by using a trigger system [24] that is basically at the beginning of the physics event selection chain. The CMS trigger system consists of two components:(a) Level-1 Trigger (L1) and (b) High Level Trigger (HLT). They are described below.

21

2.3.8.1 The Level-1 Trigger

At this stage, the information is purely hardware based and allows for a first rough estimation of relevant quantities. As a consequence, only simple calculations can be processed in the L1 stage of triggering. Still, unlike other L1 trigger systems that rely just on counting objects with an energy above certain threshold, the CMS L1 Trigger is capable of applying sophisticated trigger algorithms. At L1, the only information taken into account is the one coming from the muon chambers and the calorimeters. This information is used to identify physics objects such as muons, electrons, photons and jets, and permits to make a rough estimation of the p_T of the particles. The L1 trigger is divided into three subsystems. These are level 1 for calorimeters, level 1 for muon chambers and Global Trigger (GT). A schematic view of various components of the L1 trigger system is shown in Figure 2.8.
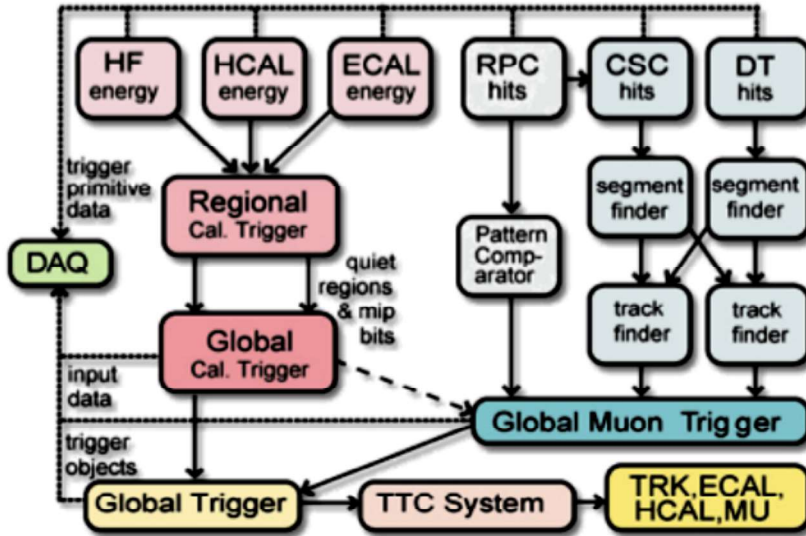
Figure 2.8: An overview of the CMS L1 Trigger system.

2.3.8.2 The High Level Trigger

The HLT is specially designed for the identification of different types of particles in CMS i.e, electrons, muons, photons, b quarks, tau leptons, jets and MET etc. At the L1 trigger level, the rate of the events has been already reduced from 10^9 kHz to ~ 100 kHz. At HLT,

22

the reduction should reach 100 Hz, so that a factor ~ 10^3 reduction must be accomplished by using intermediate steps L2 and L3. Once an event has been accepted by L1, the L2 makes a more precise reconstruction of the particles based on the hardware information. The L2 also uses the calorimeter, muon system information as well as some information from the tracker. This level reduces by a factor of 10 of the data rate. The L3 uses the CMS tracker information to reconstruct track of the object with good accuracy.

2.4   The CMS Software and Computing

CMS poses challenges not only to the physics to be discovered or the detector to be built, but also to the capability to record, store and analyze the huge amount of data produced. The data produced and the computer resources required in the CMS experiment to analyze those are at least an order of magnitude larger than in the previous high-energy physics experiments. So, the development of the necessary computing infrastructure as well as software toolkits are very important. Different software tools are described in this section. Some of them are officially provided by the CMS Collaboration while some others are specifically developed for different analysis [25]. The CMS computing model has been constructed as a distributed computing services based on Grid technologies.

2.4.1   The CMS Software Framework

The CMS Software (CMSSW) is the official software framework developed by the CMS Collaboration [25]. It is an object oriented framework based on C++ programming language. Its functionality includes event simulation and reconstruction as well as an ability to perform various physics analysis tasks. The CMSSW includes a completely revisited event data model and is fully integrated with a database infrastructure for handling calibration and alignment. The whole event data model (EDM) is based on the concept that all the data processing should pass through a single structure called the event. Inside the CMSSW, the user can make a configuration file for job submission where the information

of which data to take, what tasks to perform and what information finally needs to be stored in the output file. For each task in the processing of the data, a framework module needs to be implemented. The module defines which information is needed for the event to execute its module specific task. To be able to fully process an event, one has to take into account potentially changing and periodically updated information about the detector environment and status such as calibrations, alignments, geometry descriptions etc. The CMSSW framework also facilitates to use external software packages, for example event generation packages, FastJet package etc.

2.4.2   Workflow of the Analysis

To perform the analysis described in this thesis, the whole CMS computing chain was used. Monte Carlo (MC) simulated data and real collision data were equally treated. While the MC events are generated at the Tier-0, real data was recorded directly in the experiment and then transferred to the Tier-0. The format of the original samples (MC and data) is RAW, so these samples are large and contain all possible information. Afterwards the RAW data are transferred to the Tier-1 sites where the re-reconstruction, skimming and selection are performed. The resulting data, in the RECO format, are then transferred to the Tier-2 sites in which they are re-processed to the AOD format.

The analysis is performed using AOD data, the lightest format. A dataset is chosen depending on the needs of the analysis, that is, for a MC study, the datasets corresponding to the signal and the main backgrounds are chosen. For Data, a primary dataset based in a certain HLT trigger path, or a secondary skim provided by the corresponding physics group is selected. The final physics analysis can be performed in many different ways. In the case of this thesis, it was primarily done in the so-called EDAnalyzer mode. The CMSSW provides different modules to perform, for example, the pre-selection of interesting events, sophisticated muon identification and isolation, jet energy and missing transverse energy(E_T) corrections, and so on.

Chapter 3

Study of $B_s \to \mu^+\mu^-$ decay

The current chapter of the thesis describes the analysis performed for the observation of $B_s \to \mu^+\mu^-$ decay. Then in next sections, the analysis strategy is described in detail. The selections used to discriminate true signal events from background events and the background sources are described in detail. Next, the two methods CL_s technique and unbinned maximum likelihood fit used to extract the candidate yields are discussed in detail. Results and interpretations of these results are reported afterwards.

3.1 Analysis Overview

This analysis searches the decays $B_s \to \mu^+\mu^-$ and $B_d^0 \to \mu^+\mu^-$ simultaneously and the signal events are extracted in two ways as follows:

1. with a counting experiment in a signal window in the dimuon invariant mass distribution centered around the $B_{(s)}^0$ meson mass;

2. with an unbinned maximum likelihood fit to the dimuon invariant mass distribution.

To correctly discriminate between signal and background events, all the analysis selections are studied in detail and chosen without using events in a dimuon invariant mass re-

gion close to that of the $B^0_{(s)}$ mesons ("blind analysis"). Only after all selections are fixed, the invariant mass window is opened ("unblinded") and the actual number of events are measured. This analysis uses a relative normalization $B^\pm \to J/\psi K^\pm \to \mu^+\mu^- K^\pm$ to avoid the uncertainties of the $b\bar{b}$ production cross-section and of the luminosity measurements. Furthermore, many systematic errors cancel at first order normalizing the signal to a similar decay channel measured in data.

The $B_s \to \mu^+\mu^-$ measured branching fraction can be written as:

$$\mathscr{B}(B^0_s \to \mu^+\mu^-) = \frac{N^{B^0_s}_{obs}}{N^{B^\pm}_{obs}} \times \frac{\epsilon_{B^\pm}}{\epsilon_{B^0_s}} \times \frac{f_u}{f_s} \times \mathscr{B}(B^\pm \to J/\psi K^\pm) \times \mathscr{B}(J/\psi \to \mu^+\mu^-) \qquad (3.1)$$

where $N^{B^0_s}_{obs}$ and $N^{B^\pm}_{obs}$ are the signal and normalization yields; $\mathscr{B}(B^\pm \to J/\psi K^\pm)$ and $\mathscr{B}(J/\psi \to \mu^+\mu^-)$ are the branching fractions for the $B^\pm \to J/\psi K^\pm$ and $J/\psi \to \mu^+\mu^-$ decays respectively. The $B^0_d \to \mu^+\mu^-$ branching fraction formula is similar to Eq. 3.1, but without the f_u/f_s ratio.

The total efficiency ϵ is factorized into two components, (i) acceptance efficiency (ϵ_{acc}) and (ii) reconstruction efficiency (ϵ_{reco}):

1. ϵ_{acc} is basically the ratio between the no. of events passing single muon selection cuts (which is applied at the GEN level of the simulation) over the total no. of events generated.

2. ϵ_{reco} is defined as the ratio between the no. of reconstructed events passing the analysis selection cuts over the no. of events passing single muon selections.

$$\epsilon_i = \epsilon_{acc,i} \times \epsilon_{reco,i} \qquad (3.2)$$

The determination of the signal efficiency is done through MC simulation samples. It is important to validate the MC simulations in data, thus the analysis uses a Control Sample (CS): $B_s \to J/\psi\phi$, where the J/ψ meson decays into two muons and the ϕ meson decays

into two kaons, allowing to compare B_s meson observables directly in data and in MC simulations. In Eq. 3.1 above, the factor f_u/f_s is the ratio of probabilities for a b quark to hadronize into a $B^{\pm}$ or a B_s meson. Assuming f_u to be equal to f_d, we can use the f_s/f_d LHCb measurement, which reports, for $2 < \eta < 5$ [26],

$$\frac{f_s}{f_d} = 0.256 \pm 0.020 \tag{3.3}$$

The Normalization Sample (NS) i.e, $B^{\pm} \rightarrow J/\psi K^{\pm}$ has a high cross-section which in turn gives a high statistics sample. Another interesting normalization decay, for the $B_s \rightarrow \mu^+\mu^-$ case, could be $B_s \rightarrow J/\psi\phi$, such that the f_s/f_u ratio would not be needed, but its branching fraction is still not well measured (its relative uncertainty is about 25%) [27]:

$$\mathcal{B}(B_s \rightarrow J/\psi\phi) = 1.09^{+0.28}_{-0.23} \times 10^{-3} \tag{3.4}$$

Instead, for the chosen normalization channel, the overall branching fraction relative uncertainty is around 3.4%:

$$\mathcal{B}(B^{\pm} \rightarrow J/\psi K^{\pm}) = (1.016 \pm 0.033) \times 10^{-3} \tag{3.5}$$

$$\mathcal{B}(J/\psi \rightarrow \mu^+\mu^-) = (5.93 \pm 0.06) \times 10^{-2} \tag{3.6}$$

For this analyis, the background level is very different in the forward region of the detector, compared to the barrel region. Furthermore, the mass resolution in the CMS tracker depends strongly on the pseudorapidity of the reconstructed particles. Therefore, this analysis is performed in two distinct categories: if both muons fulfill $|\eta| < 1.4$, then the B_s candidate belongs to the "barrel category"; otherwise it belongs to the "endcap category".

3.2   Production mechanism and acceptance cross-check

In the pp collisions at LHC, the heavy b-quarks are produced in the hard collision of two partons. Once the b quarks are produced through the initial hard scattering, the process of forming B hadrons follows and is called *hadronization* or *fragmentation*. The b-pair production is carried out by any of the following three processes (shown in Figure 3.1):

1. *Flavor Excitation(FE)* where the QCD hard 2-to-2 reaction corresponds to the scattering of a b quark out of the initial state into the final state by a gluon or light quark or antiquark via the subprocess $g + b \rightarrow g + b, q + b \rightarrow q + b$, or $\overline{q} + b \rightarrow \overline{q} + b$.

2. *Flavor Creation(FC)* which corresponds to the $b\overline{b}$ pair by gluon-gluon fusion or by annihilation of light quarks via two 2-to-2 parton subprocesses, $g + g \rightarrow b + \overline{b}$ and $q + \overline{q} \rightarrow b + \overline{b}$.

3. *Gluon Splitting(GS)* includes the subprocess, $g + g \rightarrow g + (g \rightarrow b\overline{b})$ where a gluon is fragmented to a b-pair.

(a)   (b)   (c)
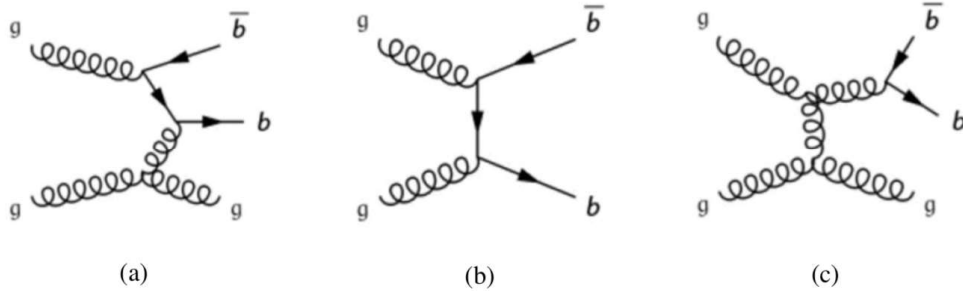
Figure 3.1: Examples of different mechanisms for $b\overline{b}$ production: (a) flavor excitation, (b) gluon-gluon fusion(flavor creation) and (c) gluon splitting. Out of the three production mechanisms, gluon splitting(GS) is found to be the most dominant one.

In this chapter, the acceptance ratio of signal sample ($B_s \rightarrow \mu^+ \mu^-$) to normalisation sample ($B^+ \rightarrow J/\psi K^+$) in different pseudorapidity regions were calculated. The main motivation was to crosscheck whether the ratio is dependent or independent on the chosen regions.

28

The following recipe was followed for calculating the acceptance for both signal and normalisation sample.

- Find the B meson and also the b-(anti)quark from which it's originated, along with this also find the b quark produced in conjuction.

- Apply the η cuts on the b-quark pair; find the tracks of the B meson for those events passing the above η cuts.

- Apply the following cuts on the tracks too.

  <u>Signal Sample</u>: $p_T^\mu > 3.5$ GeV and $|\eta^\mu| < 2.5$

  <u>Normalisation Sample</u>: $p_T^\mu > 3.5$ GeV, $|\eta^\mu| < 2.5, p_T^K > 0.4$ GeV and $|\eta^K| < 2.5$

$$\text{Acceptance} = \frac{\text{no. of } B \text{ mesons where tracks pass all the cuts above}}{\text{no. of } B \text{ mesons generated}}$$

Simulation was done in PYTHIA with MSEL=1 amd CKIN=±10 and both lower and higher statistics were considered. The results from higher statistics are shown here.

Sample	Setting	Acceptance	Production mechanism		
			FC	FE	GS
$B_s \to \mu^+\mu^-$	$\|\eta\| < 10$	0.059 ± 0.002	0.074 ± 0.006	0.076 ± 0.004	0.044 ± 0.002
	$\|\eta\| < 5$	0.064 ± 0.002	0.078 ± 0.007	0.085 ± 0.005	0.048 ± 0.003
	$\|\eta\| < 2.5$	0.091 ± 0.004	0.111 ± 0.012	0.110 ± 0.009	0.076 ± 0.005
$B^\pm \to J/\psi K^\pm \to \mu^+\mu^- K^\pm$	$\|\eta\| < 10$	0.0197 ± 0.0007	0.030 ± 0.002	0.027 ± 0.001	0.013 ± 0.001
	$\|\eta\| < 5$	0.0219 ± 0.0008	0.032 ± 0.003	0.031 ± 0.002	0.014 ± 0.001
	$\|\eta\| < 2.5$	0.0326 ± 0.0015	0.046 ± 0.005	0.038 ± 0.003	0.026 ± 0.002
		$[A(B^+)/A(B_s)]$			
			FC	FE	GS
	$\|\eta\| < 10$	0.334 ± 0.016	0.405 ± 0.042	0.355 ± 0.023	0.295 ± 0.026
	$\|\eta\| < 5$	0.342 ± 0.016	0.410 ± 0.053	0.365 ± 0.032	0.292 ± 0.028
	$\|\eta\| < 2.5$	0.358 ± 0.023	0.414 ± 0.063	0.345 ± 0.040	0.342 ± 0.035

Table 3.1: Variation of the acceptance when changing the PYTHIA $b\bar{b}$ production η range, for all production modes combined(third column) and for production modes split into flavor creation(FC), flavor excitation(FE), and gluon splitting(GS). The lower part of the table shows the ratio between normalisation acceptance and signal acceptance.

From Table 3.2, it's clear that the acceptance ratio is found to be independent of pythia production η cuts.

3.2.1 Background Sources

The main challenge in the $B_s \to \mu^+\mu^-$ BF measurement is the backgrounds suppression. The signal topology for this decay is simple: two muons originating from the common vertex. There are many background sources which can mimic a signal like event. This analysis searches for two reconstructed tracks with opposite charges identified as muons. These two tracks must come from a common vertex (called secondary vertex) which should be well displaced (around few millimeters) from the pp primary vertex. Furthermore, the dimuon invariant mass must be compatible with that of the B_s meson.

The reconstructed tracks are identified as muons by the three CMS muon sub-detectors (see Sec. 2.3.7). Thus, background events can be composed by "true" muons, generated by different physics processes or "fake" muons (such as kaons, pions and protons) misidentified wrongly as reconstructed muons. Mainly, the misidentification may be (i) due to a punch-through of the particle inside the muon stations or (ii) due to a hadron decay-in-flight. The fake rate has been studied with MC simulations and described in Sec 3.4. From the analysis point of view, the main background sources can be grouped into three categories:

1. Combinatorial background formed by muons coming from b or c weak decays ($q \to X\mu\bar{\nu}$): in this category, those events are present where a true muon is combined with a hadron misidentified as a muon;

2. Rare B^0_d, $B^\pm$, B_s and Λ^0_b semileptonic decays (like $B_s \to K^-\mu^+\nu_\mu$), in which a hadron is misidentified as a muon. Since the neutrino is not reconstructed, this category forms a continuous background in the invariant mass;

3. Rare dihadronic B^0_d, $B^\pm$, B_s and Λ^0_b decays (like $B_s \to K^+K^-$), which form a broad peak in the B_s invariant mass region.

A further background component is the possible cross-feed between the $B_s \to \mu^+\mu^-$ and

the $B_d^0 \to \mu^+ \mu^-$ decays, in which a B_s event could be identified as a B_d^0 event due to the detector resolution, or vice versa.

The first background source is without any peaking structure in the dimuon mass distribution. No MC simulation is used to study this combinatorial background: the number of generated events would be too consuming both in terms of CPU time and disk storage, to have a several times larger dataset than the 25 fb^{-1} of collected data. To overcome this difficulty, the dimuon invariant mass side-bands are used(see Sec. 3.5). The second and third sources present shapes in the dimuon mass distribution that can help to separate them from the signal events(see Sec. 3.9.1). MC simulations are used to study the impact of these rare backgrounds on the $B_s \to \mu^+ \mu^-$ BFs. Without any strong selection, the first category contains by far the largest fraction of background events, as it is roughly one hundred thousand times bigger than the SM signal expectations. Regarding the rare decays, they have a non-negligible effect although they have very low misidentification probability and small BFs.

3.3   Primary datasets and triggers used

In CMS, collected data must pass a scrutiny that certifies the quality of each run and of each single luminosity section; only those fractions that pass this certification can be used by analyses. There are two types of certification, one which checks the performances of the inner tracker and the muon stations (called "muon certification") and one that includes also the performance of the two calorimeters (called "golden certification"). Since this analysis uses reconstructed tracks and muons, but no information from calorimeters, the first kind of certification is used. The total integrated luminosity, corresponding to the muon certification, is equal to (5.0 ± 0.1) fb^{-1} for the 7 TeV run in 2011 and (20.0 ± 0.5) fb^{-1} for the 8 TeV run in 2012 [28].

The total L1 and HLT rate bandwidths are shared between different analysis groups. A careful study is made before and during the data acquisition, to optimize the full rate

to each physics group's need. All L1 triggers involved in the $B_s \rightarrow \mu^+\mu^-$ analysis require the presence of two high quality muons objects in the event. During the 2011 data taking, muons were requested to have $|\eta^{L1}| < 2.4$. During 2012, due to the increasing luminosity, to keep the rates under control while retaining the best quality events, the maximum pseudorapidity was decreased to $|\eta^{L1}| < 2.2$ and the minimum transverse momentum was increased to $p_T^{L1} > 3$ GeV. Two different sets of HLT trigger paths are used by this analysis: one acquires events in the signal invariant mass region, the other collects normalization and control events. Both trigger paths save the events in the *MuOnia* primary dataset(PD) which is primarily used for this analysis. *MuOnia* is the PD principally used by the *B*-physics group in CMS. The HLT trigger selection for both signal and normalization channels is based on two opposite-charge L3 muons, the highest quality of HLT identified and reconstructed muons. In CMS, the *B*-physics analyses usually rely on HLT paths that apply cuts on the transverse momentum and on the pseudorapidity of muons and dimuons. With increasing instantaneous luminosity (during the two years, the luminosity raised from about 5×10^{32} to about 8×10^{33} $cm^{-2}s^{-1}$), the threshold of the muon p_T was consequently raised and additional requirements on the dimuon mass and momentum and on secondary vertex(SV) observables, were implemented.

An important element to consider is the presence of pileup, especially in the 2012 run. Two uncorrelated muons coming from different primary vertices could be coupled to form a displaced dimuon. On every *B*-physics dimuon trigger, a selection based on the distance of the closest approach between the two muon tracks is applied, *i.e.* the minimum 3D distance d_{ca}^{L3} between the two muon tracks must satisfy $d_{ca}^{L3} < 0.5$ cm. Next sections are dedicated to the descriptions of the two HLT path sets used by this analysis. Despite the different instantaneous luminosities, signal and normalization triggers did not change much during each year, thus only the strictest versions of each HLT path are described.

3.3.1 HLT paths for signal sample

In a search for rare decays, the signal trigger efficiency must be the highest as possible. Since in the barrel the resolution is better and the background level is lower than in the endcaps, two different trigger paths are used, with different η ranges: the one with the strictest muon η range can apply the lowest p_T requirements. The pseudorapidity request, $|\eta| < 1.8$, is chosen to be wider than the analysis barrel category cut, to take into account the slightly worse trigger resolution.

All signal paths request the dimuon invariant mass to be around the B_s meson masses: $M_{\mu\mu} \in [4.8, 6.0]$ GeV. Additional kinematic requests are shown in Table 3.2. Finally, a very loose cut is requested on the dimuon vertex minimum probability: $p > 0.05\%$. This quantity is the SV fit p-value evaluated from the χ^2 of the vertex, given the two degrees of freedom, corresponding to the two muon tracks used by the vertex builder. The total allowed rate for the B_s triggers during the two years of data taking was about 5 Hz. The maximum rate, measured at the beginning of the run, is about 3.3 Hz, and it decreases to about 1.3 Hz at the end of the data acquisition.

HLT path	min p^{L3}_{T,μ_1} (GeV)	min p^{L3}_{T,μ_2} (GeV)	max $|\eta|^{L3}_{\mu}$	$p^{L3}_{T,\mu\mu}$ (GeV)
Barrel 2011	4.0	4.0	1.5	3.9
Endcap 2011	4.0	4.0	2.4	5.9
Barrel 2012	3.0	4.0	1.8	4.9
Endcap 2012	4.0	4.0	2.2	6.9

Table 3.2: Kinematic selections at HLT level for the signal channel, for each different used trigger.

3.3.2 HLT path for normalization and control samples

Both normalization and control channels rely on the reconstruction of J/ψ mesons at the HLT level. The high CMS performances on muon reconstruction allow for a very clean and high purity J/ψ meson signal-over-background ratio. The J/ψ meson has by far the highest cross-section with respect to the other resonances involved in the B-physics

analyses. In order to keep the *B*-physics HLT rate within the allowed bandwidth, much stricter selections than for the B_s signals are requested, which involve kinematic and SV selections. The HLT path used by this analysis selects on well-displaced J/ψ mesons coming from *B*-meson decays. The requirements are:

- two L3 muons with $p_{T,\mu}^{L3} > 4$ GeV and $|\eta_\mu^{L3}| < 2.2$. The high-rapidity region $|\eta_\mu^{L3}| >$ 2.2 is removed by the L1 requests;

- dimuon vertex fit minimum probability greater than 15%;

- dimuon invariant mass centered around the J/ψ meson, in [2.9, 3.3] GeV, and dimuon transverse momentum $p_{T,\mu\mu}^{L3} > 6.9$ GeV;

- transverse life-time significance $L_{xy}^{L3} > 3$, where L_{xy}^{L3} is the ratio of the transverse distance between the dimuon vertex and the PV, over its uncertainty;

- cosine of the transverse pointing angle α_{xy} higher than 0.9. The transverse pointing angle is the angle between the dimuon momentum and the vector from the PV to the dimuon vertex, in the transverse plane. For a perfectly aligned tracker, this angle must approach zero, compatibly with the tracker resolution.

The total rate for this displaced J/ψ trigger was one of the highest allowed (around 8 Hz), as J/ψ mesons coming from *B* decays are used also by many other *B*-physics analyses.

3.4   Fake Rate studies with simulation sample

As described in Sec 3.2.1, in case of peaking backgrounds both hadrons can be misidentified as muons, as a result it mimics as a signal (which is "fake", not "true") in the signal region. So we need to minimize the "misidentification probability" as possible and also need to calculate its probability to be taken into account properly. This study is done with three peaking background samples, e.g, $B_s \rightarrow K^+K^-$, $B^0 \rightarrow \pi^+\pi^-$ and $\Lambda_b^0 \rightarrow pK^-$ to study the misid rate for K,π and p respectively in both barrel and endcap region for both

Hadrons	misidentification prob (10^{-3})
π	0.5–1.3
K	0.8–2.2
p	0.4–1.5

Table 3.3: Muon misidentification probability ranges for pions, kaons and protons.

positive and negative charges as a function of transverse momentum. The corresponding plots are shown in Figures 3.2, 3.3 and 3.4 respectively whereas the Table 3.3 lists the corresponding probablities.

3.5 Discriminating variables for B_s signal decays

Once two muon tracks with opposite charges are found in an event and their invariant mass lie within the overall signal mass window, they form a "B candidate". The signal acceptance, evaluated with a MC simulation produced with no generator filters, requests the signal candidate to be in the detector volume:

- both generated muons coming from the B decay must be within the geometric acceptance: $|\eta| < 2.5$ and $p_T > 3.5$ GeV;

- both muons must have a reconstructed *highPurity* track with $|\eta| < 2.4$ and $p_T > 3.5$ GeV.

The invariant mass region under study is divided into four separate sub-ranges, defined in Table 3.4. The SV is determined with the kinematic vertex fitter, applying a geometric constraint. The vertex fit reduced χ^2 is one of the input variables for the candidate MVA. Given the secondary vertex and its momentum, a matching PV is chosen on the distance of the closest approach along the z axis. To avoid any geometrical bias due to displaced tracks, all tracks forming the B candidate are removed from the chosen PV and this is "refitted", *i.e.* it is reconstructed with the remaining tracks (this is valid also for the NS and CS samples that have three or four tracks, respectively).
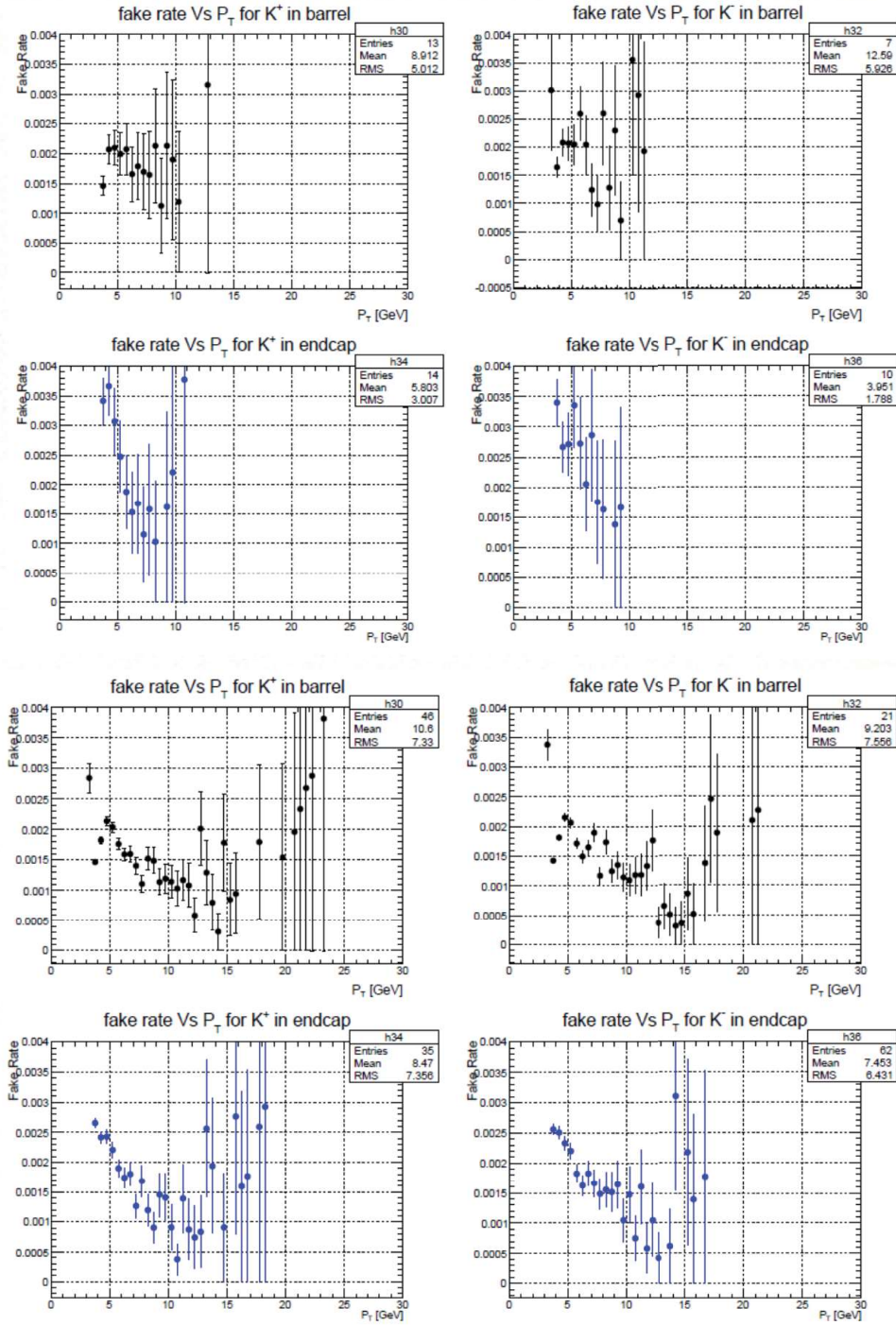
Figure 3.2: Kaon misid probability in 2011(top two rows) and 2012(bottom two rows) simulation samples in both barrel and endcap regions.
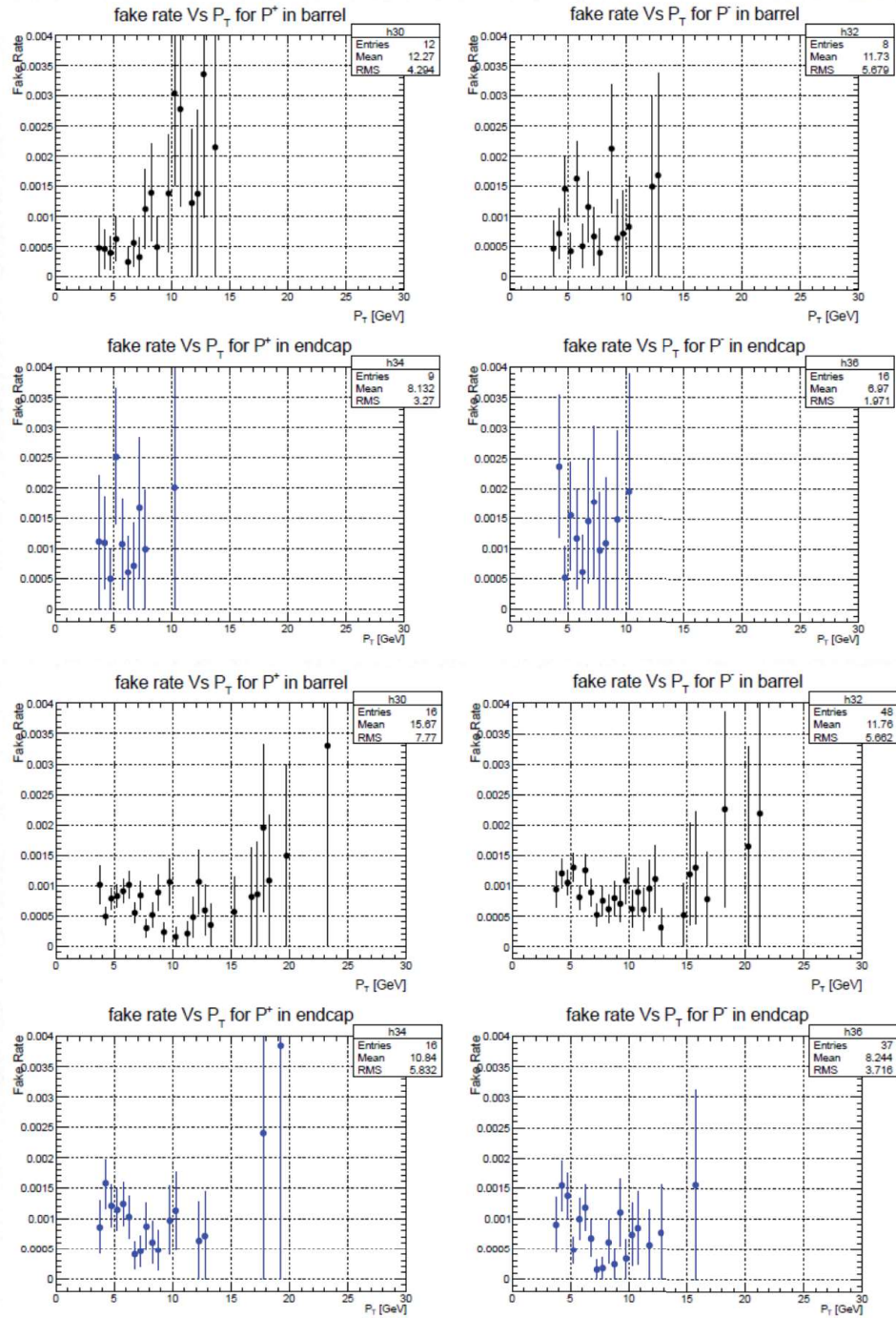
Figure 3.3: Proton misid probability in 2011(top two rows) and 2012(bottom two rows) simulation samples in both barrel and endcap regions.
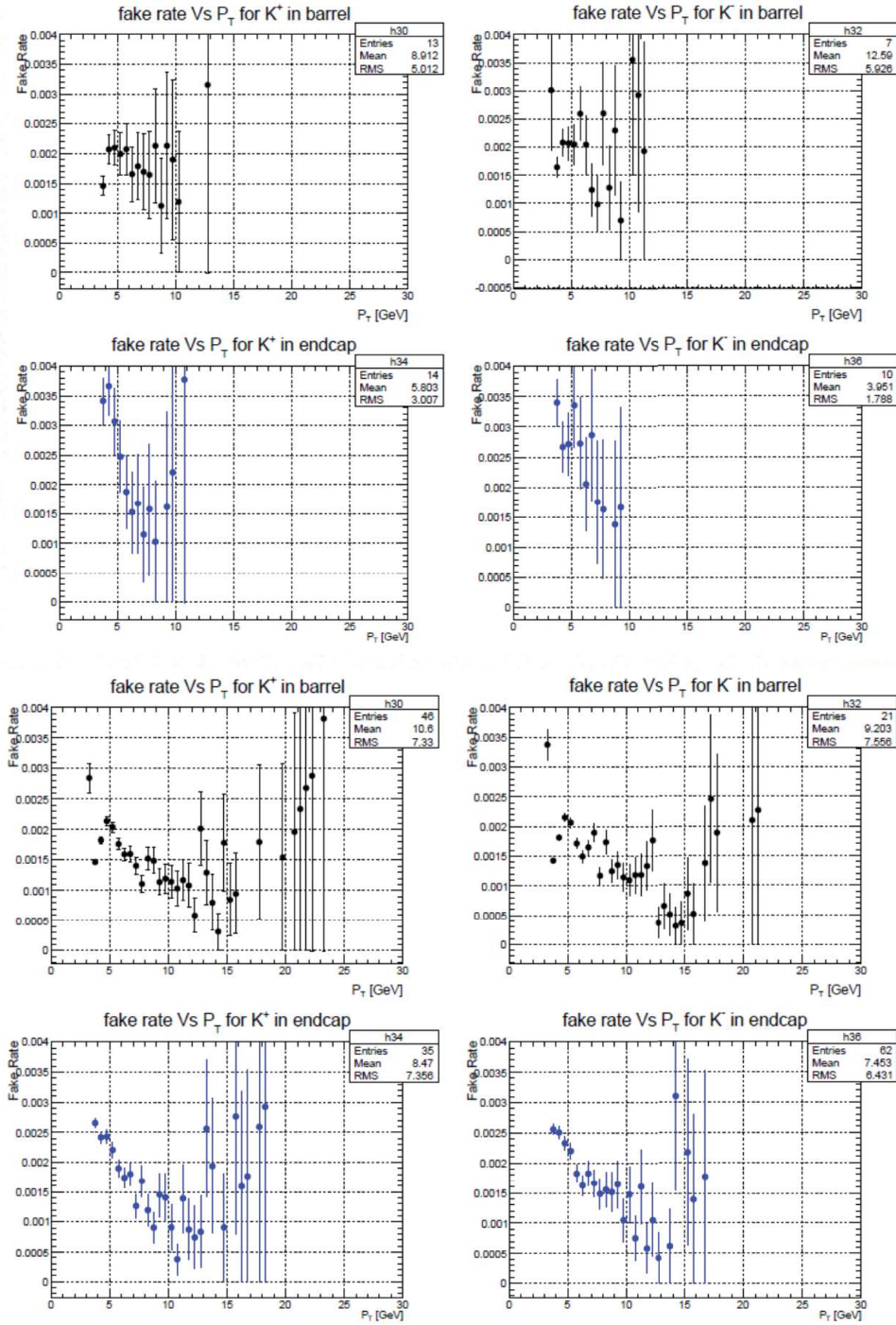
Figure 3.4: Kaon misid probability in 2011(top two rows) and 2012(bottom two rows) simulation samples in both barrel and endcap regions.

Definition	Invariant mass range in GeV
overall mass window	[4.9,5.9]
$B_s \to \mu^+\mu^-$ signal window	[5.2,5.3]
$B_d^0 \to \mu^+\mu^-$ signal window	[5.3,5.45]
blind window	[5.2,5.45]
side-band windows	[4.9,5.2]$\cup$[5.45,5.9]

Table 3.4: Invariant mass region definitions for the signal channel.

The main background is made by the combination of two uncorrelated muons (Figure 3.5), that can come from two different b or c decays. The inner tracker resolution is fundamental to discriminate these fake dimuons from real signals. The SV for these decays is badly reconstructed, their trajectories do not fit well to the same spatial point, as they should be if they are coming from a real decay, and the dimuon reconstructed tracks do not fit well considering from an existing PV. All these elements are investigated with the SV variables described in this section. An other feature is that since many of these muons can come from various decay chains, other charged particles (mainly pions and kaons) are present around them and this can be checked by looking for other close-by tracks. Hence, we define "isolation" variables to explore this effect. The candidate three-dimensional impact parameter with respect to the PV δ_{3D} and its significance $\delta_{3D}/\sigma(\delta_{3D})$ are used in the event selection. The same is true for the significance of the 3D flight length, ($l_{3D}/\sigma(l_{3D})$). Other important variables for displaced vertices are the pointing angle α_{3D}, that is the angle in three dimensions between the B-candidate momentum and the vector from the PV to the SV, and the distance of closest approach between the two muon tracks d_{ca}^{max}. A sketch of the variables related to the SV are shown in Figure 3.6.

3.6 Normalization channel event selection

The chosen NS channel is the decay $B^\pm \to J/\psi K^\pm \to \mu^+\mu^- K^\pm$. In principle, various channels could be used, each with advantages and disadvantages:

- the decay $B^\pm \to J/\psi K^\pm \to \mu^+\mu^- K^\pm$ offers the minimal number of additional tracks
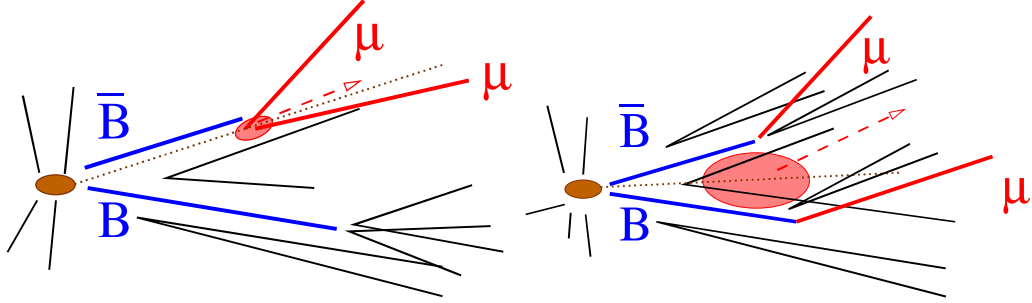
Figure 3.5: Sketch of signal (left) and combinatorial background (right) events.
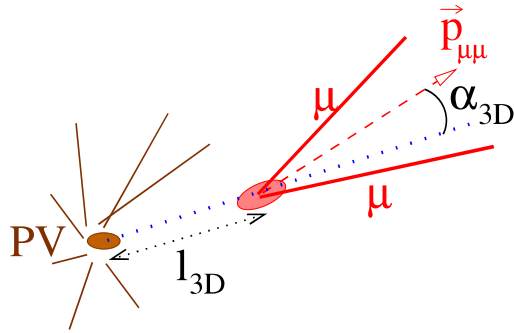
Figure 3.6: Visual sketch of a displaced decay: the impact parameter δ_{3D}, the decay length l_{3D} and the pointing angle α_{3D} variables are shown. The two muon tracks are combined to form the dimuon momentum $p_{\mu\mu}$.

next to the dimuon. The disadvantage is that the ratio of $B^{\pm}$ and B_s hadronization is known only to 8% [27]. The $B^{\pm} \to J/\psi K^{\pm} \to \mu^+\mu^- K^{\pm}$ and the $J/\psi \to \mu^+\mu^-$ BFs carry an additional 3.4% [27];

- the decay $B_s \to J/\psi\phi \to \mu^+\mu^- K^+ K^-$ has a branching fraction relative uncertainty of 32% [27]. Furthermore, since this channel has two hadronic tracks, the tracking uncertainty, which will be discussed later, is twice larger than in the channel $B^{\pm} \to J/\psi K^{\pm} \to \mu^+\mu^- K^{\pm}$;

- the decay $B_s \to K^+ K^-$ would be a very interesting normalization channel but there is no displaced hadronic trigger and no kaon identification in CMS. Hence, it cannot be used.

For these reasons the chosen normalization channel in CMS is the decay $B^{\pm} \to J/\psi K^{\pm} \to \mu^+\mu^- K^{\pm}$. For the NS acceptance, the requests are the same as for the signal, but with further requirements on the kaon track:

- the generated kaon track must fulfill $p_T > 0.4$ GeV and $|\eta| < 2.5$;

- the reconstructed *highPurity* kaon track must have $p_T > 0.5$ GeV and $|\eta| < 2.4$.

Only events that pass the triggers on displaced J/ψ mesons, as described in Sec. 3.3.2, are selected. Thus, the off-line reconstruction of $B^{\pm} \to J/\psi K^{\pm} \to \mu^+\mu^- K^{\pm}$ candidates starts from two muons with opposite charge, coming from a SV. Each other track in the event is coupled to the muon pair, to form $B^{\pm}$ candidates, and the kaon mass hypothesis is assigned to this track. The two muon tracks and the kaon track must be of *highPurity* quality and be within the acceptance of the inner tracker ($p_T > 0.5$ GeV and $|\eta| < 2.4$ for the 2011 data or $|\eta| < 2.1$ for the 2012 data). The distance of closest approach between all pairs among the three tracks is required to be less than 1 mm. The dimuon invariant mass $M_{\mu\mu}$ must be compatible with that of a J/ψ meson, i.e, $M_{\mu\mu} \in [3.0, 3.2]$ GeV. All three tracks are used in the vertex fitting.

Table 3.5 defines the side-bands and signal regions for the normalization channel. These mass regions are adopted for the side-band subtraction used in the comparison of $B^{\pm} \rightarrow J/\psi K^{\pm} \rightarrow \mu^{+}\mu^{-}K^{\pm}$ decays in data and MC simulation. In Figure 3.7, the distributions of sideband substracted are shown both for data amd normalization mc simulation. The comparison shows good agreement for all the shown varaibles.
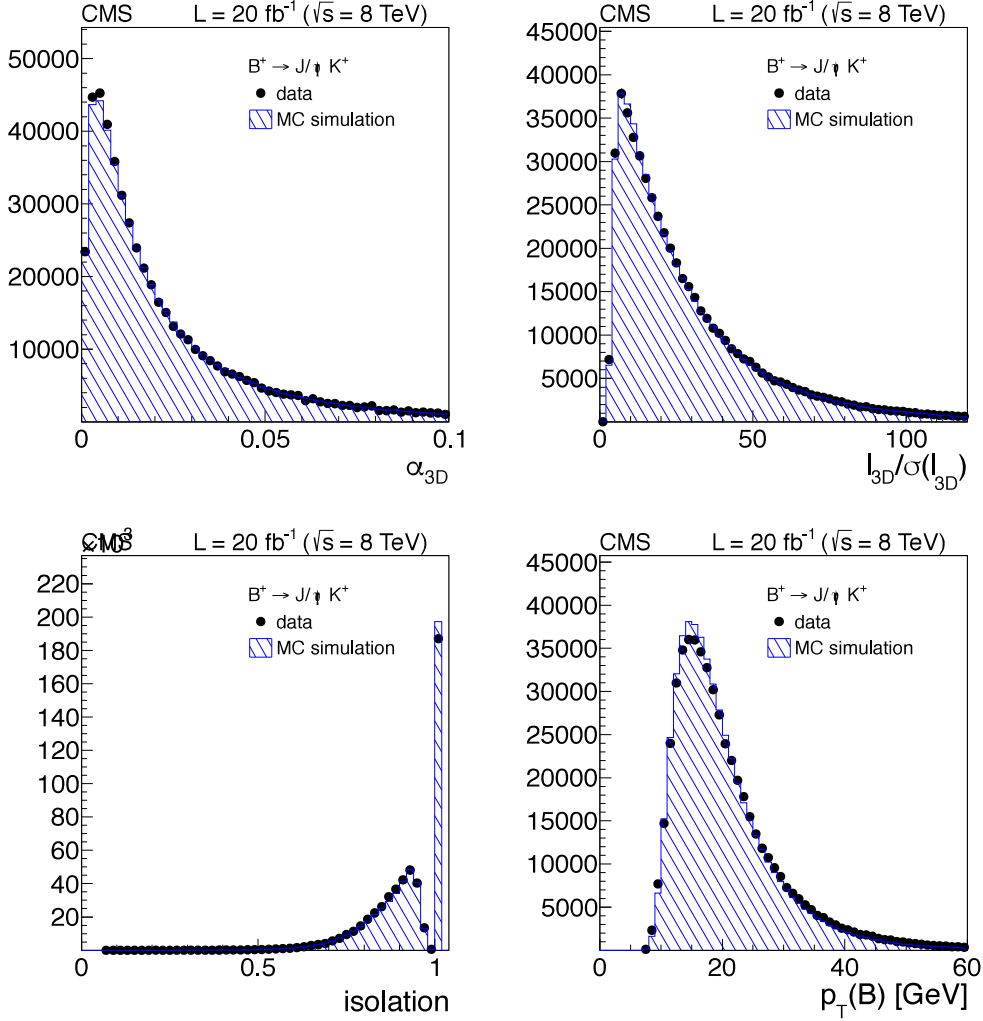
Figure 3.7: comparison of sideband substracted distributions (pointing angle, flight length significance, isolation and transverse momentum) for $B^{\pm} \rightarrow J/\psi K^{\pm} \rightarrow \mu^{+}\mu^{-}K^{\pm}$. The black solid points represent data wheras the blue shaded region represents the normalization mc simulation.

Definition	Invariant mass range in GeV
overall mass window	[4.9,5.9]
low side-band	[5.05,5.15]
signal window	[5.2,5.35]
high side-band	[5.4,5.5]

Table 3.5: Invariant mass region definitions for the normalization channel.

3.7 Control sample event selection

It is fundamental to check that the signal MC simulation well reproduces the B_s meson distributions in data. For this purpose, $B_s \rightarrow J/\psi\phi \rightarrow \mu^+\mu^- K^+ K^-$ decays are used as a validation of the MC simulations and as a way to estimate the systematic uncertainty of the analysis efficiency for $B_s \rightarrow \mu^+\mu^-$, based on the level of agreement between data and MC simulation. The validation of the MC simulation is especially important for the isolation variables. The decay $B_s \rightarrow J/\psi\phi \rightarrow \mu^+\mu^- K^+ K^-$ has four final state particles, thus lowering on average the muon transverse momenta compared to the signal decay. Since the muon p_T requirements stay at the same numerical values for the signal decay and the normalization and control channels, the p_T distribution of the B_s candidates is expected to be harder. The CS acceptance requests one more kaon track fulfilling the same acceptance requirements of Sec. 3.6. The trigger paths are the same as for the normalization sample (see Sec. 3.3.2), since they are based on displaced J/ψ mesons. All four involved tracks must fulfill the same selections described in Sec. 3.6 for the NS selection: *highPurity* tracks with $p_T > 0.5$ GeV and $|\eta| < 2.4$ for the 2011 data or $|\eta| < 2.1$ for the 2012 data. The two opposite-sign muons are combined to form a J/ψ candidate, while the other two opposite-sign tracks are assumed to be kaons, that must have an invariant mass M_{KK} $\in [0.995, 1.045]$ GeV, to form the ϕ meson candidate. To further suppress background events, the two kaons must have $\Delta R < 0.25$ in the $\eta - \phi$ plane.

Table 3.6 defines the side-bands and signal regions for the CS channel. In Figure 3.8, the distributions of sideband substracted are shown both for data amd control mc simulation.

The comparison shows good agreement for all the shown variables.
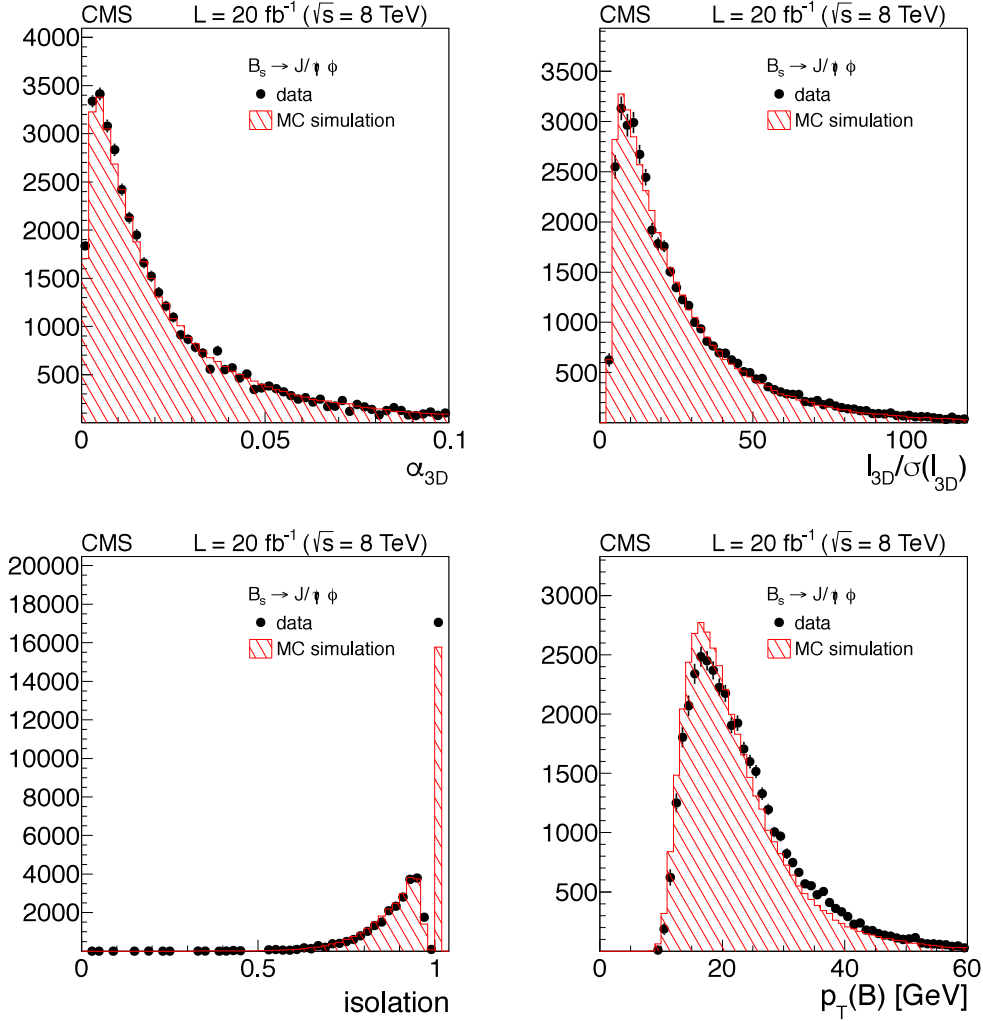
Figure 3.8: comparison of sideband substracted distributions (pointing angle, flight length significance, isolation and transverse momentum) for $B_s \rightarrow J/\psi\phi \rightarrow \mu^+\mu^- K^+ K^-$. The black solid points represent data wheras the red shaded region represents the control mc simulation.

3.8 B_s signal selection with multivariate analysis

The signal variables described in Sec. 3.5 are used as inputs to a BDT discriminator. In this way it is possible to obtain the best separation, enhancing the significance of the signals.

Definition	Invariant mass range in GeV
overall mass window	[4.9,5.9]
low side-band	[5.1,5.2]
signal window	[5.27,5.47]
high side-band	[5.5,5.6]

Table 3.6: Invariant mass region definitions for the control channel.

Variable	minimum	maximum	unit
$p_{T,B}$	5.0	9999.0	GeV
p_{T,μ_1}	4.0	999.0	GeV
p_{T,μ_2}	4.0	999.0	GeV
l_{3D}	-	2.0	cm
$l_{3D}/\sigma(l_{3D})$	0.0	200.0	-
$l_{xy}/\sigma(l_{xy})$	3.0	-	-
χ^2/dof	-	20.0	-
l_z	-	1.0	cm
$l_z/\sigma(l_z)$	-	5.0	-
δ_{3D}	-	0.1	cm
$\delta_{3D}/\sigma(\delta_{3D})$	-	5.0	-
d_{ca}^0	-	0.1	cm
α_{3D}	-	1.0	-
I	0.0	-	-
N_{trk}	-	21.0	-
d_{ca}^{max}	-	0.25	-

Table 3.7: Preselection cuts for BDT training.

3.8.1 Preselection

Before the BDT analysis, a loose preselection is required. Furthermore, the preselection may have an influence on the MVA performance, so it is optimized to obtain the best separation. In Table 3.7, the applied preselection requirements are summarized.

3.8.2 Event sample splitting

Given the huge amount of collected data, it is not possible to use a comparable statistics from a MC simulation for background sample training in BDT. Thus, the data dimuon mass side-band events are used (see Table 3.4 for the definition of the side-bands). It

45

is absolutely important to avoid any possible bias. To avoid a possible systematic effect while using background events from data side-bands, they are split into three distinct subsets and three different BDTs are used respectively:

- *subset-0*: analyzed by BDT-0, trained on subset-1 events, tested on subset-2 events

- *subset-1*: analyzed by BDT-1, trained on subset-2 events, tested on subset-0 events

- *subset-2*: analyzed by BDT-2, trained on subset-0 events, tested on subset-1 events

The division of the event sample into different types is based on the event number, that is checked to yield an unbiased splitting.

3.9 Background estimation

The combinatorial background basically arises from two reconstructed muons (which are real or misidentified hadrons), originating from separate particle decays. It is possible to estimate the combinatorial contribution under the signal peaks from the high side-band (in data), where no resonant decays are expected. In the Unbinned Maximum Likelihood (UML) fit, this background is parametrized with a linear function (which is shown in Sec. 3.9.1). The total contributions of the rare backgrounds are normalized to the reconstructed $B^{\pm}$ yield in data using the following formula:

$$N(X) = \frac{B(X)}{B(B^{\pm} \rightarrow J/\psi K^{\pm}) \times B(J/\psi \rightarrow \mu^{+}\mu^{-})} \times \frac{f_X}{f_u} \times \frac{\epsilon_X}{\epsilon_{B^{\pm}}} \times N_{obs}^{B^{\pm}} \tag{3.7}$$

where X is the given rare decay, f_X is the corresponding hadronization probability and ϵ_X is the analysis efficiency (which includes acceptance and reconstruction efficiencies respectively). The resulting event yields $N(X)$ are weighted with the corresponding muon misidentification rate for kaons, pions and protons. Table 3.8 shows the BF of the rare background decays studied in this analysis. Figure 3.9 and Figure 3.10 show the expected distributions of rare backgrounds in the barrel and endcap categories.
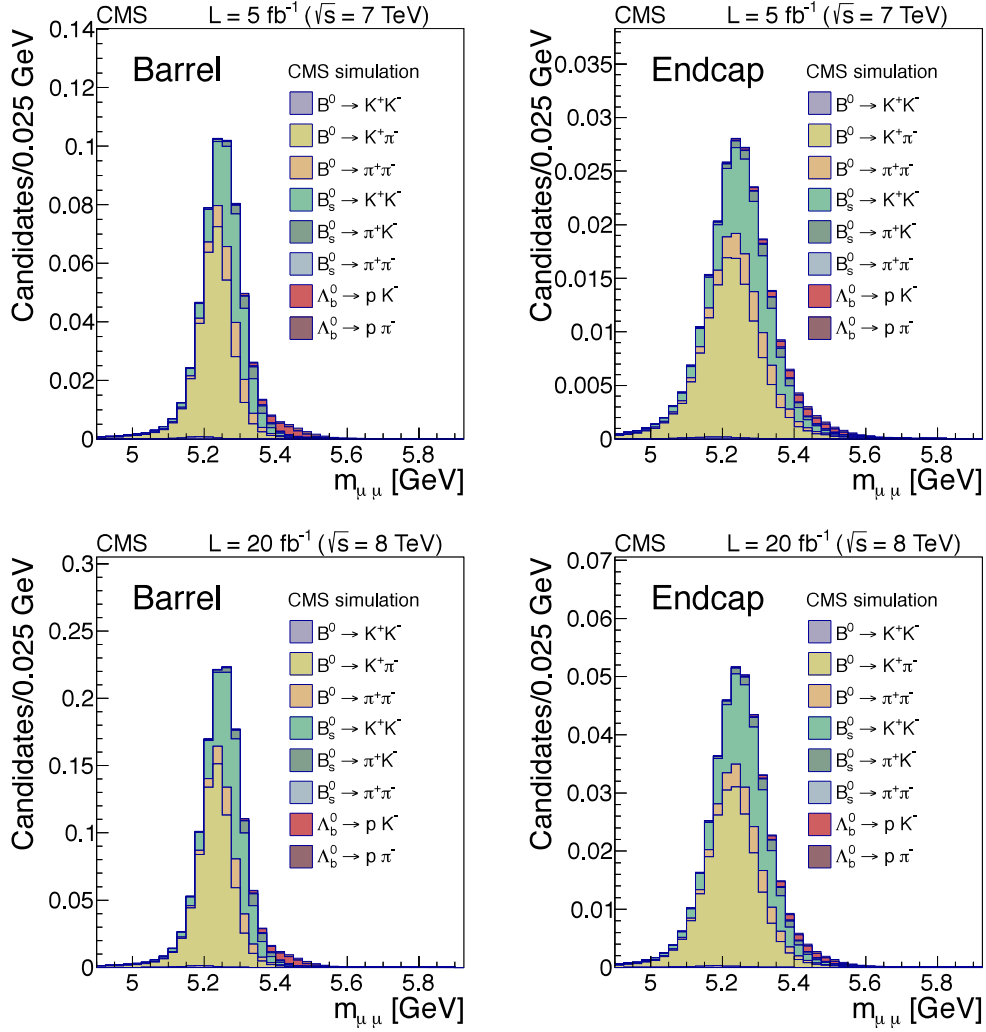
Figure 3.9: Invariant mass distributions of rare peaking backgrounds for 2011 (top) and 2012 (bottom) in barrel (left) and endcap (right) region.
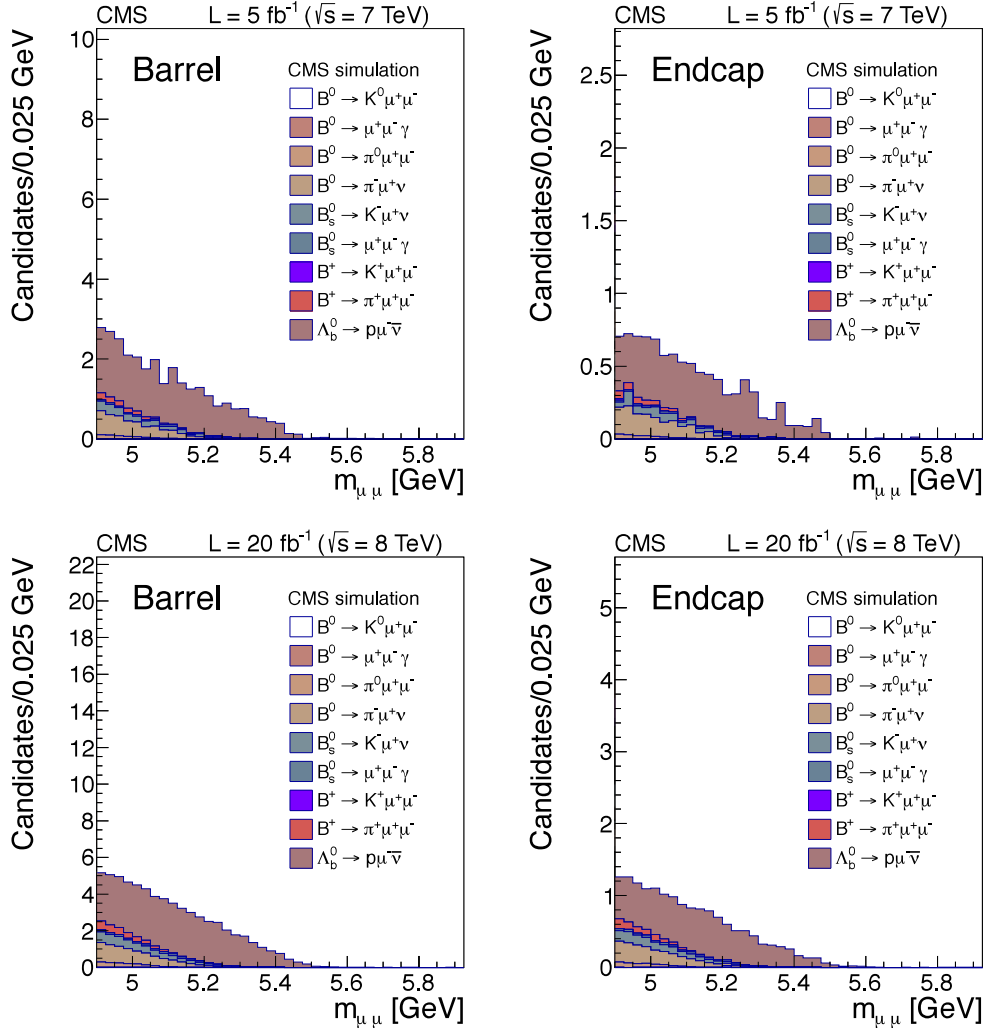
Figure 3.10: Invariant mass distributions of rare semileptonic *B* decays for 2011 (top) and 2012 (bottom) in barrel (left) and endcap (right) region.

Decay	Branching fraction ($\mathcal{B}$)
$B_s \to K^+K^-$	$2.54 \pm 0.38 \times 10^{-5}$
$B_s \to K^+\pi^-$	$5.00 \pm 1.10 \times 10^{-6}$
$B_s \to \pi^+\pi^-$	$7.30 \pm 1.40 \times 10^{-7}$
$B^0 \to K^+K^-$	$1.30 \pm 1.00 \times 10^{-7}$
$B^0 \to K^+\pi^-$	$1.95 \pm 0.06 \times 10^{-5}$
$B^0 \to \pi^+\pi^-$	$5.11 \pm 0.22 \times 10^{-6}$
$\Lambda_b^0 \to p\pi^-$	$3.50 \pm 1.00 \times 10^{-6}$
$\Lambda_b^0 \to pK^-$	$5.50 \pm 1.40 \times 10^{-6}$
$B_s \to K^-\mu^+\nu_\mu$	$1.42 \pm 0.07 \times 10^{-4}$
$B^0 \to \pi^-\mu^+\nu_\mu$	$1.42 \pm 0.07 \times 10^{-4}$
$\Lambda_b^0 \to p\mu^-\bar{\nu}_\mu$	$6.50 \pm 6.50 \times 10^{-4}$
$B^\pm \to \pi^\pm\mu^+\mu^-$	$2.30 \pm 0.60 \times 10^{-4}$
$B^\pm \to K^\pm\mu^+\mu^-$	$4.80 \pm 0.40 \times 10^{-7}$
$B^0 \to \pi^0\mu^+\mu^-$	$1.20 \pm 0.60 \times 10^{-8}$
$B^0 \to K^0\mu^+\mu^-$	$3.80 \pm 0.80 \times 10^{-7}$
$B^0 \to \mu^+\mu^-\gamma$	$1.34 \pm 0.27 \times 10^{-10}$
$B_s \to \mu^+\mu^-\gamma$	$1.89 \pm 0.38 \times 10^{-8}$

Table 3.8: Branching ratios of the rare backgrounds.

The systematic uncertainties on amount of rare (peaking and non-peaking) backgrounds arise from two sources, (i) the uncertainty on the muon misidentication probability and (ii) from the branching fractions. A 50% relative uncertainty is assigned on the pion, kaon, and proton fake rates. The knowledge about branching fractions varies considerably: some of them are known at the few percent level, some other have not been measured, but the theory prediction gives a number, while for others ($\Lambda_b^0 \to p\mu^-\bar{\nu}_\mu$, in particular) not even the model-based expectations agree and the resulting uncertainties are basically 100%.

3.9.1 Unbinned maximum likelihood fit analysis

In the UML fit, there are four contributions to the total mass yield: (i) $B_s \to \mu^+\mu^-$ signal yield, (ii) $B_d^0 \to \mu^+\mu^-$ signal yield, (iii) combinatorial background and rare background (subdivided into semileptonic and peaking contributions). The shape parameters of every contribution, except the combinatorial one, are fixed to MC simulation events. The num-

ber of events of each non-rare contribution is left floating, to be fitted to the unblinded event yield, while the rare contribution yields are constrained to the expectations. Thus, the mass likelihood of each independent category is:

$$L = N_{B_s} F_{B_s} + N_{B_d^0} F_{B_d^0} + N_{comb} F_{comb} + N_{peak} F_{peak} + N_{semi} F_{semi} \qquad (3.8)$$

where N_i is the yield and F_i is the corresponding pdf for each contribution i. A Per-Event Error (PEE) pdf is implemented because the width parameters of the B_s and B_d^0 mesons are not constant, but rather they are taken from the candidate mass error (σ_η) for each event. To avoid any dependence between (σ_η) and the mass of the candidate, since the detector resolution has a linear dependence with respect to the dimuon invariant mass, we divide the mass error by the event mass value, obtaining a "reduced" mass error: $\sigma(\eta)_r \equiv \sigma(\eta)/m$.

3.10 Results

After the final choice of all selections, the analysis is "unblinded": the blind window (Table 3.4) is opened and the results on the searches for the B_s and B_d^0 mesons can be extracted. Table 3.9 shows the final efficiencies ϵ_i for each category. In Figure 3.11 the unblinded dimuon invariant mass distribution in the barrel and endcap categories are shown. In Figure 3.12 the same final events are shown in a 2D plot of BDT output versus invariant mass. The expected MC distributions for the $B_s \to \mu^+\mu^-$ candidates are superimposed to the data distributions. These invariant mass distributions are given to the binned analysis (Sec. 3.10.1) and to the unbinned likelihood fit (Sec. 3.10.2) to extract the final $\mathcal{B}(B_s \to \mu^+\mu^-)$ and $\mathcal{B}(B_d^0 \to \mu^+\mu^-)$ results, respectively. The expected and observed yields in the two blind windows are shown, together with the NS yields, in Table 3.10. The observed numbers of candidates in each category are within one or two standard deviations close to the expected values.

Efficiency	Barrel 2011	Endcap 2011	Barrel 2012	Endcap 2012
$B_s \to \mu^+\mu^-$				
A	0.034 ± 0.001	0.024 ± 0.001	0.033 ± 0.001	0.024 ± 0.001
ϵ_{ana}	0.229 ± 0.007	0.170 ± 0.005	0.196 ± 0.006	0.103 ± 0.003
ϵ_{reco}	0.47 ± 0.02	0.66 ± 0.05	0.57 ± 0.02	0.65 ± 0.05
ϵ_{trig}	0.83 ± 0.03	0.73 ± 0.04	0.63 ± 0.02	0.61 ± 0.04
$\epsilon[10^{-2}]$	0.30 ± 0.04	0.20 ± 0.02	0.23 ± 0.03	0.09 ± 0.01
$B^{\pm} \to J/\psi K^{\pm} \to \mu^+\mu^- K^{\pm}$				
A	0.010 ± 0.001	0.005 ± 0.001	0.011 ± 0.001	0.006 ± 0.001
ϵ_{ana}	0.25 ± 0.01	0.19 ± 0.01	0.23 ± 0.01	0.13 ± 0.01
ϵ_{reco}	0.50 ± 0.02	0.60 ± 0.05	0.60 ± 0.02	0.56 ± 0.05
ϵ_{trig}	0.77 ± 0.02	0.60 ± 0.04	0.95 ± 0.02	0.49 ± 0.03
$\epsilon[10^{-2}]$	0.098 ± 0.008	0.036 ± 0.004	0.082 ± 0.007	0.021 ± 0.003

Table 3.9: Final efficiencies for the signal and normalization channels.

Category	$N_{B^0}^{obs}$	$N_{B^0}^{exp}$	$N_{B_s^0}^{obs}$	$N_{B_s^0}^{exp}$	$N_{B^{\pm}}^{obs}$
Barrel 2011	1.3 ± 0.8	3	3.6 ± 0.6	4	$(71.2 \pm 4.1) \times 10^3$
Endcap 2011	1.5 ± 0.6	1	2.6 ± 0.5	4	$(21.4 \pm 1.1) \times 10^3$
Barrel 2012	7.9 ± 3.0	11	7.9 ± 2.8	16	$(309 \pm 16) \times 10^3$
Endcap 2012	2.2 ± 0.8	3	5.1 ± 0.7	4	$(69.3 \pm 3.5 \times 10^3)$

Table 3.10: Expected and observed number of signal and background events in the B_d^0 and B_s mass windows, in the four 1D-BDT categories. Last row shows the fitted normalization sample(NS) yield $N_{B^{\pm}}^{obs}$ with its uncertainty.

51
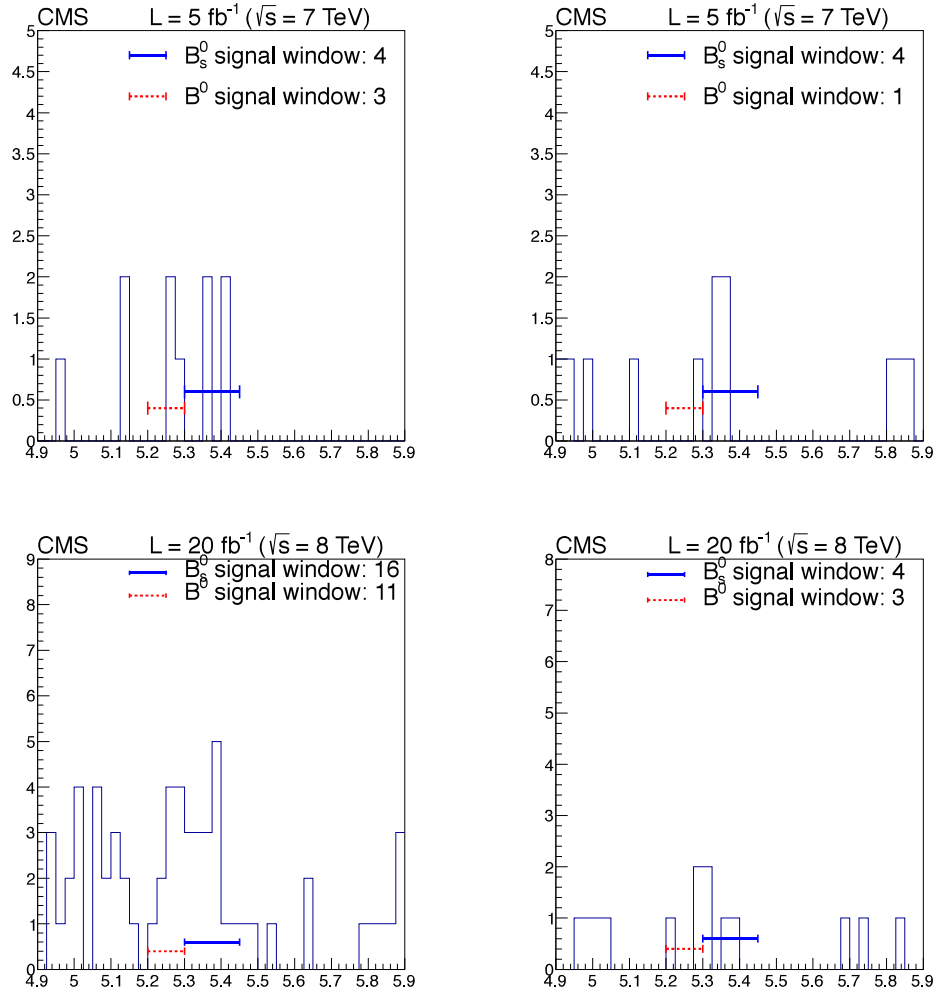
Figure 3.11: Dimuon invariant mass distribution for 2011 (top) and 2012 (bottom) in the barrel (left) and the endcap channel (right).
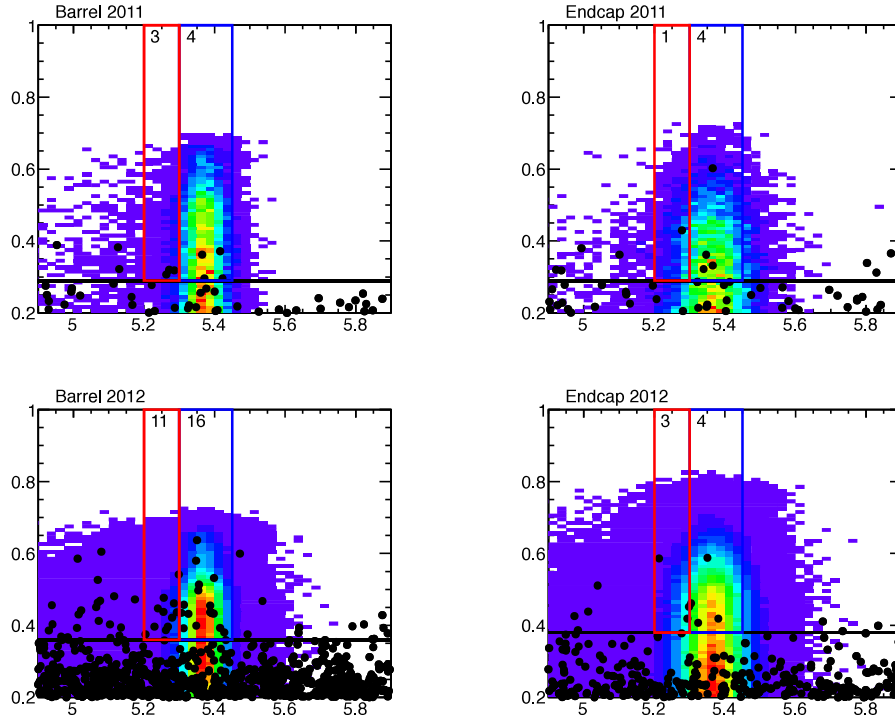
Figure 3.12: Analysis BDT output versus the dimuon invariant mass distributions or 2011 (top) and 2012 (bottom) in the barrel (left) and the endcap channel (right). The horizontal black line corresponds to the 1D-BDT selection. The red and blue lines present the B_d^0 and B_s blind windows, respectively. The numbers of observed events in these ranges are shown on the top. The colored histograms show the distributions for the $B_s \to \mu^+\mu^-$ signal MC.

3.10.1 Results with the binned analysis

These results are evaluated using the binned CL_s method, that gives the following upper limits:

$$\mathcal{B}(B_s \to \mu^+\mu^-) \leq 4.9 \times 10^{-9} \qquad \text{at 95\% CL} \tag{3.9}$$

$$\mathcal{B}(B_d^0 \to \mu^+\mu^-) \leq 1.1 \times 10^{-9} \qquad \text{at 95\% CL} \tag{3.10}$$

If the observed excess is assumed from a signal, the branching fractions can be measured to be

$$\mathcal{B}(B_s \to \mu^+\mu^-) = (2.6^{+1.2}_{-1.0}) \times 10^{-9} \tag{3.11}$$

$$\mathcal{B}(B_d^0 \to \mu^+\mu^-) = (4.9^{+3.1}_{-2.7}) \times 10^{-10} \tag{3.12}$$

where the errors are related to the standard 1σ uncertainty.

3.10.2 Results with the UML fit

The UML simultaneous fit technique is performed on the unblinded data for both methods. Results of the fitting are shown in Figure 3.13 for the 1D-BDT method, and in Figure 3.14 for the categorized BDT method.

For the categorized BDT fit, the measured signal branching fractions are:

$$\mathcal{B}(B_s \to \mu^+\mu^-) = (3.0^{+1.0}_{-0.9}) \times 10^{-9} \tag{3.13}$$

$$\mathcal{B}(B_d^0 \to \mu^+\mu^-) = (3.5^{+2.1}_{-1.8}) \times 10^{-10} \tag{3.14}$$

and the significances for the alternative hypotheses are:

$$sign(\mathcal{B}(B_s \to \mu^+\mu^-)) = 4.3\sigma \tag{3.15}$$

$$sign(\mathcal{B}(B_d^0 \to \mu^+\mu^-)) = 2.0\sigma \tag{3.16}$$

The significance, given no $\mathcal{B}(B_s \to \mu^+\mu^-)$ nor $\mathcal{B}(B_d^0 \to \mu^+\mu^-)$ decays is:

$$sign(\mathcal{B}(B_s \to \mu^+\mu^-)) \cap sign(\mathcal{B}(B_d^0 \to \mu^+\mu^-)) = 4.7\sigma \qquad (3.17)$$
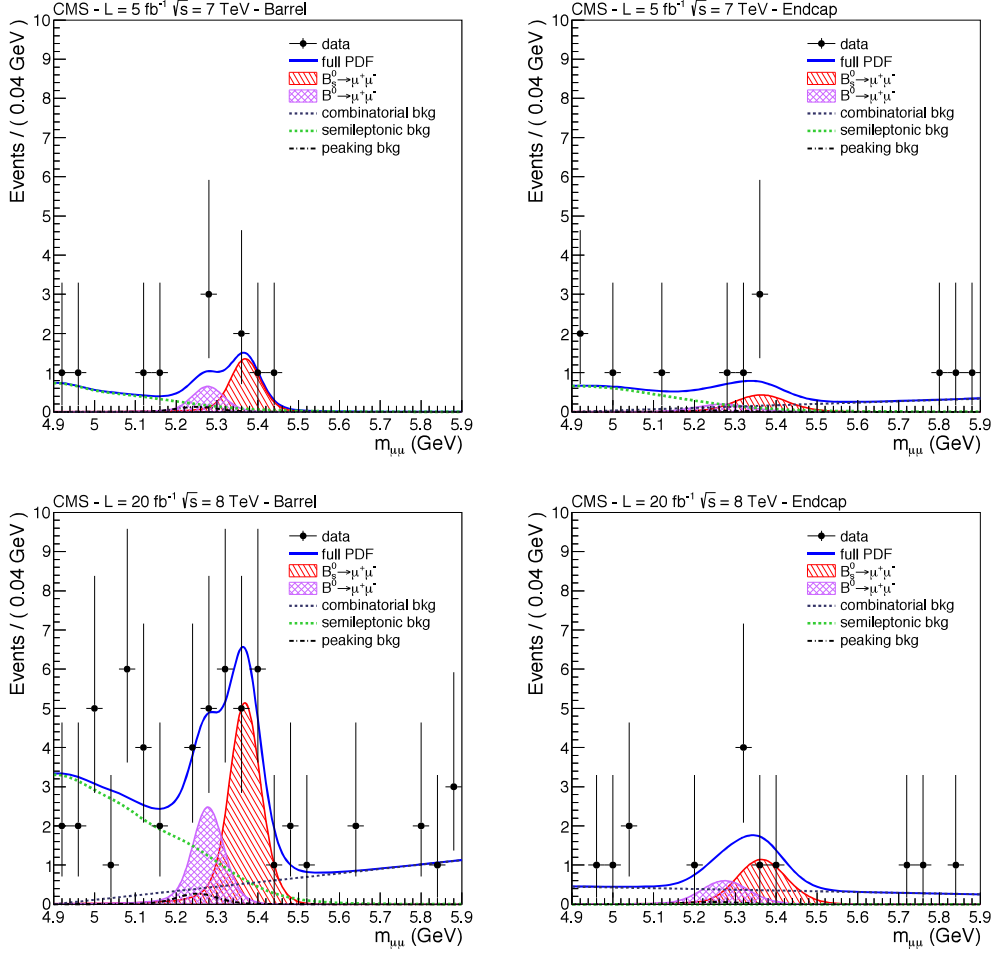
Figure 3.13: 1D fit result on the dimuon invariant mass distribution for 2011 (top) and 2012 (bottom) in the barrel (left) and the endcap channel (right).

The profile likelihoods, from which the significances of the alternative hypothesis are extracted, are shown in Figure 3.15 for both branching fractions.

$$\mathcal{B}(B_s \to \mu^+\mu^-) = (3.0^{+0.9}_{-0.8}(stat.)^{+0.6}_{-0.4}(syst.)) \times 10^{-9} \qquad (3.18)$$
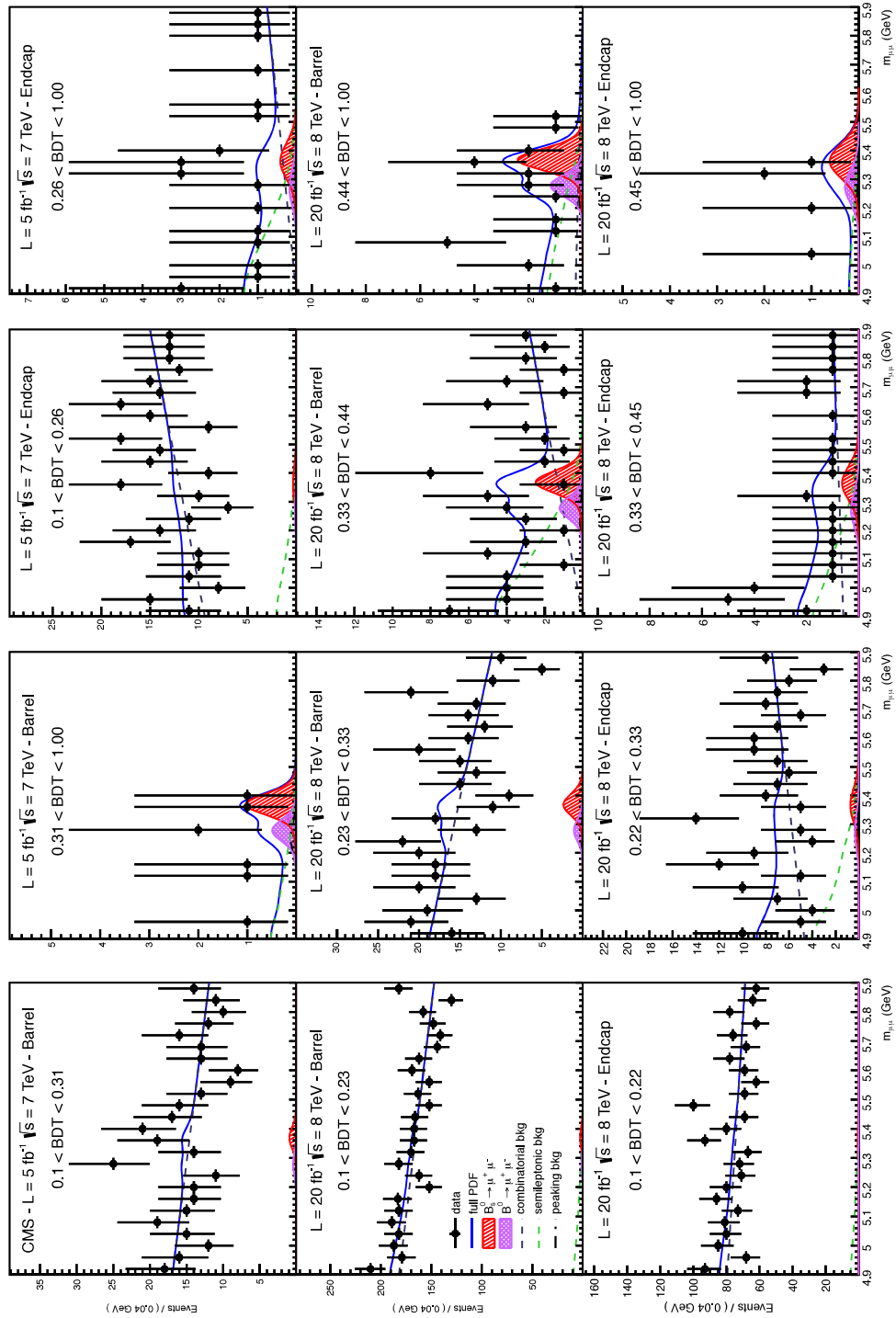
Figure 3.14: Categorized BDT fit result. The top row shows the 2011 samples, divided in two barrel and two endcap categories. The middle row displays the four 2012 barrel categories and the bottom row the four 2012 endcap categories.

The $B_s \to \mu^+ \mu^-$ BF uncertainty is statistically dominated. For the 1D-BDT method, the $B_s \to \mu^+ \mu^-$ BF significance is $\mathrm{sign}(\mathcal{B}(B_s \to \mu^+ \mu^-)) = 4.8\sigma$ and the double null hypothesis significance is $\mathrm{sign}(\mathcal{B}(B_s \to \mu^+ \mu^-) \cap \mathcal{B}(B_d^0 \to \mu^+ \mu^-)) = 5.4\sigma$.

As illustration, Figure 3.16 shows all data from the different categories, combined together. For these plots, the individual categories are weighed with $w = S/(S + B)$, where S is the signal yield and B is the background yield, determined at the B_s peak position of each category. The overall normalization is set such that the fitted B_s signal corresponds to the total yield of the individual contributions.
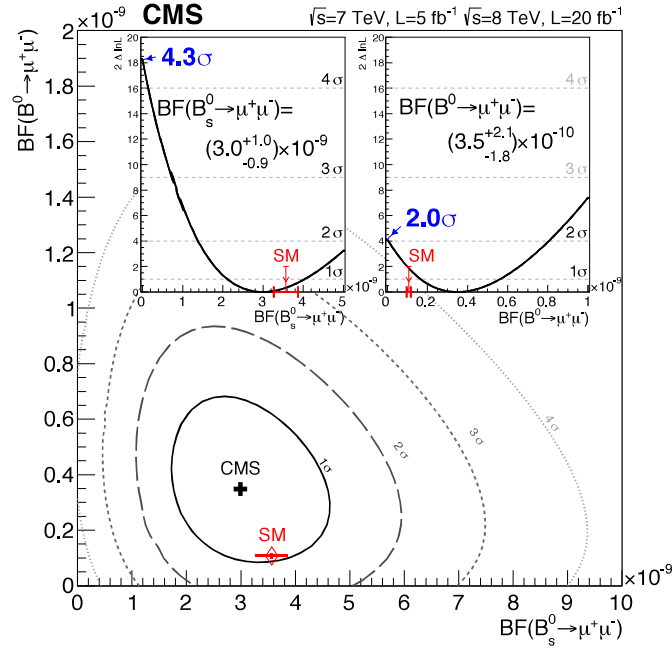
Figure 3.15: Categorized BDT method: scan of the ratio of the joint likelihood for $\mathcal{B}(B_s \to \mu^+ \mu^-)$ and $\mathcal{B}(B_d^0 \to \mu^+ \mu^-)$.

3.10.3   Interpretation of results

With the LHC run 1 data it has been finally possible to measure the $B_s \to \mu^+ \mu^-$ decay after decades of experimental efforts. This striking result has been obtained, because of the large amount of events produced by the LHC in just two years of excellent run operations. The high performances of the CMS detector, especially the silicon tracker and muon
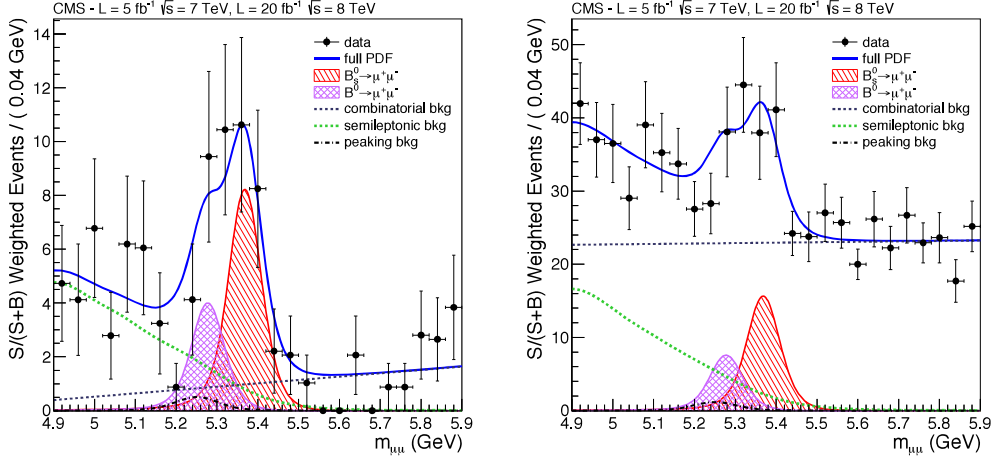
Figure 3.16: Weighted invariant mass distributions, based on $S/(S + B)$, for the 1D-BDT and categorized BDT methods respectively.

stations, allowed for a very high muon reconstruction efficiency and high geometrical coverage. This is especially true for the low p_T muons that are used in this analysis. The strong fake muon rejection and the high separation between signals and background sources have been achieved due to the BDT techniques applied on the muon and candidate variables. This sample of almost pure muons allowed the maximum likelihood fit to extract a clear signal with a remarkable significance.

The $B_s \to \mu^+\mu^-$ BF measurement is fully compatible with the SM expectation. A lower significance is obtained than expected (4.3σ instead of 4.8σ, since the measured BF is slightly lower than the SM value, but within uncertainty. The $B_d^0 \to \mu^+\mu^-$ BF measurement is three times the SM expectations. The $B_d^0 \to \mu^+\mu^-$ upper limit evaluated with the CL_s method is set to $\mathcal{B}(B_d^0 \to \mu^+\mu^-) \leq 1.1 \times 10^{-9}$ at 95% CL, ten times higher than the SM expectation value.

3.10.4 CMS and LHCb combination

After the CMS results were published, the LHCb collaboration published a new measurement of f_s/f_d [33]:

$$f_s/f_d = 0.259 \pm 0.015 \qquad (3.19)$$

58

By considering this new f_s/f_d value, the $\mathcal{B}(B_s \to \mu^+\mu^-)$ result of Eq. 3.13 changes very slightly which uses $f_s/f_d = 0.256 \pm 0.020$ from Eq. 3.3.

Along with the CMS collaboration, the LHCb collaboration also reported at the same time the measurement of the $B_s \to \mu^+\mu^-$ decay with 4σ significance and the $B_d^0 \to \mu^+\mu^-$ decay with 2σ significance [34].

$$\mathcal{B}(B_s \to \mu^+\mu^-) = (2.9^{+1.1}_{-1.0}(stat)^{+0.3}_{-0.1}(syst)) \times 10^{-9} \qquad (3.20)$$

$$\mathcal{B}(B_d^0 \to \mu^+\mu^-) = (3.5^{+2.1}_{-1.8}) \times 10^{-10} \qquad (3.21)$$

Since both the collaborations report the measurement of the $B_s \to \mu^+\mu^-$ BF with same Run1 data, a joint analysis was performed and reported the first observation of $B_s \to \mu^+\mu^-$ decay with significance more than 6σ for B_s signal [35].

$$\mathcal{B}(B_s \to \mu^+\mu^-) = (2.8^{+0.7}_{-0.6}) \times 10^{-9} \qquad (3.22)$$

$$\mathcal{B}(B_d^0 \to \mu^+\mu^-) = (3.9^{+1.6}_{-1.4}) \times 10^{-10} \qquad (3.23)$$

where the uncertainties included both statistical and systematic sources. The statistical significance was computed to be 6.2σ for $B_s \to \mu^+\mu^-$ decay mode and 3.2σ for $B_d^0 \to \mu^+\mu^-$ mode respectively. The results are shown in Figures 3.17-3.18.

The combined analysis explored the statistical power of data from both CMS and LHCb, established the existence of $B_s \to \mu^+\mu^-$ decay and provided an improved measurement till date. The measured BFs of both the decays are compatible with SM predictions.
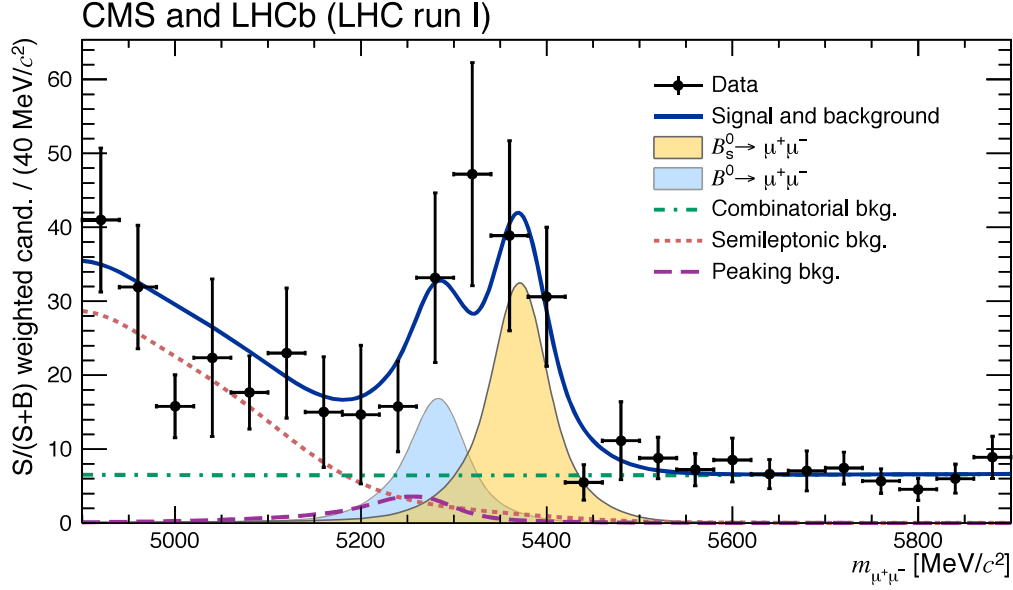
Figure 3.17: Weighted distribution of the dimuon invariant mass for all categories. Superimposed on the data points in black are the combined fit (solid blue) and its components: the B_s^0 (yellow shaded) and B^0 (light-blue shaded) signal components; the combinatorial background (dash-dotted green); the sum of the semileptonic backgrounds (dotted salmon); and the peaking backgrounds (dashed violet).
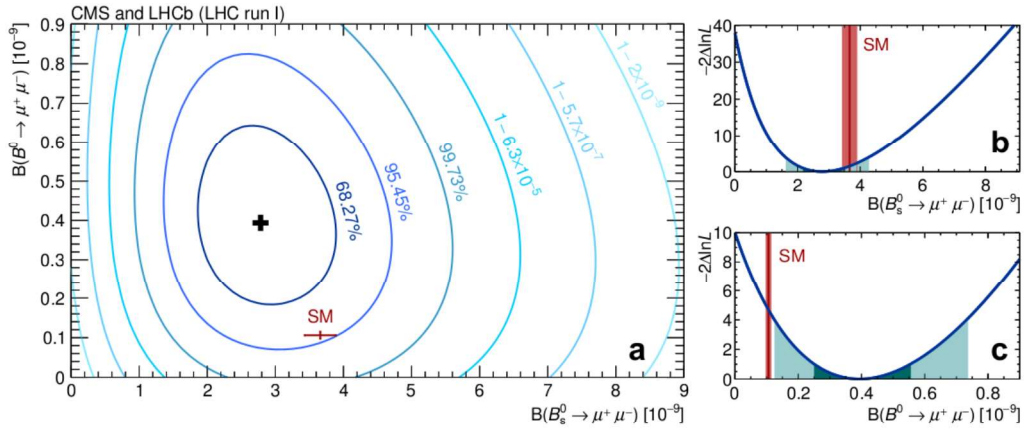
Figure 3.18: CMS and LHCb combined result showing the likelihood contours in $\mathcal{B}(B^0 \rightarrow \mu^+\mu^-)$ versus $\mathcal{B}(B_s^0 \rightarrow \mu^+\mu^-)$ plane. Also shown are the variations of the test statistics for $\mathcal{B}(B^0 \rightarrow \mu^+\mu^-)$ and $\mathcal{B}(B_s^0 \rightarrow \mu^+\mu^-)$.

Chapter 4

Angular Analysis of the decay
$B^+ \rightarrow K^{*+}\mu^+\mu^-$

4.1 Introduction

The process $B^+ \rightarrow K^{*+}\mu^+\mu^-$, sketched in Figure 4.1, is a flavour changing neutral current decay. In the Standard Model (SM) such decays are suppressed, as they can only proceed via loop processes involving electroweak penguin or box diagrams as shown in Figure 4.2 [36, 37]. As-yet undiscovered particles could give additional contributions with comparable amplitudes, making the decay a sensitive probe of new phenomena. A number of angular observables in $B^+ \rightarrow K^{*+}\mu^+\mu^-$ decay can be theoretically predicted with a relatively good control of the relevant form factor uncertainties especially in the low and high dimuon invariant mass regions, *i.e.* far from the J/ψ and ψ' resonances. These include the forward-backward asymmetry of the muons, A_{FB} and the longitudinal polarization of $K^{*+}(892)$, F_L as a function of the dimuon invariant mass squared (q^2) [38–42]. These observables have previously been measured for similar kind of analysis $B^0 \rightarrow K^{*0}\mu^+\mu^-$ by the BaBar, Belle, CDF and CMS experiments [43–45,50]. Still they are statistically limited and a precise determination of A_{FB} is of particular interest as, in the

61

$1 < q^2 < 6\,\mathrm{GeV/c^2}$ region, the form factor ratio used in the calculation of the zero-crossing point is almost free of hadronic uncertainties.
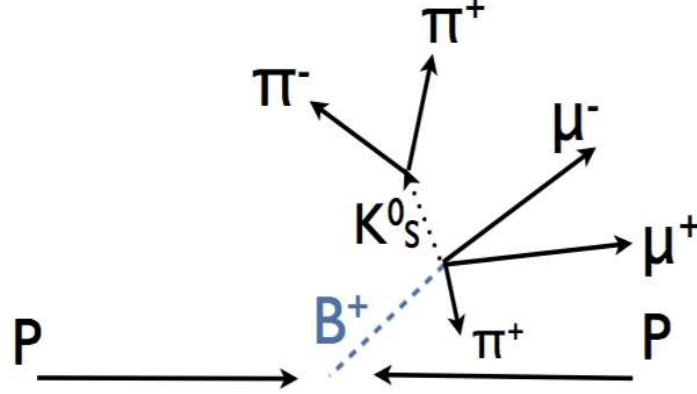
Figure 4.1: Topological features of the $B^+ \to K^{*+}\mu^+\mu^-$ decay: B^+ detached secondary vertex decaying into a fully charged final state defined by particle tracks.

This thesis presents the measurements of A_{FB} and F_L performed with the Compact Muon Solenoid (CMS) experiment at the CERN LHC [46] during 2012 at the center of mass energy of 8 TeV. The amount of analyzed data corresponds to an integrated luminosity of $19.98\ fb^{-1}$ [47] corresponding to 8 TeV center of mass energy.
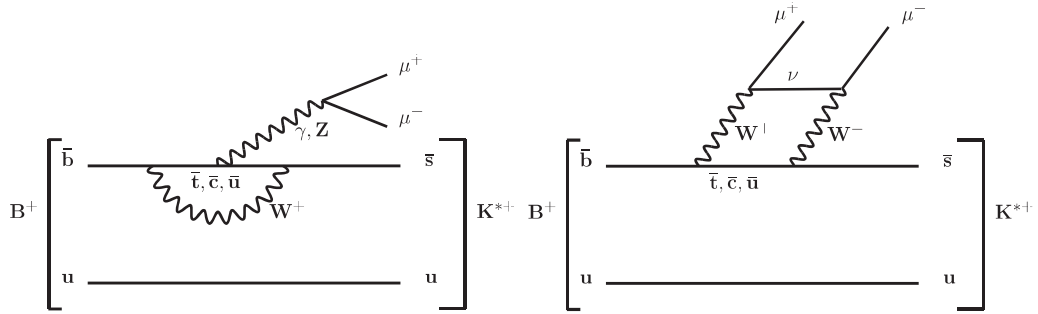
Figure 4.2: Dominant Standard Model Feynman diagrams for the decay $B^+ \to K^{*+}\mu^+\mu^-$. The first one is the penguin diagram whereas the second is the box diagram.

The K^{*+} is reconstructed through its decay into $K_s\pi^+$ and the B^+ is reconstructed by fitting two muons and K^{*+} to a common vertex. A_{FB} and F_L are measured by fitting the event distribution as a function of two angular variables, the angle between the positive charged muon and the B^+ in the dimuon reference frame, and the angle between the

kaon and the B^+ in the K^{*+} reference. The measurements are performed in bins of the dimuon invariant mass squared (q^2) and the results are compared with SM predictions. The analysis includes both CP-conjugate states of B^+ and B^- in the reconstruction.

4.2   Primary datasets and trigger used

The analysis is performed with the parked dataset recorded during the 2012 pp collision but reconstructed and processed afterwards during the long shutdown(LS1) period, corrsponding to 8 TeV center of mass energy. The corresponding integrated luminosity calculated with the official recipe is 19.98 fb^{-1} . The good runs and luminosity sections are selected with the "MuonPhysics" JSON file applied on the following parked datasets.

- /DoubleMuParked/Run2012A-22Jan2013-v1/AOD

- /MuOniaParked/Run2012B-22Jan2013-v1/AOD

- /MuOniaParked/Run2012C-22Jan2013-v1/AOD

- /MuOniaParked/Run2012D-22Jan2013-v1/AOD

The luminosity of the datasets is computed with the officially recommended tool from the luminosity group `pixelLumiCalc.py`. The luminosity shown in Table 4.1 is per dataset after all processing including the JSON file.

The names of MC simulation datasets used in this analysis are listed below:

- `/BuToKstarMuMu_EtaPtFilter_8TeV-pythia6-evtgen/Summer12_DR53X-PU_RD2_START53_V19F-v1/AODSIM`

- `/BuToKstarMuMu_EtaPtFilter_8TeV-pythia6-evtgen/Summer12_DR53X-PU_RD2_START53_V19F-v2/AODSIM`

Sample	Events	$\mathcal{E}_{filter}$	Braching frac.	Lumi (fb^{-1})
Data				
Run2012A	6 432 930 (RECO)	N.A.	1.12×10^{-6}	0.923
Run2012B	60 037 388 (RECO)	N.A.	1.12×10^{-6}	4.811
Run2012C	130 542 135 (RECO)	N.A.	1.12×10^{-6}	6.614
Run2012D	146 890 724 (RECO)	N.A.	1.12×10^{-6}	7.631
Monte Carlo				
$B^+ \to K^{*+}\mu^+\mu^-$	126 345 475 (GEN)	2.4×10^{-4}	1.12×10^{-6}	37 378.629
$B^+ \to K^{*+}J/\psi$	75 808 840 (GEN)	2.5×10^{-4}	1.44×10^{-3}	295.761
$B^+ \to K^{*+}\psi'$	5 125 502 (GEN)	4.2×10^{-4}	6.7×10^{-4}	218.472
Background simulation				
$B^+ \to \psi(\mu^+\mu^-)X$	58 574 844 (GEN)	1.921×10^{-4}	N.A.	9.81

Table 4.1: Data and Monte Carlo simulation samples for both signal and control channels used in the analysis. The data are `MuOnia-AOD` datasets. The numbers listed in the branching fraction column are taken from the PDG.

- /BuToKstarJPsi_EtaPtFilter_8TeV-pythia6-evtgen/Summer12_DR53X-PU_RD2_START53_V19F-v1/AODSIM

- /BuToKstarJPsi_EtaPtFilter_8TeV-pythia6-evtgen/Summer12_DR53X-PU_RD2_START53_V19F-v2/AODSIM

- /BuToKstarPsi2S_EtaPtFilter_8TeV-pythia6-evtgen/Summer12_DR53X-PU_RD2_START53_V19F-v1/AODSIM

- /BuToKstarPsi2S_EtaPtFilter_8TeV-pythia6-evtgen/Summer12_DR53X-PU_RD2_START53_V19F-v2/AODSIM

- /BpToPsiMuMu_2MuPtEtaFilter_8TeV-pythia6-evtgen/Summer12_DR53X-PU_S10_START53_V7A-v1/AODSIM

Both signal ($B^+ \to K^{*+}\mu^+\mu^-$) and control samples ($B^+ \to K^{*+}J/\psi$ and $B^+ \to K^{*+}\psi'$) were recorded with the same double muon trigger which was especially designed to perform this analysis: **HLT_DoubleMu3p5_LowMass_Displaced**. This trigger covers the dimuon mass range from **1** to **4.8** GeV/c^2. The selections were optimized to maintain the highest possible efficiency given the rate limitations.

The most important selections to reduce the trigger rate are:

- single muon p_T greater than **3.5** GeV ;

- dimuon p_T greater than **6.9** GeV ;

- dimuon invariant mass window **1-4.8** GeV/c^2 ;

- the significance of the separation between dimuon vertex and beamspot in the transverse plane greater than **3**;

- the dimuon χ^2 vertex probability greater than **10%**.

where the p_T selection favors b-quark events from lighter quark events, the vertex probability rejects two muons from different vertices such as from a cascade decay of b to c to s or from a b-quark and anti-b-quark, and the vertex separation distinguishes dimuons from b-decays and from prompt muons.

The amount of data recorded by each dimuon trigger is computed with the officially recommended tool from the luminosity group `pixelLumiCalc.py`, version `V04-02-10`, with the option `lumibyls`(which means integrated luminosity delivered by LHC and recorded by CMS in each lumi section) and with the `JSON` file containing only the runs and lumisections used in this analysis and obtained with the `crab report` command.

The other pre-selection cuts applied at trigger level are:

- $|\eta^\mu| < $ **2.2**: muon pseudorapidity range;

- $DCA_{xy}^\mu < $ **2** cm: Distance of Closest Approach (DCA_{xy}^μ) between the muon momentum and the beamspot in the transverse plane;

- $DCA^{\mu\mu} < $ **0.5** cm: DCA in three dimensions between two muon momenta;

- $\cos(\alpha_{xy}^{\mu\mu}) > $ **0.9**: $\alpha_{xy}^{\mu\mu}$ is the angle in the transverse plane between the dimuon momentum and the separation between the dimuon vertex and the beamspot.

To validate the analysis technique a detailed study based on Monte Carlo (MC) simulations is performed. The simulation is also used to determine the efficiency, the systematic uncertainties and for a variety of systematic checks. The simulation samples used are shown in Table 4.1, they are generated with `PYTHIA MSEL = 1`, using the `EvtGen` package to perform the decay, and allowing for radiated photons using the PHOTOS package [48]. Particles are traced through a detailed model of the detector with `GEANT4` [49]. The samples were reconstructed within the framework tag `CMSSW_5_3`, with pileup distributions for signal and control samples respectively and with the same versions of the double muon trigger used to record the data, but `HLT_DoubleMu3p5_LowMass_Displaced` as explained later in the text in Sec. 4.3.

The MC simulation was generated in three steps:

GEN: pure generation level without any filter applied;

GEN-Filter: like the `GEN` step, but with also the B^+ filter (only events with B^+ (B^-) are retained) and the muon acceptance filter applied ($p_T^\mu > 2.8$ GeV and $|\eta^\mu| < 2.3$);

RECO: like the `GEN-Filter` step, but with also the full reconstruction applied, together with the pileup and the trigger simulation.

4.3   Reconstruction and Event Selection

The process $B^+ \to K^{*+}\mu^+\mu^-$, together with the two control channels $B^+ \to K^{*+}J/\psi$ and $B^+ \to K^{*+}\psi'$, are reconstructed through their decay into the fully charged final state $\pi^+\pi^-\pi^+ \mu^+\mu^-$ (with obvious generalization to the CP-conjugate states, which are implicitly considered throughout the whole analysis unless explicitly stated). Each event is required to pass one of the dimuon trigger versions described in Sec. 4.2. B^+ candidates are formed by combining a dimuon candidate with a K^{*+} candidate to a common vertex. Dimuon candidates are required to pass the triggers described in Sec. 4.2. Dimuon vertices are reconstructed from oppositely charged muon tracks which are selected ac-

cordingly to the `soft` muon selections officially recommended by the muon group and reported here for completeness:

- muon type: `TMOneStationTight`;

- tracker layers with measurement > **5**;

- pixel layers with measurement > **0**;

- normalized muon track $\chi^2 <$ **1.8**;

- distance of closest approach between the muon momentum and the primary vertex in the transverse plane < **0.3** cm;

- distance of closest approach between the muon momentum and the primary vertex along the beam line < **20** cm.

The pre-selection cuts applied in the analysis for muon tracks and dimuon vertices have the same values as those applied at trigger level accordingly to the dataset (see Table 4.1).

The K^{*+} candidate is reconstructed through its decay into a K_s and a pion. The hadron(pion) tracks are vetoed from being muons by rejecting all tracks which are `TrackerMuonArbitrated`. The K_s candidate is reconstructed through its decay into two pions with opposite charge as final states. These candidates are taken from the `generalV0Candidates_Kshort` list as reconstructed by the `RecoVertex/V0Producer` package. The following selection criteria are applied in that module:

- Track normalized $\chi^2 < 5$;

- Track number of hits ≥ 6;

- Track transverse impact parameter w.r.t the beamspot $> 1.2\sigma$ where σ includes the uncertainty from the track impact parameter and the beamspot (typical values have $\sigma \sim 200\mu$m with a large spread);

67
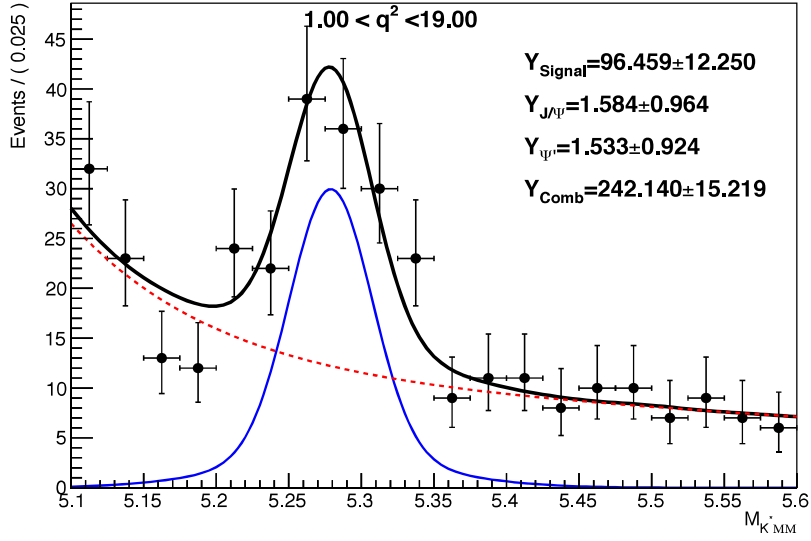
Figure 4.3: B^+ invariant mass from data, computed from the whole q^2 spectrum excluding the J/ψ and ψ' ranges as described in the text. Just to guide the eye, the plot is fitted with a double Gaussian with unique mean to measure the signal yield (96 ± 12 events) and with exponential to distinguish the background.
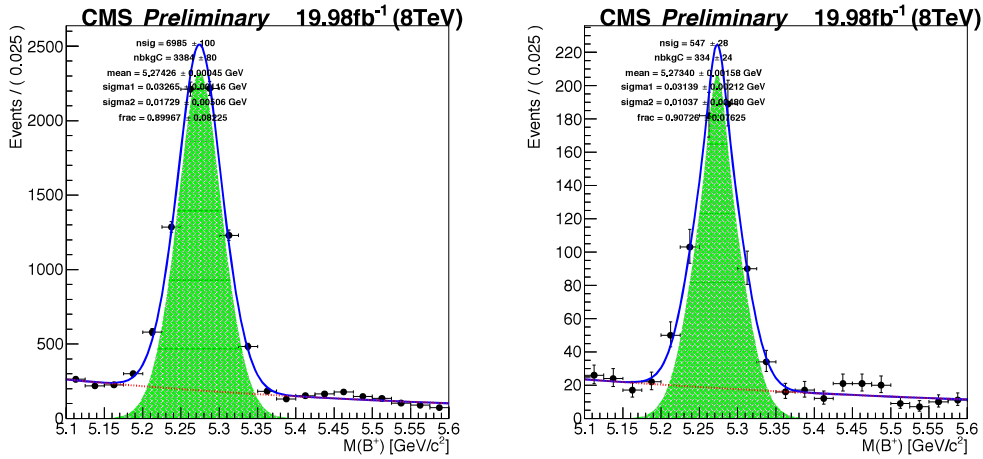
Figure 4.4: B^+ invariant mass for both control channels, $B^+ \to K^{*+}J/\psi$ (left) and $B^+ \to K^{*+}\psi'$ (right), from data. Just to guide the eye the plot is fitted with a double Gaussian with unique mean and an exponential pdf to describe the signal and the background respectively.

- Vertex significance $> 10\sigma$ from beamline;

- Vertex $\chi^2 < 7$.

For the K_s candidate reconstruction, all charged tracks are used out of which two oppositely charged tracks are fitted to a common vertex using a vertex constraint to improve the mass of K_s. Then the K_s candidate in conjunction with the hadron(pion) track and two muon tracks are fitted to a common vertex with a vertex constraint and also a mass constraint on the K_s mass. No mass constraint is applied to K^{*+} as the natural width is much larger than the experimental resolution. And the refitted tracks after the vertex and mass constraint are used to get the B^+ and K^{*+} masses. The K_s candidates have $p_T > 1.0$ GeV and the K^{*+} invariant mass must lie within 100 MeV/c^2 (which is two times its natural width) of the nominal K^{*+} mass. The detector resolution is small compared to the natural width. The K_s candidates having invariant mass within 80 MeV/c^2 of the K_s PDG mass value are saved. The hadron tracks are required to pass the following selections:

- $p_T^h > 0.4$ GeV: hadron(pion coming from K^{*+}) transverse momentum;

- $DCA_{xy}^h/\sigma > 0.4$: DCA_{xy}^h is the Distance of Closest Approach between the hadron(pion coming from K^{*+}) momentum and the beamspot in the transverse plane and σ is its uncertainty;

- $K_s p_T > 1.0$ GeV: K_s transverse momentum.

B^+ candidates are then reconstructed by fitting the two muons and K^{*+} candidates to a common vertex. The vertex-constrained B^+ fit allows to compute more accurate momenta and positions of the daughter particles, which are then used to calculate all other derived quantities, *i.e.* invariant masses, distances of closest approach and angular variables.

The B^+ candidates are required to pass the following selections:

- $CL(B^+-vtx) > 10\%$: B^+ vertex confidence level;

69

- $L_{xy}(B^+ - vtx)/\sigma > 12$: $L_{xy}(B^+ - vtx)$ is the transverse separation between the B^+ vertex and the beamspot and σ is its uncertainty;

- $\cos(\alpha_{xy}^{B^+}) > 0.9994$: $\alpha_{xy}^{B^+}$ is the angle in the transverse plane between the B^+ momentum and the separation between the B^+ vertex and the beamspot.
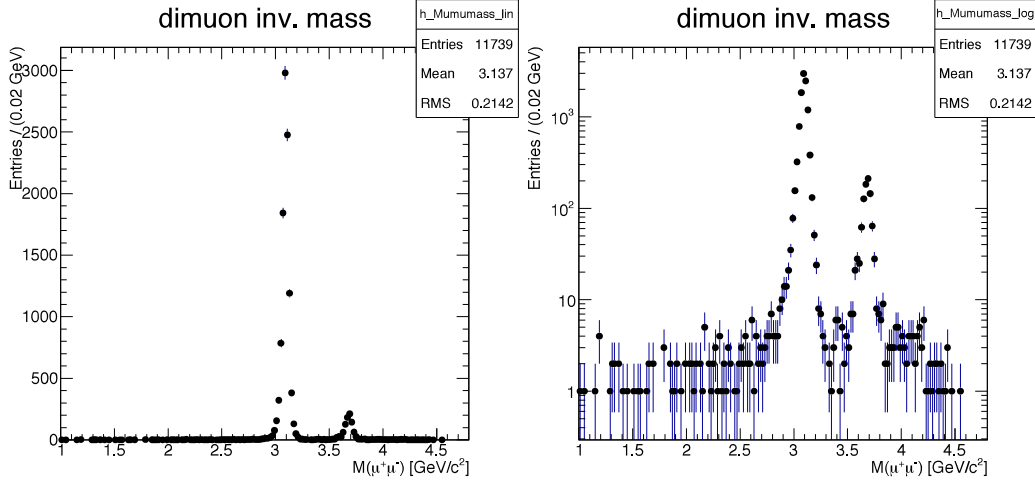
Figure 4.5: dimuon invariant mass plot from data: linear scale(left) and log scale(right). The first peak is for J/ψ and the second one is for ψ'.

After the selection process is done, we are left with 1.003 candidates per event out of which the choice of the best candidate among the multiple candidates per event is based on the best vertex fit probability.

All selection cuts that depend upon a reference point are referred to the **beamspot**, they are therefore independent from any choice of the primary vertex. The only exceptions are the distances of closest approach computed for the muon selection, but given their loose values they are not influenced by the choice of the primary vertex.

The B^+ invariant mass plots for signal and control channels from data are shown in Figure 4.3 and 4.4, the dimuon invariant mass spectrum is shown in Figure 4.5 while the invariant mass of the J/ψ and ψ' are shown in Figure 4.6. It's important to mention that no fit to K^{*+} mass spectrum is used in the analysis.
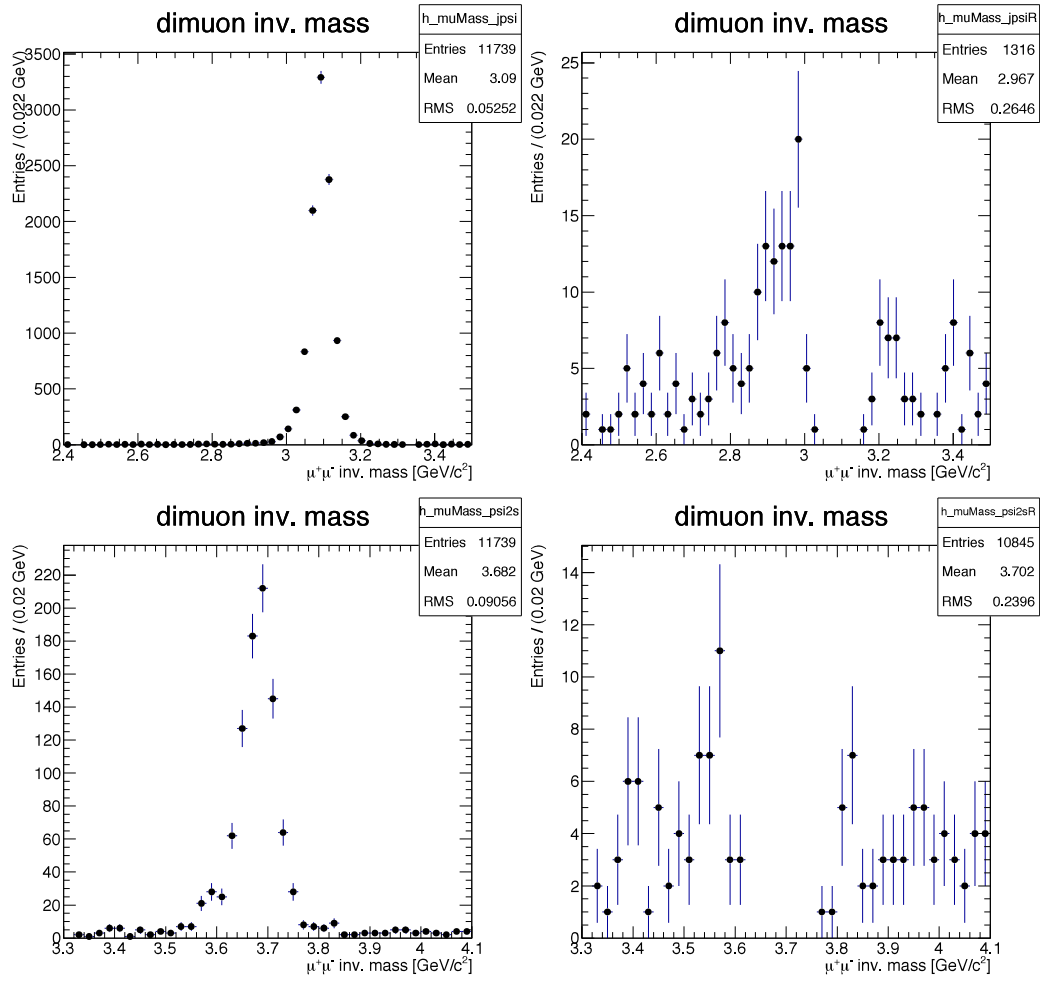
Figure 4.6: J/ψ (top two plots) and ψ' (bottom two plots) dimuon invariant mass regions from data shown for two different cases: before (two plots on the left column) and after (two plots on the right column) selecting the signal sample.

4.3.1 Possible peaking Backgrounds and Supressions

4.3.1.1 Resonance Rejection

The discrimination between signal, $B^+ \to K^{*+}\mu^+\mu^-$, and control channels, $B^+ \to K^{*+}J/\psi$ and $B^+ \to K^{*+}\psi'$, is based on the dimuon invariant mass. The signal sample is required to pass the selection:

- $\mathrm{m}(\mu\mu) < \mathrm{m}_{J/\psi\mathrm{PDG}} - 5.5\sigma_{\mathrm{m}(\mu\mu)}$ or

- $\mathrm{m}_{J/\psi\mathrm{PDG}} + 3.5\sigma_{\mathrm{m}(\mu\mu)} < \mathrm{m}(\mu\mu) < \mathrm{m}_{\psi'\mathrm{PDG}} - 3.5\sigma_{\mathrm{m}(\mu\mu)}$ or

- $\mathrm{m}(\mu\mu) > \mathrm{m}_{\psi'\mathrm{PDG}} + 3.5\sigma_{\mathrm{m}(\mu\mu)}$;

For the control channel $B^+ \to K^{*+}J/\psi$ the requirement is:

- $\mathrm{m}_{J/\psi\mathrm{PDG}} - 5\sigma_{\mathrm{m}(\mu\mu)} < \mathrm{m}(\mu\mu) < \mathrm{m}_{J/\psi\mathrm{PDG}} + 3\sigma_{\mathrm{m}(\mu\mu)}$;

while for the $B^+ \to K^{*+}\psi'$ channel is:

- $|\mathrm{m}(\mu\mu) - \mathrm{m}_{\psi'\mathrm{PDG}}| < 3\sigma_{\mathrm{m}(\mu\mu)}$.

The $\sigma_{\mathrm{m}(\mu\mu)}$ is the uncertainty on the measurement of the dimuon invariant mass. It is determined on candidate-by-candidate basis. The reason for an asymmetric interval selection cut around the J/ψ PDG mass is because the left-hand tail is more broaden than the right-hand one due to radiated photons in the decay (*i.e.* Final State Radiation - FSR), as one can see from Figure 4.6; the same is true for the ψ' region but given its reduced branching fraction the choice of having a symmetric ($\pm 3\sigma_{\mathrm{m}(\mu\mu)}$) selection cut is adopted.

4.3.1.2 Anti-radiation Cut

Some events from control channels still remain due to Final State Radiation(FSR) even after the resonance rejection cuts are applied. Since these processes have very huge branching ratio in comparison to the signal channel, we need to remove these events. This

72

method is very similar to CMS paper [50] and we call it as "anti-radiation cut" after-wards. This cut is applied in whole B^+ invariant mass region i.e, $5.1 < m(B) < 5.6$ GeV/c^2 and we require $|(m - m_{B^+}) - (m(\mu\mu) - m_{J/\psi(\psi')})| > 60(30)$ MeV/c^2 to reject the remaining $J/\psi(\psi')$ events. To help visualizing the effect of "anti-radiation cut", the scatter plots are shown in Figure 4.7.
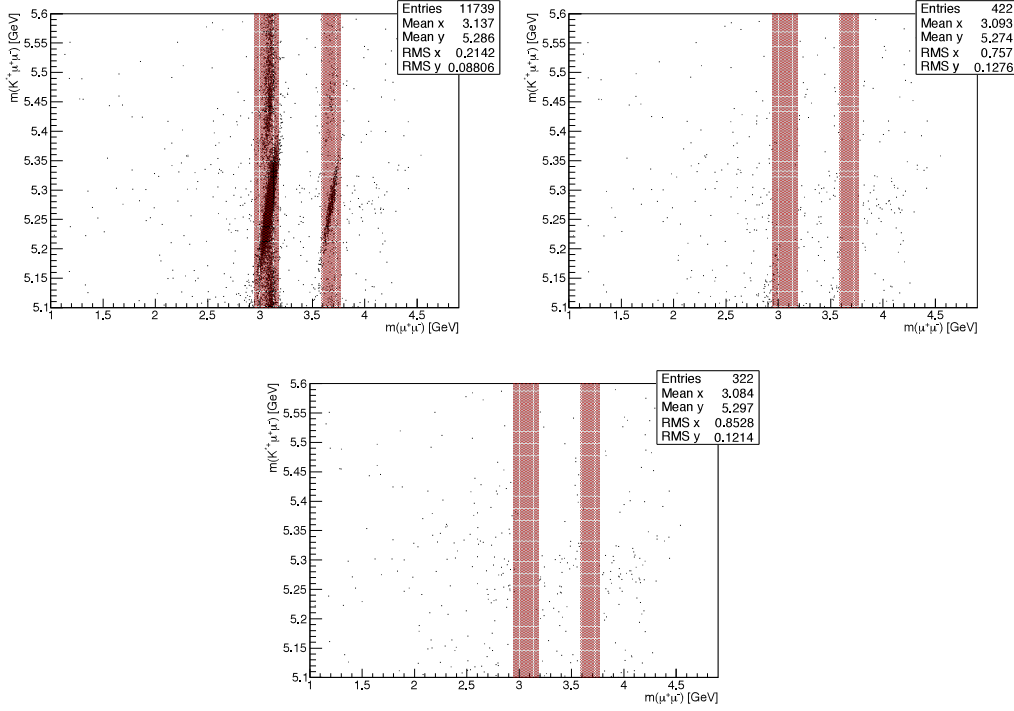
Figure 4.7: Scatter plot of event distribution in data in dimuon invariant mass, m($\mu\mu$) versus B invariant mass, m($K^*\mu\mu$). The first plot shows the events before both the J/ψ and ψ' rejection and the anti-radiation cuts are applied. The second plot shows the event distribution after the J/ψ and ψ' rejection and before ant-radiation cuts applied. The third plot shows the events after both J/ψ and ψ' rejection and anti-radiation cuts. The red shaded regions correspond to the J/ψ and ψ' bins, $2.946 < $ m($\mu\mu$) < 3.177 GeV/c^2 and $3.586 < $ m($\mu\mu$) < 3.766 GeV/c^2 respectively.

The aim of this cut is to reject the additional events still remaining although after the resonance rejection cuts mentioned on Sec. 4.3.1. The number of events remained after applying this cut in both signal and control simulation samples are shown in Figure 4.8,4.9 and 4.10 respectively.

By applying the anti-radiation cut, **98.9%** signal events are remained whereas **92.9%**
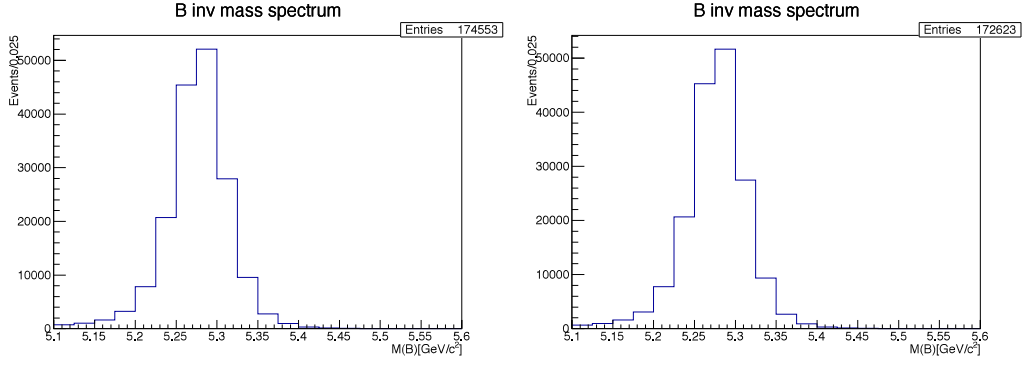
Figure 4.8: B mass distribution in $B^+ \rightarrow K^{*+}\mu^+\mu^-$ sample without and with antiradition cut(left to right)
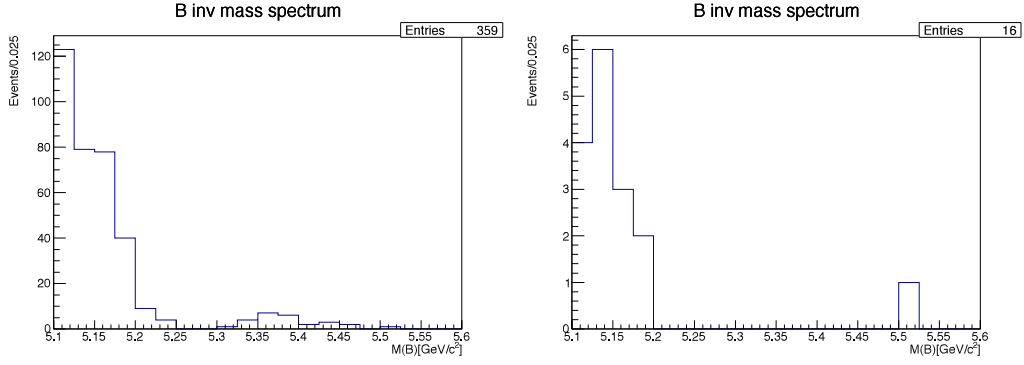
Figure 4.9: B mass distribution in $B^+ \rightarrow K^{*+}J/\psi$ sample without and with antiradition cut(left to right)
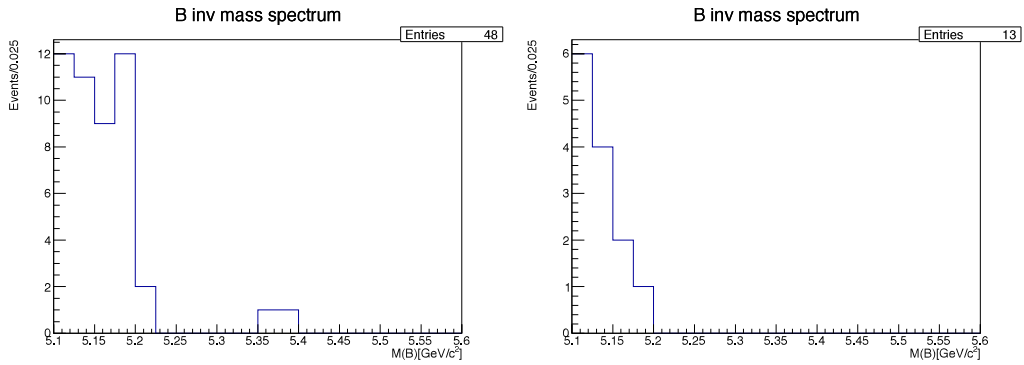
Figure 4.10: B mass distribution in $B^+ \rightarrow K^{*+}\psi'$ sample without and with antiradition cut(left to right)

background events are rejected.

4.3.2   Optimization Procedure for the Selection Cuts

The optimization procedure is data-driven, based on the maximization of the S/ $\sqrt{(S+B)}$,i.e,

Figure Of Merit(FOM). **S** is the number of truth-matched events computed on signal sim-

ulation whose B^+ invariant mass falls within $\pm 2.5\sigma_{mB^+}$ around the B^+ PDG mass (where

σ_{mB^+} is determined from signal simulation from a single Gaussian fit with unique mean

0.0315 GeV/c^2).

B is the number of events computed on data, using the dataset `Run2012A,B,C,D-22Jan2013-v1`,

whose B^+ invariant mass falls within the ranges $[(m_{B^+PDG} - 5.5\sigma_{m(B^+)}), (m_{B^+PDG} - 3\sigma_{m(B^+)})]$ GeV/c^2

or $[(m_{B^+PDG} + 3\sigma_{m(B^+)}), (m_{B^+PDG} + 5.5\sigma_{m(B^+)})]$ GeV/c^2.

The number of events computed with the simulation (**S**) is rescaled by the ratio between

data and simulation integrated luminosities (the latter is corrected by a factor that takes

into account that `PYTHIA` overestimates the B^+ production cross-section [51]).

The selection cuts scanned for the optimization are:

- CL(B^+−vtx): B^+ vertex confidence level;

- L$_{xy}$(B^+−vtx)/σ: L$_{xy}$(B^+−vtx) is the transverse separation between the B^+ vertex
  and the beamspot and σ is its uncertainty;

- cos($\alpha_{xy}^{B^+}$): $\alpha_{xy}^{B^+}$ is the angle in the transverse plane between the B^+ momentum and
 the separation between the B^+ vertex and the beamspot;

- p_T^h: hadron transverse momentum;

- DCA$_{xy}^h$/σ: DCA$_{xy}^h$ is the Distance of Closest Approach between the hadron mo-
  mentum and the beamspot in the transverse plane and σ is its uncertainty;

- K$_s p_T$ is the transverse momentum of K$_s$(coming from K^{*+}).

75

One thing to note is that for the selection cut optimization, K^{*+} mass hasn't been optimised, rather we have used ± 100 MeV/c^2(which is two times its full width) around its PDG mass value.

The scanning procedure for each selection cut under optimization is divided into following two steps:

1. **Step-1 (Individual Optimization):** In this step, each selection cut variable is scanned individually and the FOM value is computed corresponding to the scanned cut value. The optimization process is continued until the scan is completed and the maximum value is picked up.

2. **Step-2 (N-1 Optimization):** In this step, one follows the same procedure as mentioned in step-1, but during optimization, one applies the optimised values for other selection variables got from step-1, but no cut on the scanning variable itself. The process is continued for all scanned values and maximal value is noted.

All the FOM plots after step-2 for the selection cut variables are shown in Figure 4.12.

4.4   Analysis Strategy

The main goal of this analysis is to measure the forward-backward asymmetry of the muons, A_{FB}, the fraction of longitudinal polarization of the K^{*+}, F_L of the decay $B^+ \rightarrow K^{*+}\mu^+\mu^-$ as a functions of the dimuon invariant mass squared (q^2). The q^2 bins are defined in Table 4.2, they are chosen in order to match measurements performed by previous experiments.

4.4.1   Physics Model

The forward-backward asymmetry, A_{FB}, and the fraction of longitudinal polarization, F_L, are extracted from the fit to the angular observables of the decay. In Figure 4.13 are
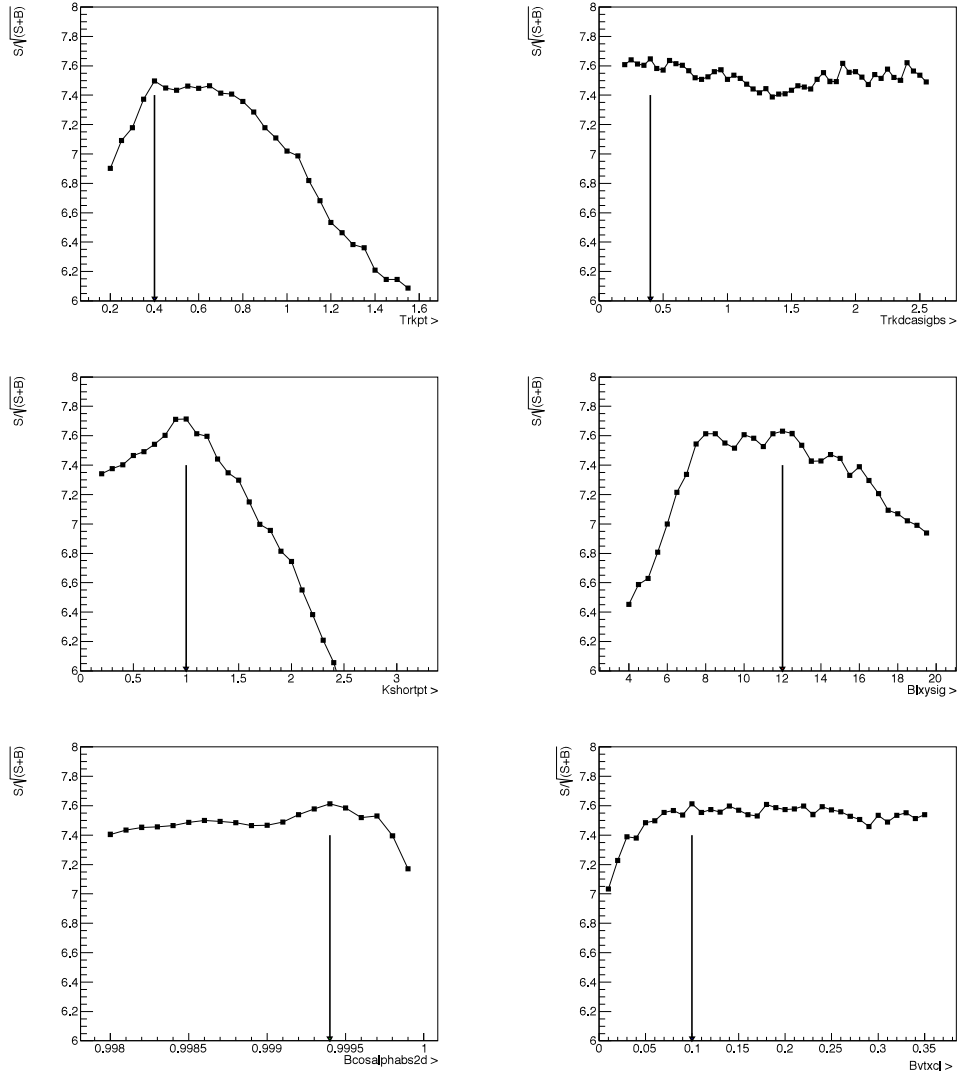
Figure 4.11: FOM plots for the selection cut variables p_T^h, $\mathrm{DCA}_{xy}^h/\sigma$, $\mathrm{K}_s p_T$, $\mathrm{L}_{xy}(B^+-\mathrm{vtx})/\sigma$, $\cos(\alpha_{xy}^{B^+}$ and $\mathrm{CL}(B^+-\mathrm{vtx}))$ are shown respectively from left to right. The arrow indicates the optimized value for that selection cut variable in the plot.

q^2 bin index	mass range $(\mathrm{GeV/c^2})^2$
0	$1-8.68$
1	$8.68-10.09$ (J/ψ region)
2	$10.09-12.86$
3	$12.86-14.18$ (ψ' region)
4	$14.18-19$
5	$1-6$
6	$1-8.68, 10.09-12.86, 14.18-19$

Table 4.2: Dimuon invariant mass bins. Both J/ψ and ψ' regions, namely q^2 bins #1 and #3, are used as control channels.
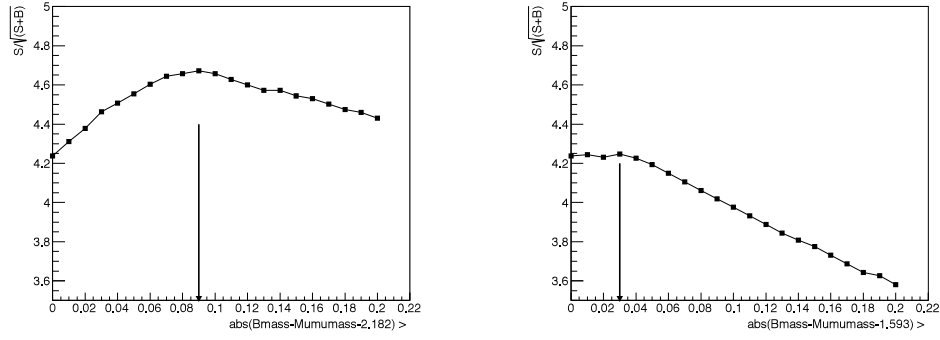
Figure 4.12: FOM plots for anti-radiation cuts: left plot for J/ψ and right plot for ψ'.

defined the angular observables for the signal and control channels, and Eqs. 4.1, 4.2, and 4.3 describe the dependence of the decay-rate as a function of such variables [52]. The angle θ_K is defined as the angle between the kaon and the opposite direction of the B^+ (B^-) in the K^{*+} (K^{*-}) reference frame, while the angle θ_l is defined as the angle between the positive (negative) charged muon and the opposite direction of the B^+ (B^-) in the dimuon reference frame. The angle ϕ is defined as the angle between the plane containing two muons and the plane containing K_s and pion. In this analysis, the angle ϕ has been integrated out due to lack of statistics.
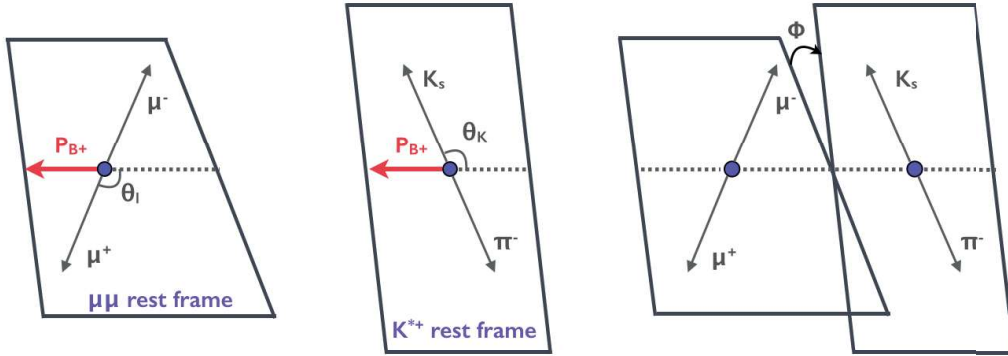
Figure 4.13: Sketch showing the definition of the angular observables for the signal ($B^+ \rightarrow K^{*+}\mu^+\mu^-$) and control channels ($B^+ \rightarrow K^{*+}J/\psi$ and $B^+ \rightarrow K^{*+}\psi'$) .

If the $K_s - \pi$ are generated from the vector meson K^{*+}, their angular distribution in the

78

final state can be described with a P-wave, while if the $K_s - \pi$ are not generated from any resonance, their angular distribution in the final state can be described with an S-wave. Therefore the processes $B^+ \to K^{*+}\mu^+\mu^-$ and $B^+ \to \pi^+\pi^-\pi^+\mu^+\mu^-$ have different angular distributions and to perform the measurements that are the object of this analysis, it is in principle important to disentangle P-wave from S-wave decays. Indeed the decay rates described in Eqs. 4.1, 4.2, and 4.3 take into account both processes as well as their interference, where the fraction of S-wave is described by the F_S term (the fraction of P-wave is simply $F_P = 1 - F_S$), while the interference between S and P-waves is described by the A_S term.

$$\frac{1}{\Gamma}\frac{\mathrm{d}^2\Gamma}{\mathrm{d}\cos\theta_l\mathrm{d}q^2} = \frac{1}{8}\left(3(1 + F_L + F_S - F_L F_S)\right.$$
$$+8A_{FB}(1 - F_S)\cos(\theta_l) \tag{4.1}$$
$$\left.+3(1 - 3F_L(1 - F_S) - 3F_S)\cos^2(\theta_l)\right),$$

$$\frac{1}{\Gamma}\frac{\mathrm{d}^2\Gamma}{\mathrm{d}\cos\theta_K\mathrm{d}q^2} = \frac{1}{4}\left(2F_S\right.$$
$$+4A_S\cos(\theta_K) \tag{4.2}$$
$$\left.+3(1 - F_S)(1 - F_L - \cos^2(\theta_K) + 3F_L\cos^2(\theta_K))\right),$$

$$\frac{1}{\Gamma}\frac{\mathrm{d}^3\Gamma}{\mathrm{d}\cos\theta_K\mathrm{d}\cos\theta_l\mathrm{d}q^2} = \frac{9}{16}\left(\left(\frac{2}{3}F_S + \frac{4}{3}A_S\cos(\theta_K)\right)(1 - \cos^2(\theta_l))\right.$$
$$+(1 - F_S)[2F_L\cos^2(\theta_K)(1 - \cos^2(\theta_l))$$
$$+\frac{1}{2}(1 - F_L)(1 - \cos^2(\theta_K))(1 + \cos^2(\theta_l)) \tag{4.3}$$
$$\left.+\frac{4}{3}A_{FB}(1 - \cos^2(\theta_K))\cos(\theta_l)]\right).$$

4.4.2 The Probability Density Function

The interesting observables are extracted from unbinned fits using an extended maximum likelihood estimator. The p.d.f. has the following mathematical expression:

$$\text{p.d.f.}(m, \theta_K, \theta_l) = Y_{Si}\ S_i^M(m) \cdot S_i^A(\theta_K, \theta_l) \cdot \mathcal{E}_i(\theta_K, \theta_l)$$
$$+ Y_{Bi}^c\ B_i^{Mc}(m) \cdot B_i^{\theta_K c}(\theta_K) \cdot B_i^{\theta_l c}(\theta_l) \tag{4.4}$$
$$+ Y_{Bi}^p\ B_i^{Mp}(m) \cdot B_i^{\theta_K p}(\theta_K) \cdot B_i^{\theta_l p}(\theta_l),$$

where

- Y_{Si}, Y_{Bi}^c, and Y_{Bi}^p are the yields of the "signal", "combinatorial" and "peaking" backgrounds respectively; the "combinatorial" component accounts for the background coming from the unavoidable fraction of misreconstructed B^+ from randomly associated dimuons to hadrons, while the "peaking" component accounts for the feed-through from the control channels;

- $S_i^M(m) \cdot S_i^A(\theta_K, \theta_l)$ describes the signal shape in the 3D-space: B^+ invariant mass and angular observables;

- $B_i^{Mc}(m) \cdot B_i^{\theta_K c}(\theta_K) \cdot B_i^{\theta_l c}(\theta_l)$ describes the "combinatorial" background shape in the 3D-space: B^+ invariant mass and angular observables;

- $B_i^{Mp}(m) \cdot B_i^{\theta_K p}(\theta_K) \cdot B_i^{\theta_l p}(\theta_l)$ describes the "peaking" background shape in the 3D-space: B^+ invariant mass and angular observables;

- $\mathcal{E}_i(\theta_K, \theta_l)$ describes the efficiency in the 2D-space of the angular observables (more details on the efficiency are given in Sec. 4.7);

where the subscript i runs over q^2 bins listed in Table 4.2. Unless explicitly stated in the text, every time when it is referred to $\theta_{K/l}$ it is actually meant $\cos(\theta_{K/l})$.

The mathematical expressions of the various terms of the p.d.f. are:

q^2 bin index	$B_i^{Mc}(m)$	$B_i^{Mp}(m)$	$B_i^{\theta_K p}(\theta_K)$	$B_i^{\theta_l p}(\theta_l)$	$B_i^{\theta_K c}(\theta_K)$	$B_i^{\theta_l c}(\theta_l)$
0	exp fun	1 exp.	4th degree	4th degree	4th degree	2 gauss
2	exp fun	1 Gauss	4th degree	4th degree	4th degree	4th degree
4	exp fun	1 Gauss	4th degree	4th degree	4th degree	4th degree
5	exp fun	N.A	N.A	N.A	5th degree	2 guass
6	exp fun	exp/gauss	4th degree	4th degree	4th degree	2 gauss

Table 4.3: Mathematical description of the background parameterizations for data (both for "combinatorial" and "peaking") as a function of q^2 bins.

- $S_i^M(m)$: double Gaussian with unique mean;

- $S_i^A(\theta_K, \theta_l)$: right-hand side term of Eq. 4.3;

- $B_i^{Mc}(m)$: exponential function;

- $B_i^{Mp}(m)$: zero, one Gaussian or exponential function depending on q^2 bin (see Table 4.3) to model the mass shape of the "peaking" background from the tails of the J/ψ and ψ' modes.

- $B_i^{\theta_{K/l}c}(\theta_{K/l})$: fourth or fifth degree polynomial or 1-2 Gaussians depending on q^2 (see Table 4.3);

- $B_i^{\theta_{K/l}p}(\theta_{K/l})$: fourth degree polynomial (see Table 4.3);

- $\mathcal{E}_i(\theta_K, \theta_l)$: 6th order polynomial or 3 gaussians multiplied by 0-3rd order Legendre Polynomial as a function of θ_K and θ_l respectively (see Table 4.5.

4.4.3 Fit Sequence

The fit is performed in stages during which some components of the p.d.f. are determined from simulation, namely:

- "signal" shape $S_i^M(m)$ (only the two sigma and the Gaussian fraction);

- "peaking" background shapes and yield $Y_{Bi}^p \cdot B_i^{\theta_K p}(\theta_K) \cdot B_i^{\theta_l p}(\theta_l)$.

while the remaining ones are determined directly from data. At each stage a component of the p.d.f. is fitted and determined for the next stage. In the next stage, the previously determined component is constrained with Gaussian constraints.

The fit-stages are:

1. Determination of the shape as a function of the B^+ invariant mass variable:

    (a) Extract the signal shape from fit to signal simulation in the whole signal mass region $[m_{B^+ \text{PDG}} \pm 0.28]$ GeV/c^2 (see fit results in Figure 4.38);

    - p.d.f. $= Y_{Si} \cdot S_i^M(m) + Y_{Bi}^c \, B_i^{Mc}(m)$;

    - determination: $S_i^M(m)$.

    (b) Extract the "peaking" background shape and yield from fit to the control channel simulations in the whole signal mass region $[m_{B^+ \text{PDG}} \pm 0.28]$ GeV/c^2 (see fit results in Figure 4.39-4.41 and 4.40-4.42);

    - p.d.f. $= Y_{Bi}^p \cdot B_i^{Mp}(m)$;

    - determination: Y_{Bi}^p and $B_i^{Mp}(m)$ (Y_{Bi}^p is rescaled by the yield ratio between data and simulation of the control channel $B^+ \to K^{*+} J/\psi$, or $B^+ \to K^{*+} \psi'$ depending on the q^2 bin, and the errors are assigned accordingly).

2. Determination of the shape as a function of the angular variables (θ_K and θ_l):

    (a) Extract the "peaking" background shape as a function of the angular variables from fit to the control channel simulations (see fit results in Figure 4.39-4.41 and 4.40-4.42);

    - p.d.f. $= Y_{Bi}^p \cdot B_i^{\theta_K p}(\theta_K) \cdot B_i^{\theta_l p}(\theta_l)$;

    - Gaussian constraints for Y_{Bi}^p and $B_i^{Mp}(m)$;

    - determination: $B_i^{\theta_K p}(\theta_K)$ and $B_i^{\theta_l p}(\theta_l)$.

    (b) Extract the "combinatorial" background shape as a function of the angular variables from fit to the data sidebands (see fit results in Figure 4.43 and 4.44);

- p.d.f. $= Y^c_{Bi} \cdot B^{\theta_K c}_i(\theta_K) \cdot B^{\theta_l c}_i(\theta_l)$;

- determination: $B^{\theta_K c}_i(\theta_K)$ and $B^{\theta_l c}_i(\theta_l)$.

In order to guide the 3D-fit, a prior 2D-fit is performed as a function of the angular variables to the B^+ sidebands to get the initial values of the combinatorial background. The B^+ sidebands are defined as $[m_{B^+\text{PDG}} - 0.28, m_{B^+\text{PDG}} - 2.5\sigma_{mB^+}]$ GeV/c^2 and $[m_{B^+\text{PDG}} + 2.5\sigma_{mB^+}, m_{B^+\text{PDG}} + 0.28]$ GeV/c^2, where σ_{mB^+} is defined in Sec. 4.3.2. During the final 3D-fit, A_S, A_{FB}, F_S and F_L are all left floating.

4.4.4 Convergence verification and fitting quality control

Due to limited statistics, we want to minimize the number of floating parameters. During the final fitting step, the free, fixed and constrained parameters are:

- the physical obseravbles F_L and A_{FB} are free parameters to be obtained from fit ;

- the signal mass shape parameters are fixed ;

- the background angular shape parameters are fixed ;

- the peaking background mass shape parameters and number of events are fixed ;

- the combinatorial background mass shape parameters and number of events are free to float.

To ensure good fitting, we have verified all the fits. The qualities checked are the status of convergence, the positive definiteness of the covariance matrix, the goodness of the shapes of likelihood profile, and the agreement of the errors estimated from profile likelihood with that of the fitting output. This implies that all the plots of this analysis showing fit results should show the tag: Fit Status: **GOOD**.

$\cos(\theta_K)$	$\cos(\theta_l)$	p.d.f.
-1	-1	0
-1	0	$F_S - A_S + 3F_L(1-F_S) \geq 0$
-1	+1	0
0	-1	$(1-F_S)(1-F_L-\frac{4}{3}A_{FB}) \geq 0$
0	0	$4F_S + 3(1-F_L)(1-F_S) \geq 0$
0	+1	$(1-F_S)(1-F_L+\frac{4}{3}A_{FB}) \geq 0$
+1	-1	0
+1	0	$F_S + A_S + 3F_L(1-F_S) \geq 0$
+1	+1	0

Table 4.4: Search for the physically-allowed domain of the angular variables. The p.d.f. in Eq. 4.4 is imposed to be positive for specific values of the angular observables.

4.4.5 Angular Variables Transformations and Uncertainty Determination

In order to make the decay rate described in Eq. 4.3 to be positive, the p.d.f mentioned in Eq. 4.4 should be constrained to physically allowed domains to make it positive. This requirement of physical validness should be fulfilled over the whole angular observables domain. Hence, the values of the angular variables should lie within those specific ranges. The physically allowed ranges are determined by requiring the p.d.f to be positive within the bound values determined from the particular values of the angular observables which is summarised in Table 4.4.

The approximate ranges of validity are therefore:

- F_L: range of validity [0,1];

- A_{FB}: range of validity $[-\frac{3}{4}(1-F_L), +\frac{3}{4}(1-F_L)]$;

- F_S: range of validity $[0, \min\left\{\frac{3(1-F_L)}{1+3F_L}, 1\right\}]$;

- A_S: range of validity $[-(F_S+3F_L(1-F_S)), +(F_S+3F_L(1-F_S))]$;

In order to apply this constraints in the fittings, the non-linear transformations of the angular variables are performed. The transformation allows MINUIT [53] to use the unbounded

84

variables internally, which are labeled here with an "⌢". After these transformations, the physical variables,i.e, the "un-hat" variables are guaranted to lie within the physically-allowed domain. So, there is no need to implement specific "penalty" terms which is in general very unnatural.

The angular variables and their transformations are:

- $F_L = 1/2 + \arctan(\widehat{F_L})/\pi$;

- $A_{FB} = 3/4(1 - F_L) \cdot 2\arctan(\widehat{A}_{FB})/\pi$;

- F_S is not transformed but simply limited within the range [0,1];

- A_S is not transformed but simply limited within the range [-1,1].

Because it is easier for MINUIT to deal with unbounded variables and with continuous p.d.f.s, the non-linear transformations are extremely powerful to find the global maximum likelihood. On the other hand the error computation is not trivial when in presence of these non-linear transformations and it might result in incorrect estimation of the fitting uncertainties. For this reason the errors on F_L and A_{FB} are computed by re-fitting the data without the non-linear transformations and by initializing the fit with values determined previously (*i.e.* with the non-linear transformation).

In summary, all steps described in Sec. 4.4.3 are performed with a p.d.f. implementing the non-linear transformations, leading to the determination of the central value of the variables. In order to determine the uncertainties on the angular observables, namely F_L and A_{FB}, the fit is run one more time without the non-linear transformations, using MINOS [53], and with starting values determined as in Sec. 4.4.3.

The whole fit procedure is thoroughly validated as described in Sec. 4.8.

4.5 Studies of Possible Background Peaking in the Signal Region

There might be B^+ decays whose final state dynamics and kinematics is similar to the one of the signal or control channels, which are object of this analysis. It is of particular danger for this analysis if a background would result in a peak centered right at the B^+ mass. The possible presence of such a background is studied with one kind of simulation listed below. Only B^+ decays are considered here for completeness. Figure 4.14 shows the mother particle invariant mass plots in three different conditions:

- rejecting the J/ψ and ψ' regions;

- selecting only the J/ψ region;

- selecting only the ψ' region.

For the above simulation sample $B^+ \to \psi(\mu^+\mu^-)X$, in the first plot there is **no evidence for a peak centered at the B^+ mass**, therefore they won't be further discussed since the resulting background is taken into account with the "combinatorial" background component of the p.d.f. (see Sec. 4.4).

By writing "ψ" in the final state it is actually meant all known ψ states, *e.g.* J/ψ, ψ', etc... The rescale of the luminosities to data must take into account the production cross-section difference between PYTHIA and data as reported in the referenced publications. All samples are officially produced with the following characteristics: 2MuPtEtaFilter_8TeV-pythia6-evtgen and Summer12_DR53X-PU_S10_ START53_V7A-v1.
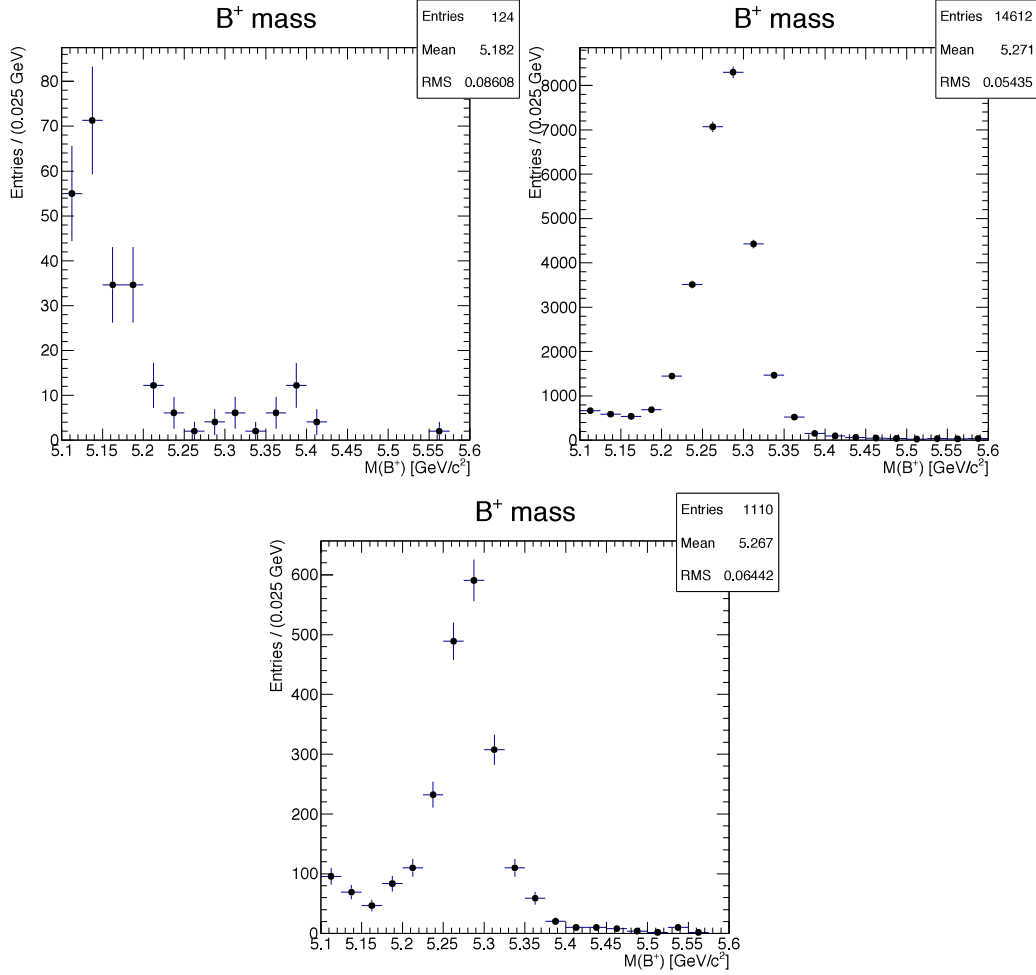
Figure 4.14: B^+ invariant mass plots from the simulation sample $B^+ \to \psi(\mu^+\mu^-)X$. The number of entries is rescaled in order to match the amount of data recorded. The first plot is made by rejecting the J/ψ and ψ' regions (see Sec. 4.3 for the rejection criteria). The second plot is made by selecting only the J/ψ region. The third plot is made by selecting only the ψ' region. The numbering goes from left to right and from top to bottom.

4.6 Data-Simulation Comparison of various kinematic and dynamic variables

The main kinematic observables, such as p_T, and ϕ for B^+ and the selection variables, are compared between data and simulation. On data only the J/ψ dimuon mass regions have been selected by applying the selection criteria described in Sec. 4.3. All plots from data are background subtracted (the plot of the sidebands is subtracted from the plot of the signal region, for the definition of signal and sideband regions, see Sec. 4.3.2).

The compared kinematic and dynamic observables shown on the Figure 4.15 are:

- B p_T: B^+ transverse momentum ;

- B vtx. CL: B^+ vertex confidence level ;

- B ϕ: azimuthal angle of B^+ ;

- DCA$_{xy}^{B^+}/\sigma$: B^+ vertex L_{xy}/σ ;

- cos$\alpha_{xy}^{B^+}$: B^+ cosα_{xy} ;

- K$_s p_T$: transverse momentum of K_s.

4.7 Efficiency Modelling

The efficiency for reconstructing signal events is entirely computed from MC simulation. The general definition of the efficiency is the ratio between the number of reconstructed events that pass the selections over the total number of generated events.

The actual computation splits the efficiency into two terms as in Eq. 4.5:

$$\varepsilon_{total} = \varepsilon_{acceptance} \cdot \varepsilon_{reconstruction},\qquad(4.5)$$

where
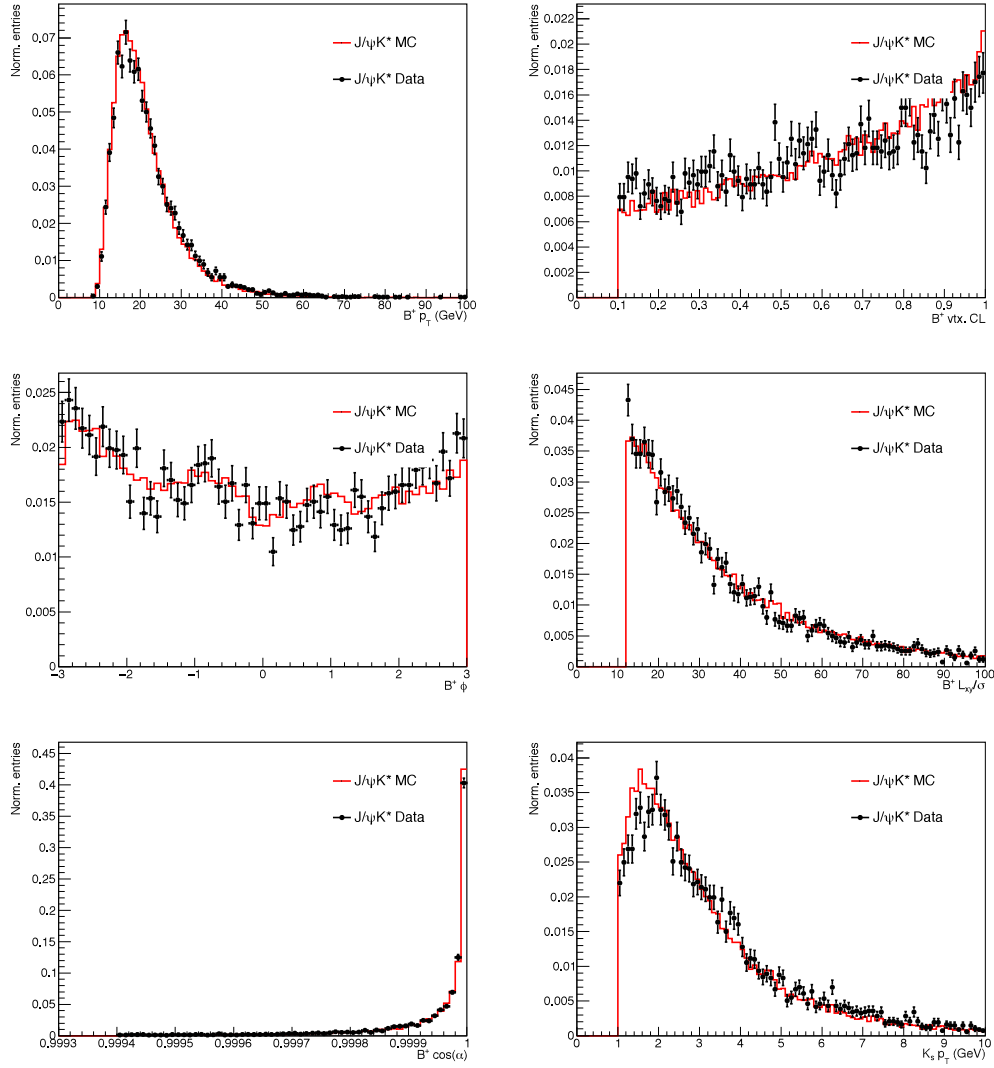
Figure 4.15: Variable comparison between data and simulation of the B^+. Both data and simulation have been rescaled in order to have unit area. In data only the J/ψ dimuon mass regions have been selected. The simulation, instead, is J/ψ control sample.

- $\mathcal{E}_{acceptance}$ is the "acceptance" efficiency defined as the ratio between the number of events that pass the single muon selections ($p_T^\mu > 2.8$ GeV and $|\eta^\mu| < 2.3$, this selection is performed at the GEN level of the simulation) over the total number of events generated.

- $\mathcal{E}_{reconstruction}$ is the "reconstruction" efficiency defined as the ratio between the number of reconstructed events that pass the selections and are truth-matched over the number of events that pass the single muon selections ($p_T^\mu > 2.8$ GeV and $|\eta^\mu| < 2.3$, this selection is performed at the GEN level of the simulation); $\mathcal{E}_{reconstruction}$ is computed by means of the RECO MC simulation which also contains the GEN information, the RECO information is used to compute the numerator, while the GEN one is used to compute the denominator.

- $\mathcal{E}_{total}$ is the total efficiency which is product of $\mathcal{E}_{acceptance}$ and $\mathcal{E}_{reconstruction}$.

The total efficiency value is found to be about 0.8×10^{-4} for this analysis.

4.7.1 Acceptance Efficiency

Since the official signal MC sample doesn't save the GEN level information before filter, we have to generate a private unfiltered signal MC. The total number of events is 35,080,733. For acceptance efficiency calculation, the denominator is number of events generated, while the numerator is the number of events in acceptance region (that pass single muon selections).

4.7.2 Reconstruction Efficiency

The reconstruction efficiency is calculated from the official MC sample where the denominator is the number of events in acceptance region (that pass singlemuon selections) and the numerator is number of events passed all selection cuts mentioned before.

q^2 bin	$\cos\theta_K$	$\cos\theta_L$	cross terms
0	pol6	3 gauss	3rd LP * pol4
2	pol6	pol6	3rd LP * pol4
4	pol6	pol6	3rd LP * pol4
5	pol6	3 gauss	3rd LP * pol4
6	pol6	pol6	3rd LP * pol4

Table 4.5: The different shapes used for $\cos\theta_K$, $\cos\theta_L$ and cross terms in efficiency modelling where LP and poln stand for Legendre Polynomial and nth order polynomial respectively.

4.7.3   Total Efficiency and modelling

There is limited statistics from the official signal MC sample and the efficiency is quite low. Correlation is seen in the official MC smaple. Due to the low efficiency, to achieve a good PDF with under limited size of samples in one step is not easy. The following steps are adopted, and detailed functions could be found in Table 4.5

- Fit is performed to each angular axes assuming there's no correlation in between. Then, the product of the functions are taken as the base function for higher order correction.

- For the correlation term, a correction term of "1+cross terms" is considered and multiplied to the base function. An extra normalization term is also taken into account for proper normalization of efficiency map.

The fit projections into angular axes $\cos\theta_K$ and $\cos\theta_L$ are shown in Figure 4.16 and 4.17 respectively whereas the correlation plots are shown in Figure 4.18 for each q^2 bin.

4.8   Angular Analysis Validation

A detailed validation of the analysis is performed with MC simulation and confirmed on data with the control channels. All analysis steps, *i.e.*signal selection, efficiency computation, and fit procedure, are applied on signal simulation, also called RECO MC, just as they

Figure 4.16: Projection of total efficiency onto $cos\theta_K$ angular axis for q^2 bins 0,2,4,5 and 6 for signal simulation and fitting results.
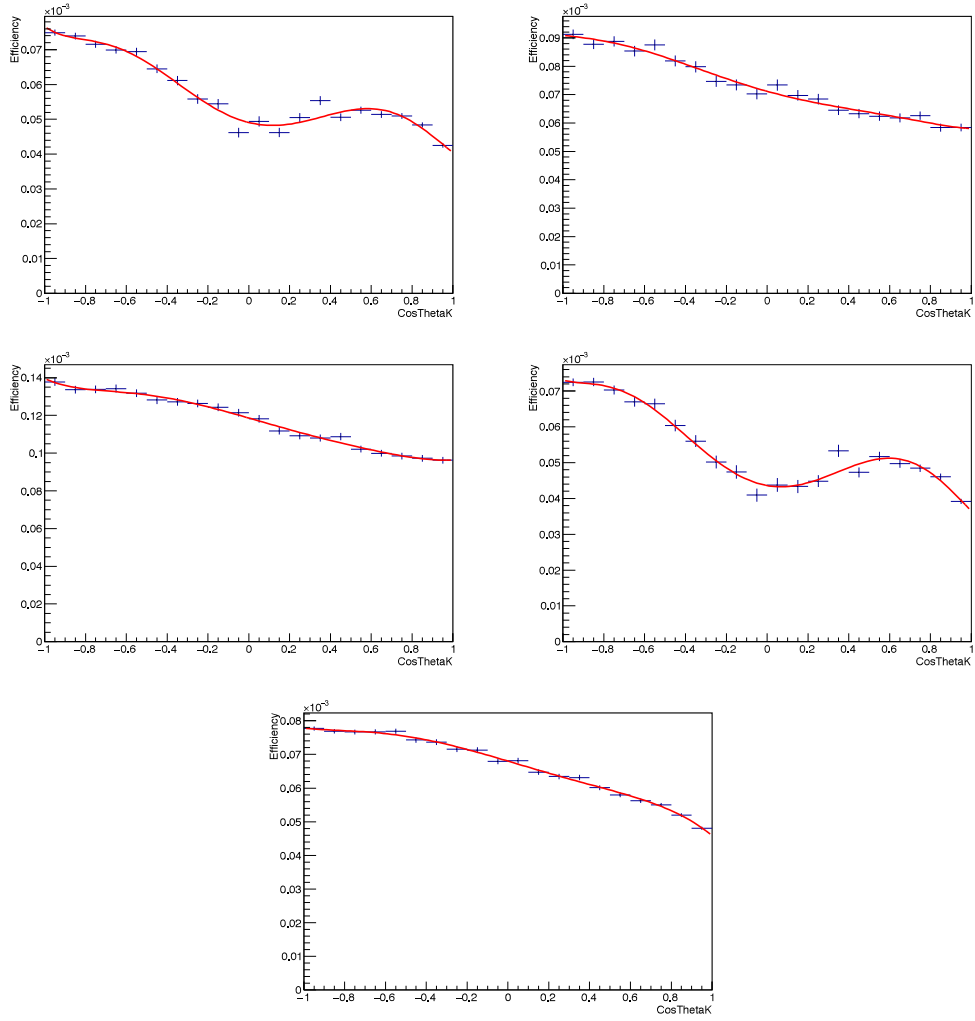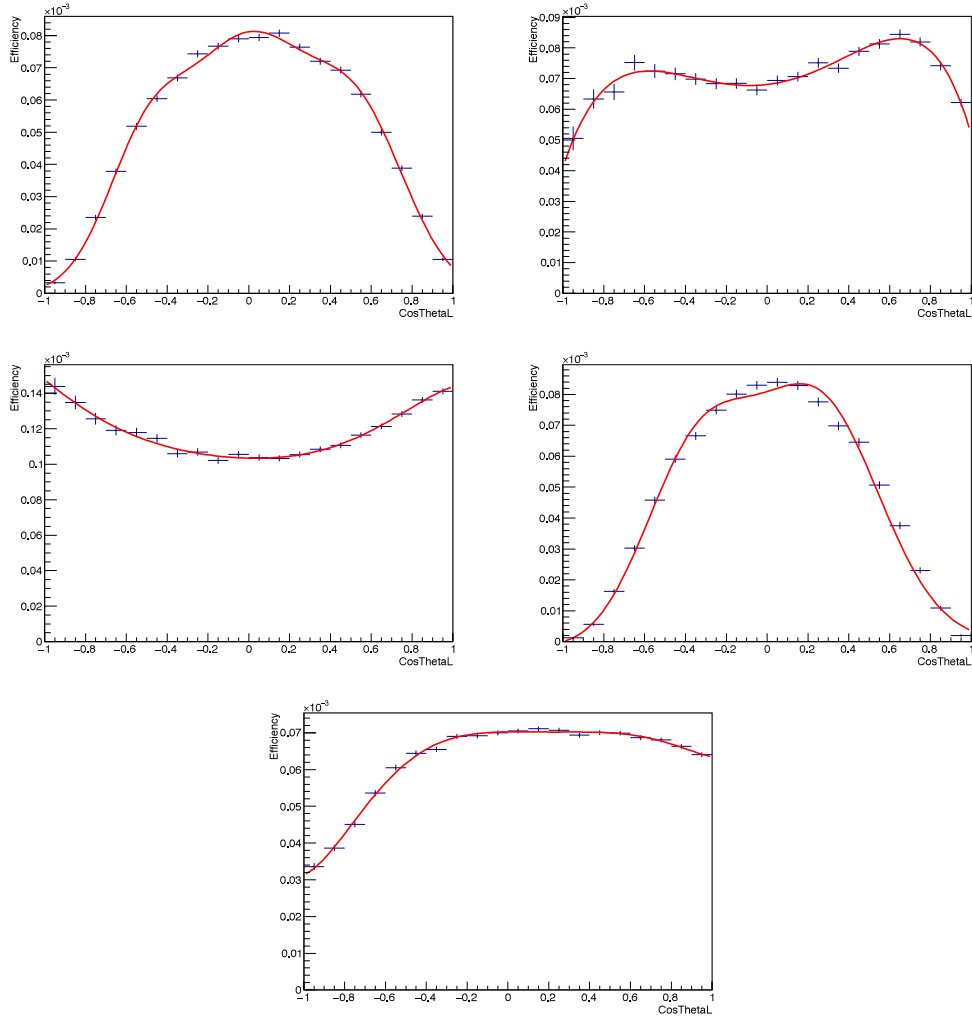
Figure 4.17: Projection of total efficiency onto $cos\theta_L$ angular axis for q^2 bins 0,2,4,5 and 6 for signal simulation and fitting results.
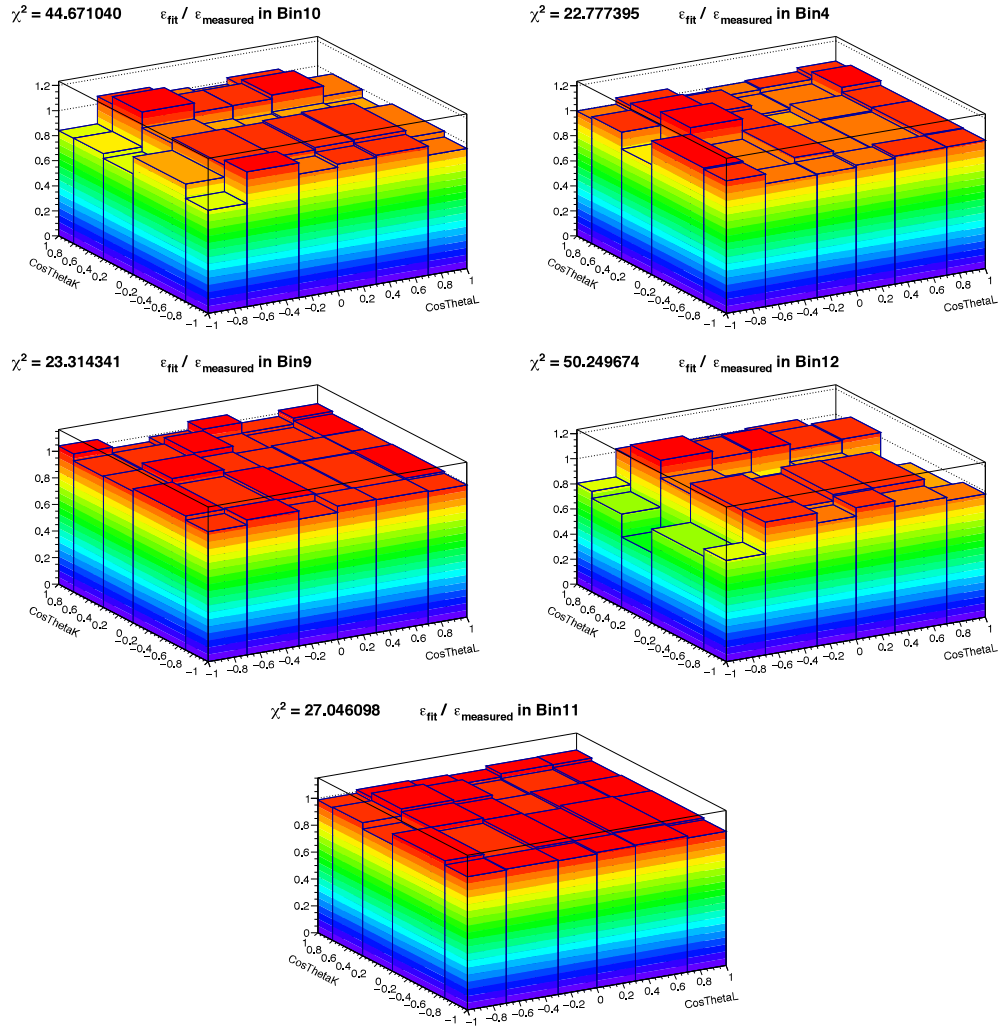
Figure 4.18: The correlation plots between the two angular axes $cos\theta_L$ and $cos\theta_K$ for q^2 bins 0,2,4,5 and 6 from signal simulation.

are applied on data. The interesting observables, namely A_{FB} and F_L, are measured as a function of the dimuon q^2 and compared to values extracted from the simulation at pure generator level (GEN MC). In particular on GEN MC, due to the absence of any selection and background, only the pure angular shape is fitted to extract A_{FB} and F_L using Eq. 4.3. The validation procedure with the MC simulation is two-fold:

- validation with High-Statistics, pure Signal Simulation without background;

- closure tests and validation of fitting program

4.8.1 Validation with High-Statistics pure Signal Simulation

The analysis is validated with the highest number of events available signal MC simulation, without background, in order to verify if asymptotically the analysis is able to measure the interesting observables, and to quantify possible biases of the measurements.

The validation of the analysis is performed with MC simulation at both GEN and RECO level. The size of the signal MC sample corresponds to ~37,378.63 fb^{-1} which is about 1900 times data size. All analysis steps, i.e, signal selection, efficiency modelling and fitting procedures are applied on official signal simulation samples(denoted as Official-MC) in exact the same manner as they are applied on data. At both the generator level(GEN level) and reconstruction level(RECO level), the observables A_{FB} and F_L are determined as a function of the dimuon invariant mass squared (q^2).

In the fit at GEN level, we use the theoretical angular shape to fit the GEN level information to extract A_{FB} and F_L. Details of the GEN level fitting results in each q^2 bin are shown in Figure 4.19.

In the fit at RECO level, the theoretical angular shape is corrected by the total efficiency to fit the RECO level information to extract A_{FB} and F_L. Detailed fitting results per q^2 bin are shown in Figure 4.20.

The results for A_{FB} and F_L extracted from simulation at both GEN and RECO level are

compared in Figure 4.21. GEN level results are in black plus sign with vertical line denoting statistical errors. RECO level results are in black points with red band denoting statistical errors respectively.

The major conclusion from this test are: the efficiency modelling is good enough and it describes data so well that the results at both GEN and RECO level agree. This is a validation of the fitting procedure and the fitting components.

4.8.2 Validation with Signal MC Sub-samples

In order to validate the fitting procedures, we have also performed studies based on signal MC samples. The basic idea is to divide the total sample into many sub-samples and perform the angular fitting with same procedure as we do for data. In principle, the reslults from these fitting should be stable and consistent results should be obtained.

Since the MC luminosity is about 1900 times data, we divided the total sample into sub-samples where each subsample has same size and luminosity same as data. And the division was completely random basis. The fitting results for only subsamples are shown in Figure 4.22 while the A_{FB} and F_L spectrum for all subsamples are shown in Figure 4.23.

From these plots, the fitting results are quite stable with different sub-samples at both GEN and RECO level.

4.8.3 Validation with Cocktail MC sample

This fitting procedure is validated with the cocktail simulation containing signal, peaking and combinatorial backgrounds. Each cocktail sample is a pure toy of signal and background fit results. The total number of events correspond to full statistics of ~4000 fb^{-1}. The whole sample is divided into 2 sub-samples where each subsample corresponds to ~2000 fb^{-1} which is ~100 times data luminosity. The goal is to verify whether in data-like conditions and with a high number of events, the analysis is able to measure the

96
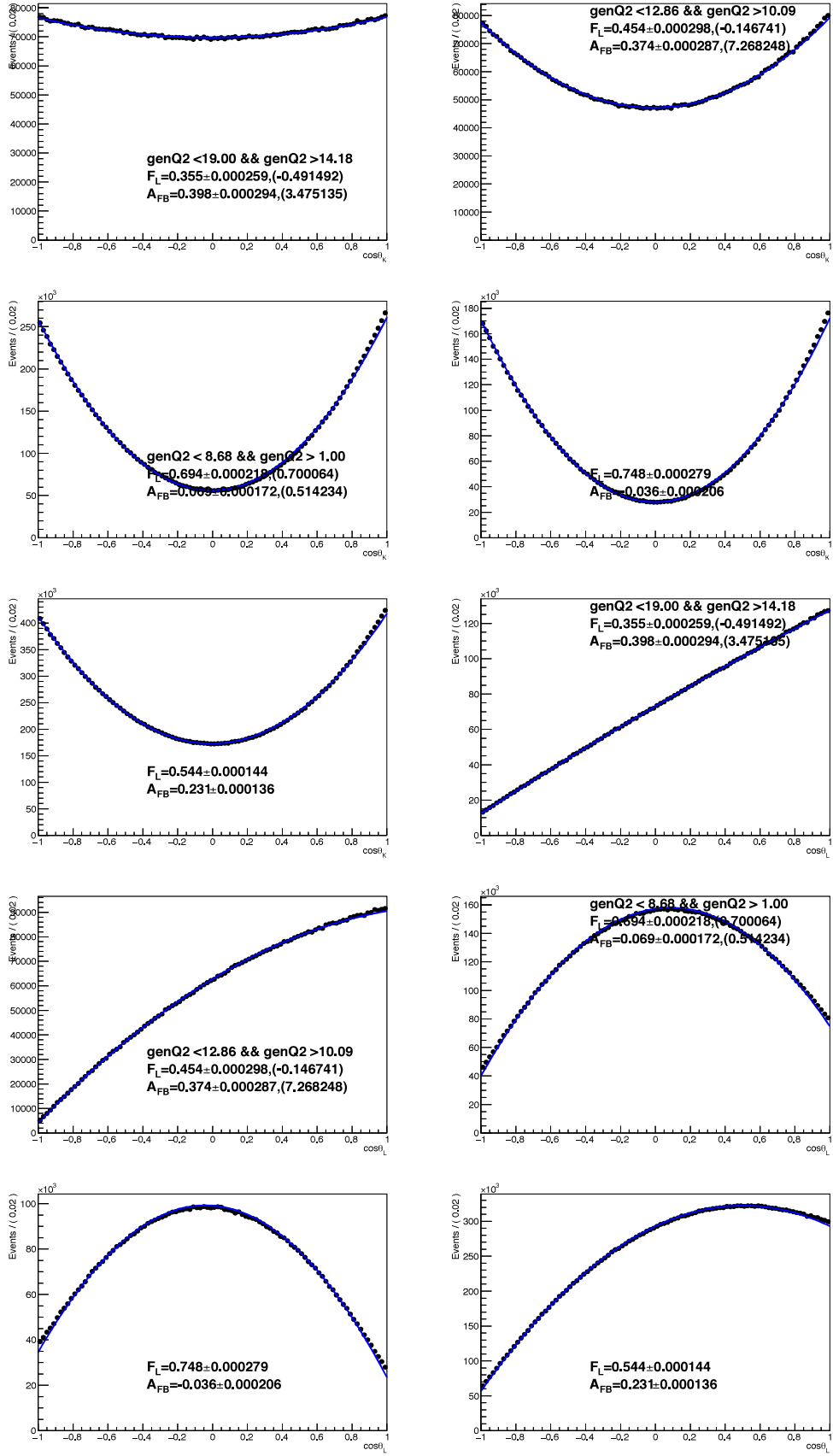
Figure 4.19: Angular fitting results at GEN level in each q^2 bin.
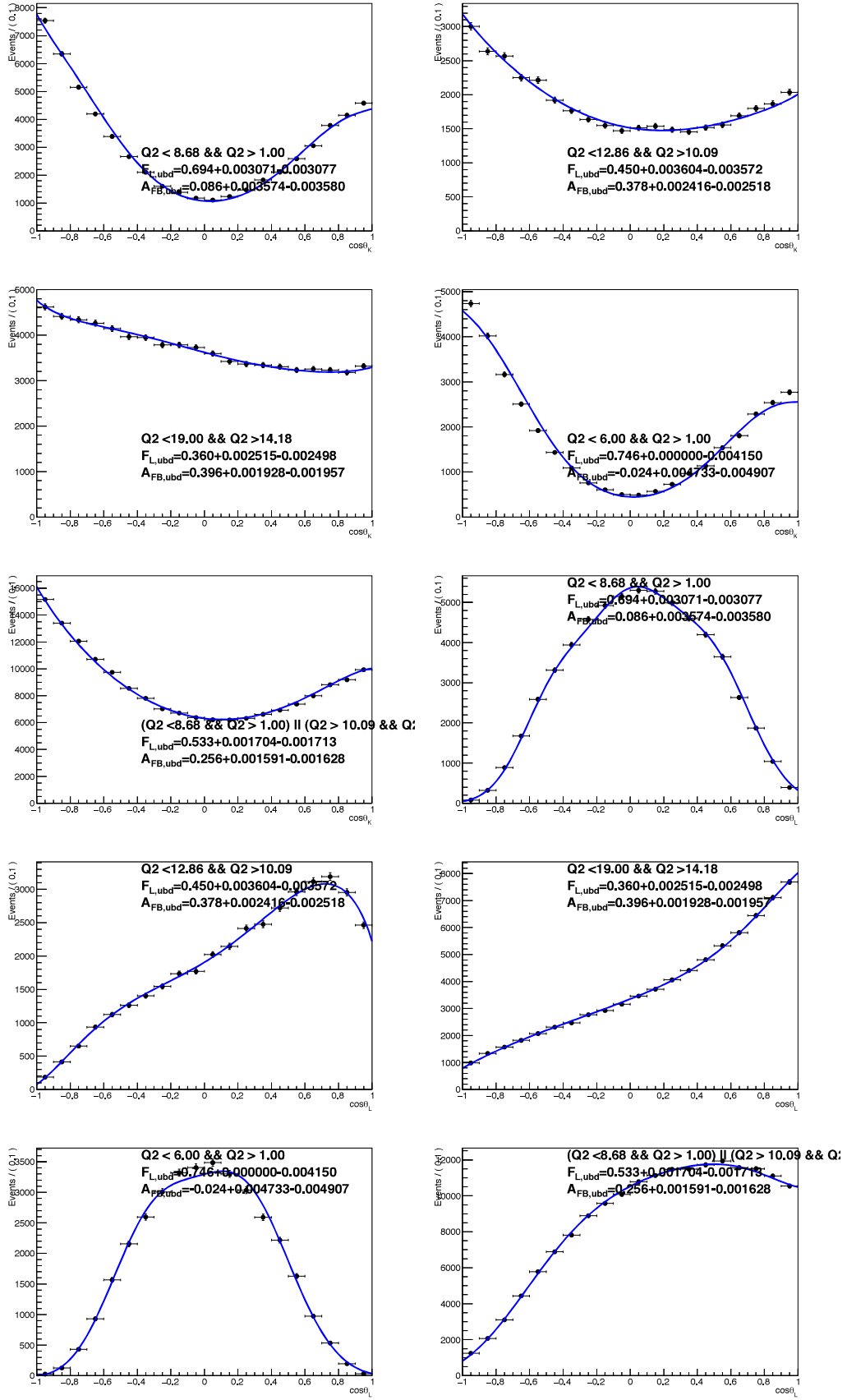
Figure 4.20: Angular fitting results at RECO level in each q^2 bin.
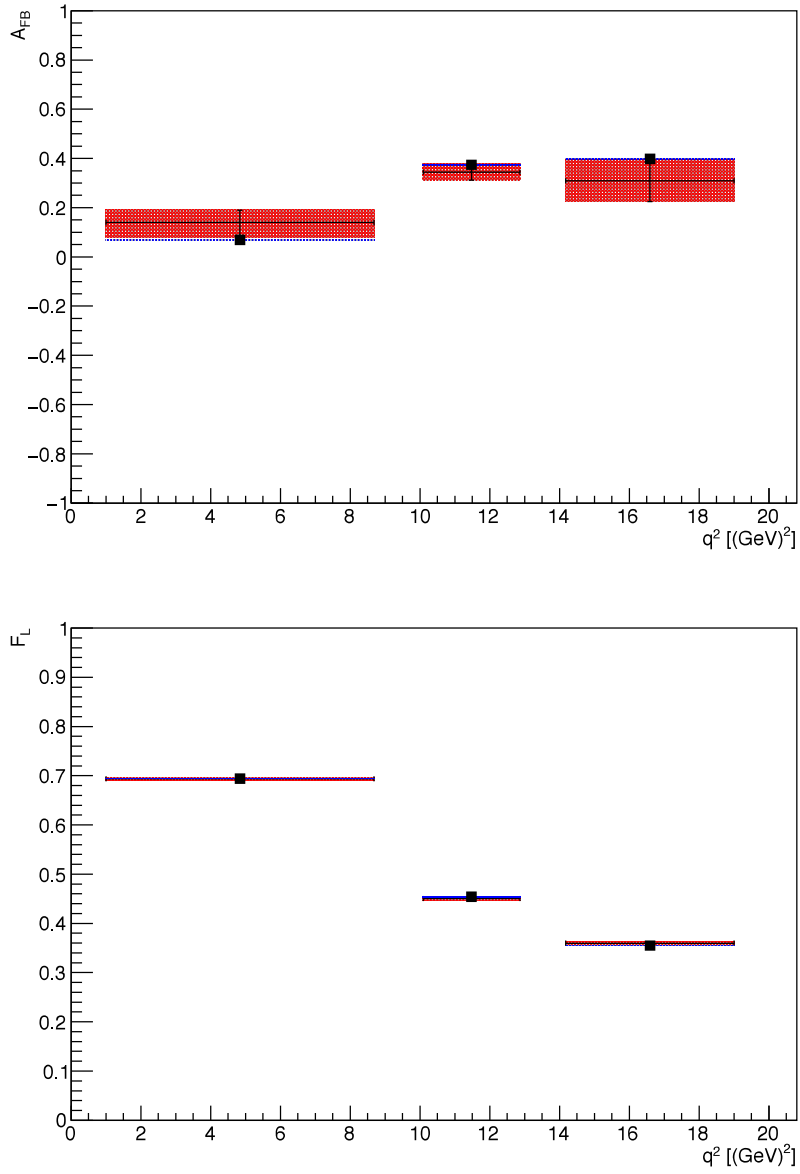
Figure 4.21: Validation of the analysis with truth-matched signal simulation: comparison between results of the GEN level(black dot and black plus) and RECO level(black dot and red band) for both observables A_{FB}(top) and F_L(bottom). The plots show values as a function of dimuon q^2. The errors shown here are purely statistical.
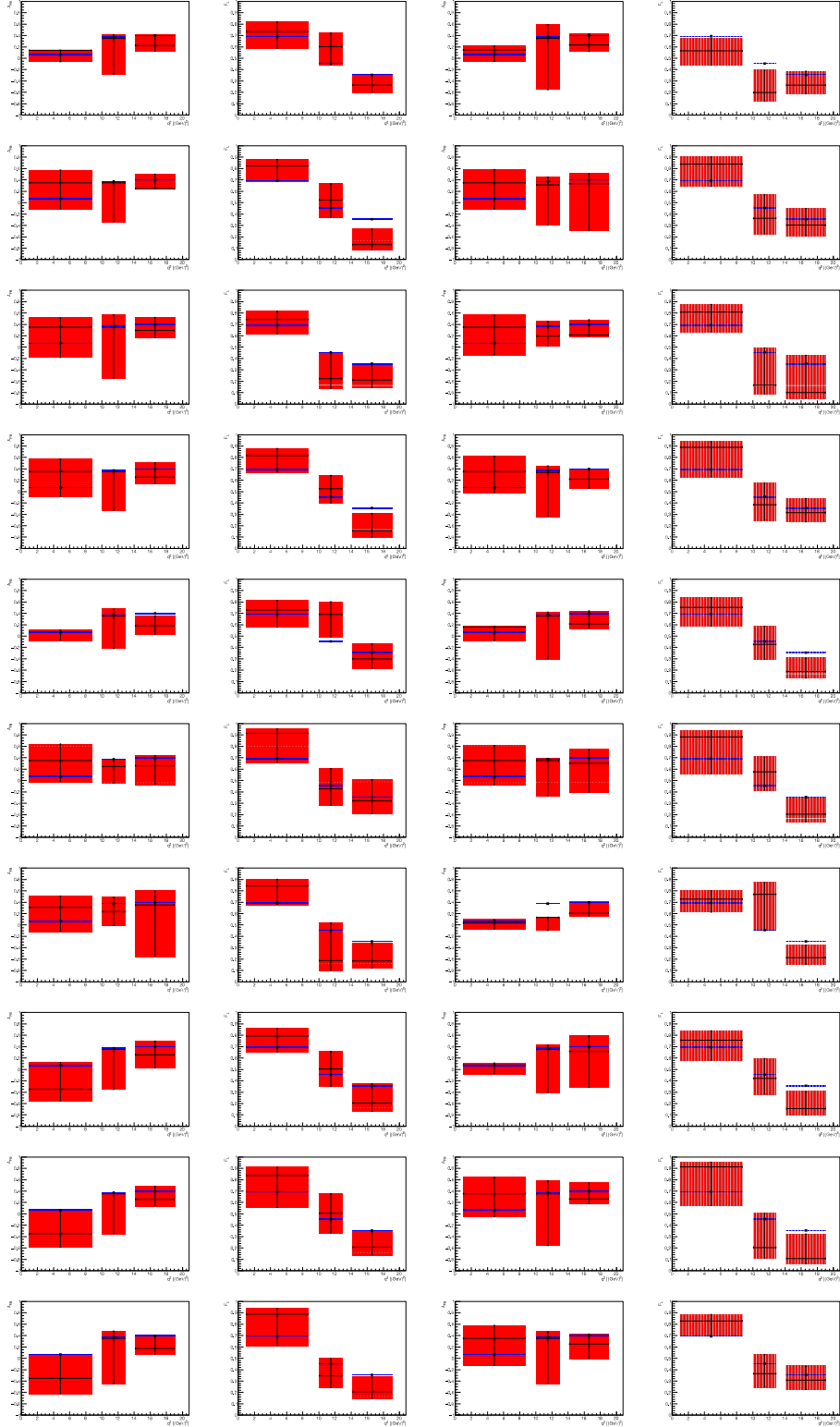
Figure 4.22: Bin-by-bin comparison of GEN(black square and black plus) and RECO(black dot and red band) level results from all q^2 bins for 20 subsamples.
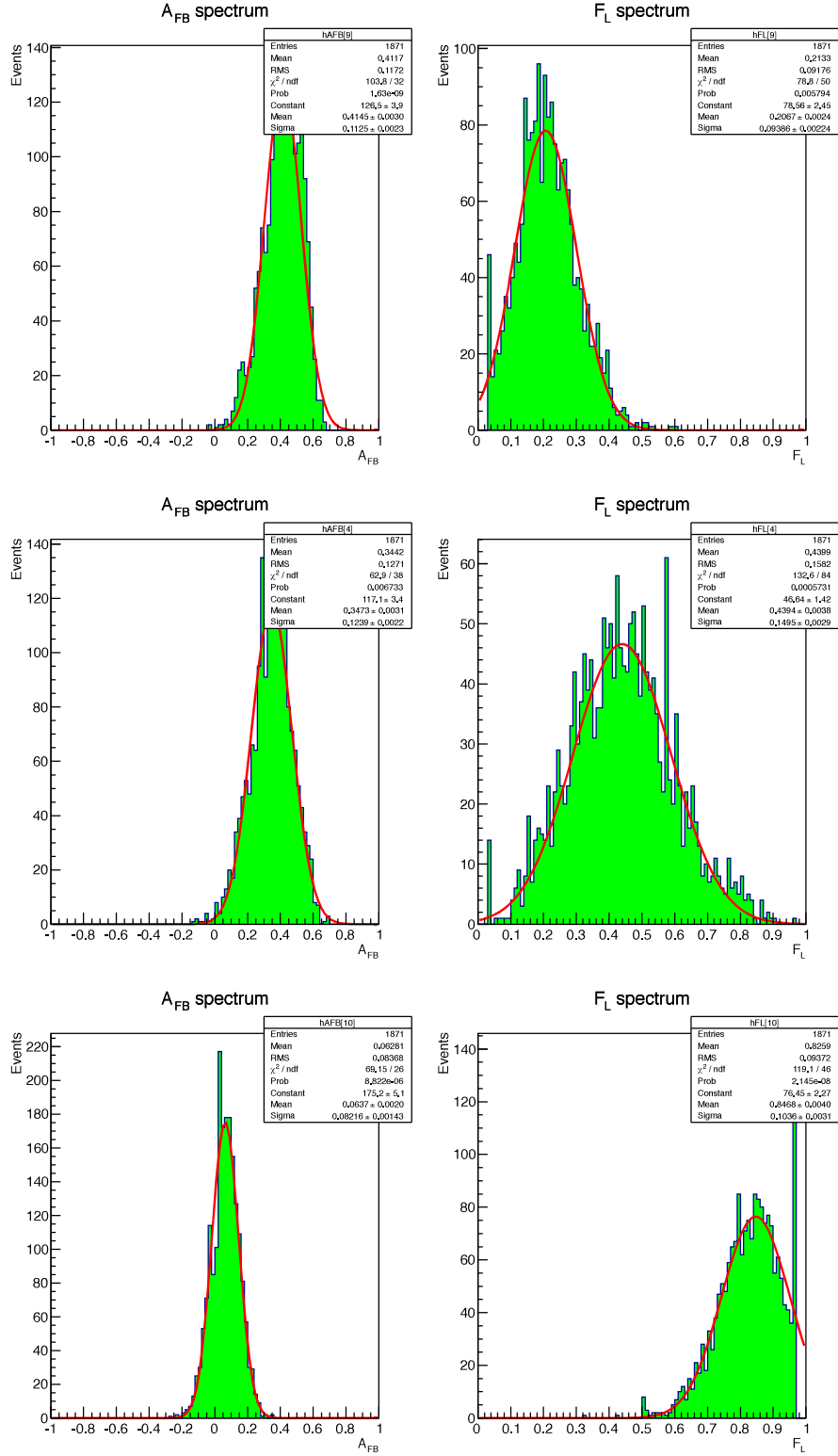
Figure 4.23: A_{FB} and F_L distribution for all subsamples for bin 0,2 and 4 respectively.

interesting variables. The comparison results for A_{FB} and F_L for both subsamples at GEN and RECO are presented in Figure 4.24. The GEN level results are in black plus sign with vertical line denoting statistical errors while the RECO level results are in black points with red band denoting statistical errors respectively.

The projections of B mass and angular variables $\cos\theta_L$, $\cos\theta_K$ distributions in each q^2 bin for subsample 1 and 2 are shown in Figures 4.25-4.27 and 4.28-4.30 respectively.

Figure 4.24: Comparison of A_{FB} and F_L values at both GEN(black square and black plus) and RECO(black dot and red band) level in each q^2 bin for both subsamples. The top and bottom row plots present A_{FB} and F_L for subsample 1 and 2 respectively. The errors here are purely statistical.

From these plots, it's clear that the fitting results are quite stable for different subsamples in data-like conditions.

4.8.4 Validation with Mixing MC sample

This fitting procedure is validated with the mixing simulation containing signal, peaking and combinatorial backgrounds. In this case, the background is still pure toy from fitting

Figure 4.25: Projection of fitting results from cocktail MC in B mass distribution in each q^2 bin(left to right)

Figure 4.26: Projection of fitting results from cocktail MC in $\cos\theta_K$ distribution in each q^2 bin(left to right)

Figure 4.27: Projection of fitting results from cocktail MC in $\cos\theta_L$ distribution in each q^2 bin(left to right)

Figure 4.28: Projection of fitting results from cocktail MC in B mass distribution in each q^2 bin(left to right)

Figure 4.29: Projection of fitting results from cocktail MC in $\cos\theta_K$ distribution in each q^2 bin(left to right)

Figure 4.30: Projection of fitting results from cocktail MC in $\cos\theta_L$ distribution in each q^2 bin(left to right)

results whereas the signal is taken from the official signal MC sample. The full statistics correspond to ~4000 fb^{-1}, divided into 2 subsamples having ~2000 fb^{-1} luminosity each. The aim is to verify whether in data-like conditions and with large statistics, the analysis is able to measure interesting variables. The comparison results for A_{FB} and F_L for both subsamples at GEN and RECO are presented in Figure 4.31. GEN level results are in black plus sign with vertical line denoting statistical errors. RECO level results are in black points with red band denoting statistical errors respectively.

The projections of B mass and angular variables $\cos\theta_L$, $\cos\theta_K$ distributions in each q^2 bin for subsample 1 and 2 are shown in Figures 4.32-4.34 and 4.35-4.37 respectively.
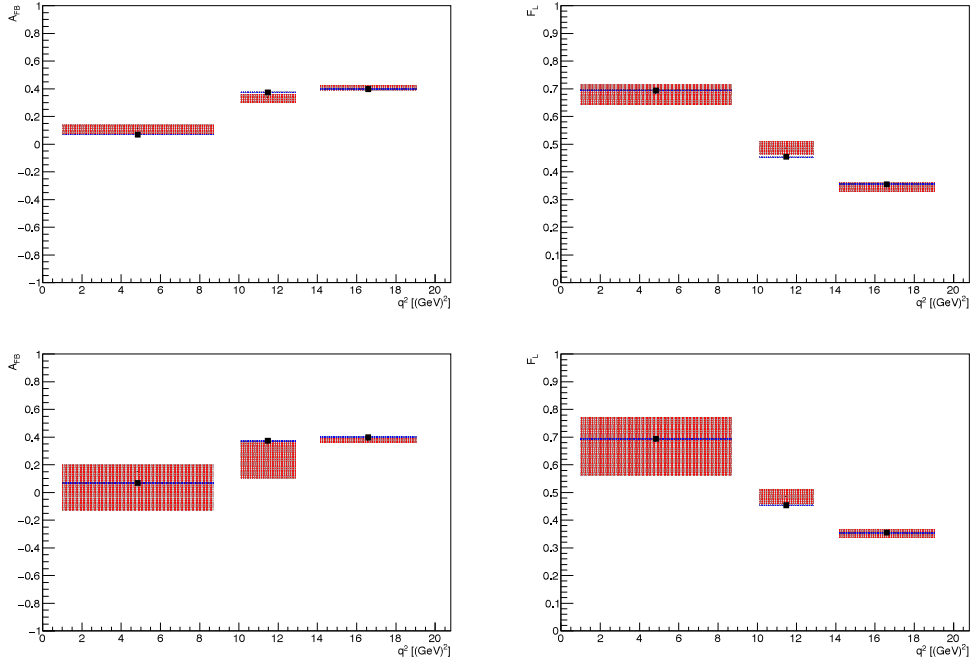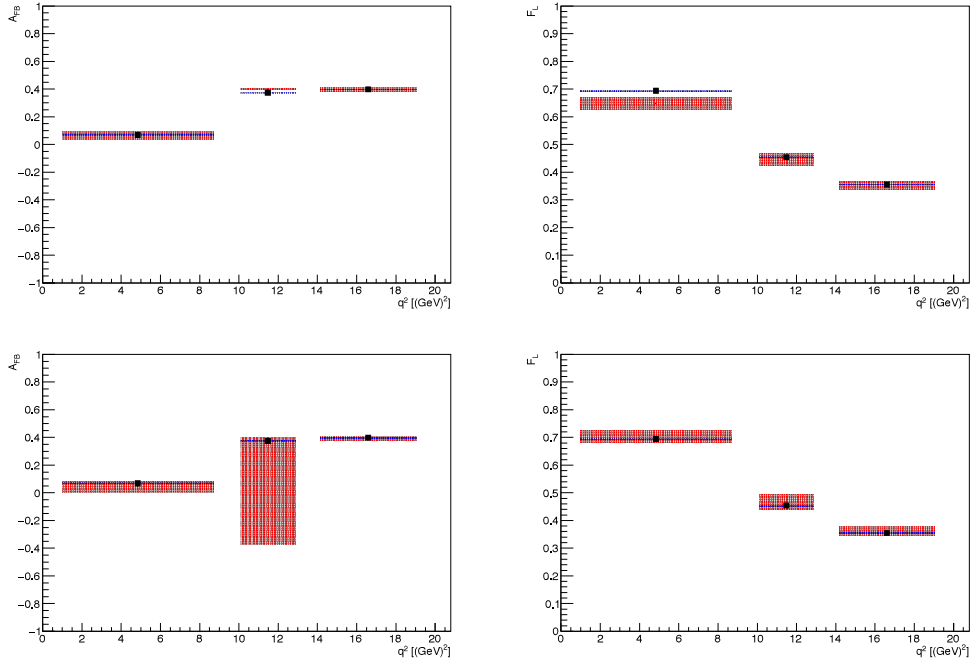

Figure 4.31: Comparison of A_{FB} and F_L values at both GEN(black square and black plus) and RECO(black dot and red band) level in each q^2 bin for both subsamples. The top and bottom row plots present A_{FB} and F_L for subsample 1 and 2 respectively. The errors here are purely statistical.

The fitting results are quite stable for different subsamples in data-like conditions which is clear from Figure 4.31.
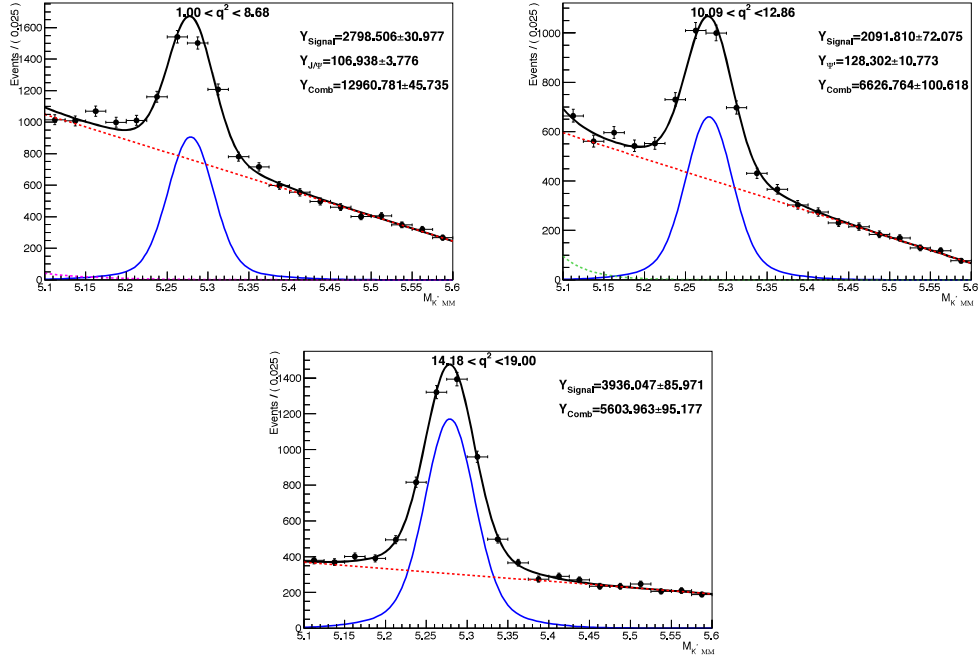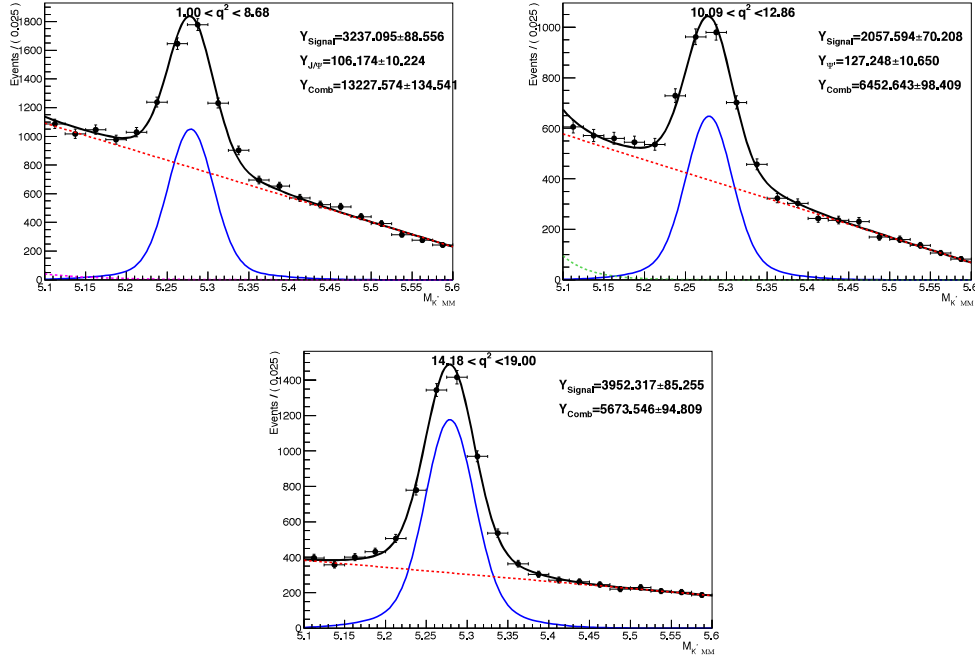
Figure 4.32: Projection of fitting results from mixing MC in B mass distribution in each q^2 bin(left to right)
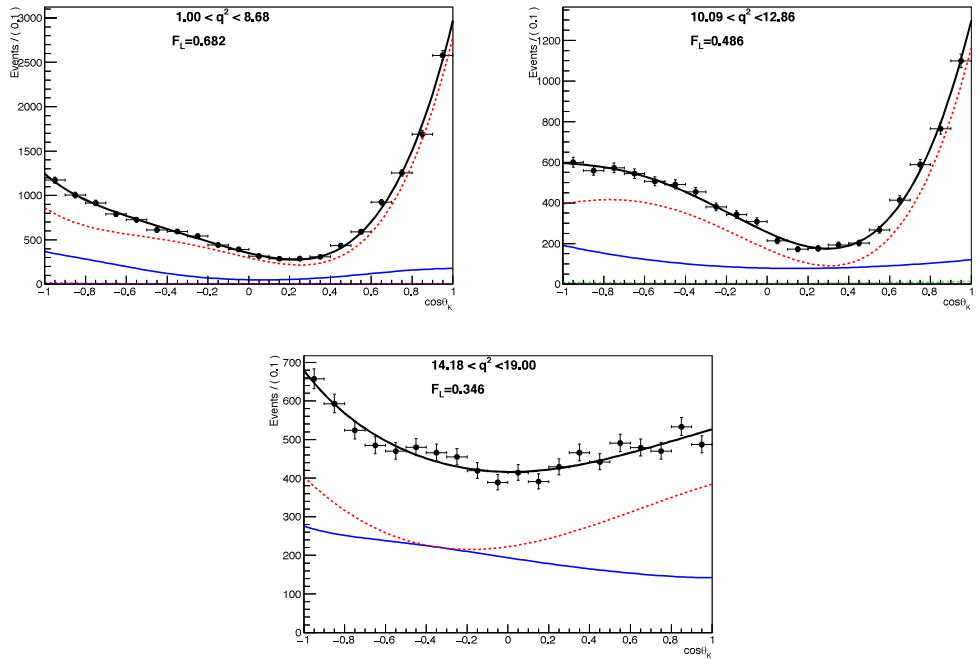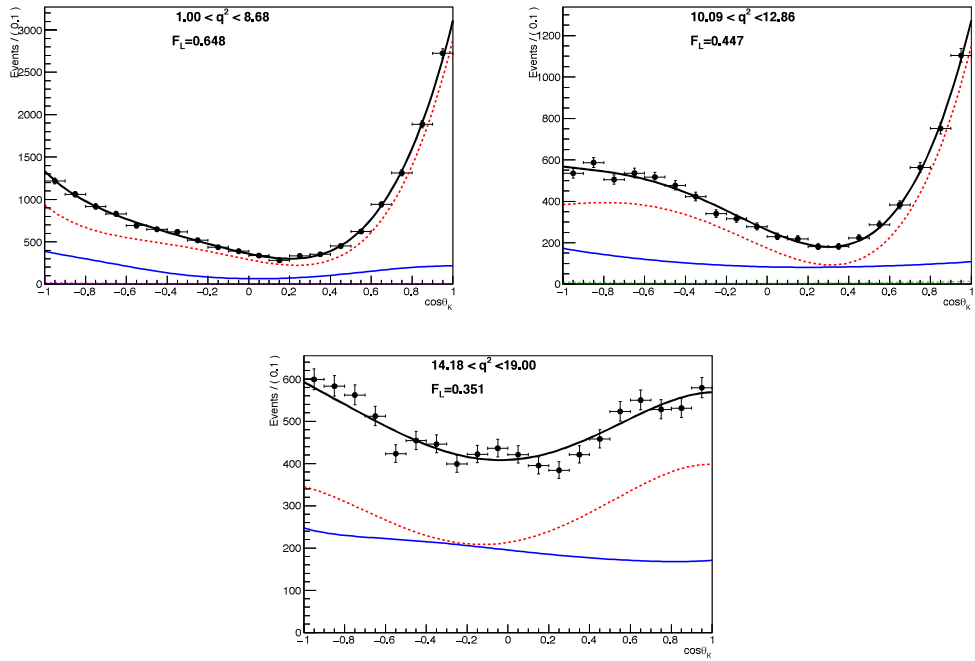

Figure 4.33: Projection of fitting results from mixing MC in $\cos\theta_K$ distribution in each q^2 bin(left to right)
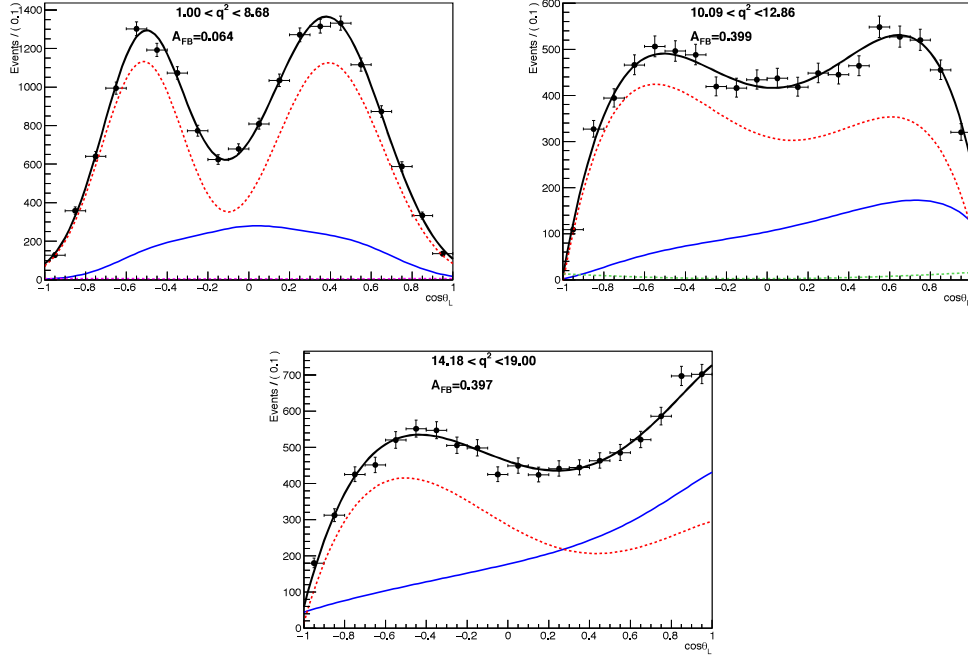
Figure 4.34: Projection of fitting results from mixing MC in $\cos\theta_L$ distribution in each q^2 bin(left to right)
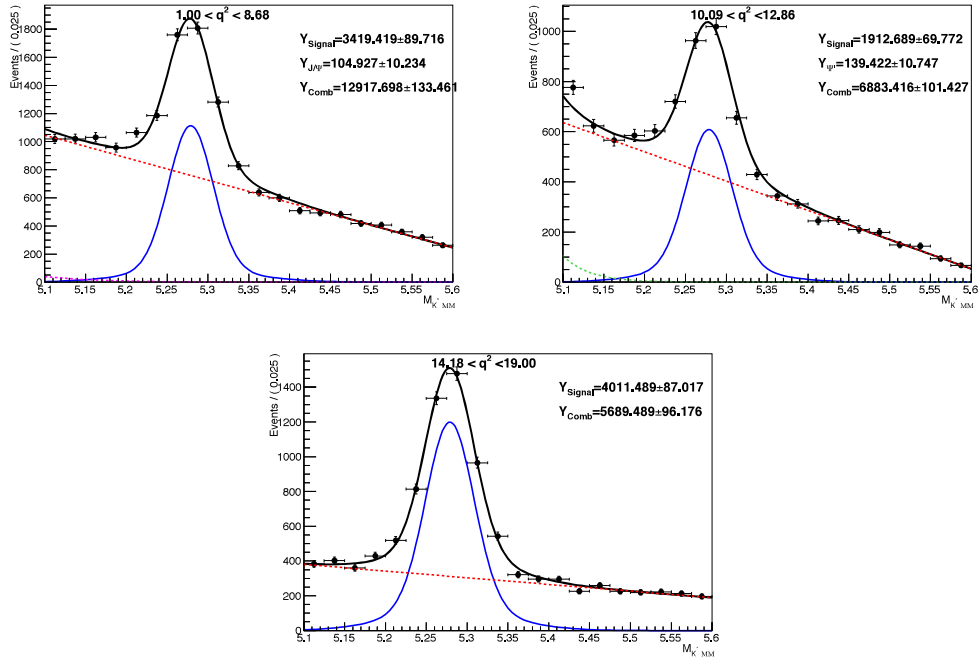
Figure 4.35: Projection of fitting results from mixing MC in B mass distribution in each q^2 bin(left to right)
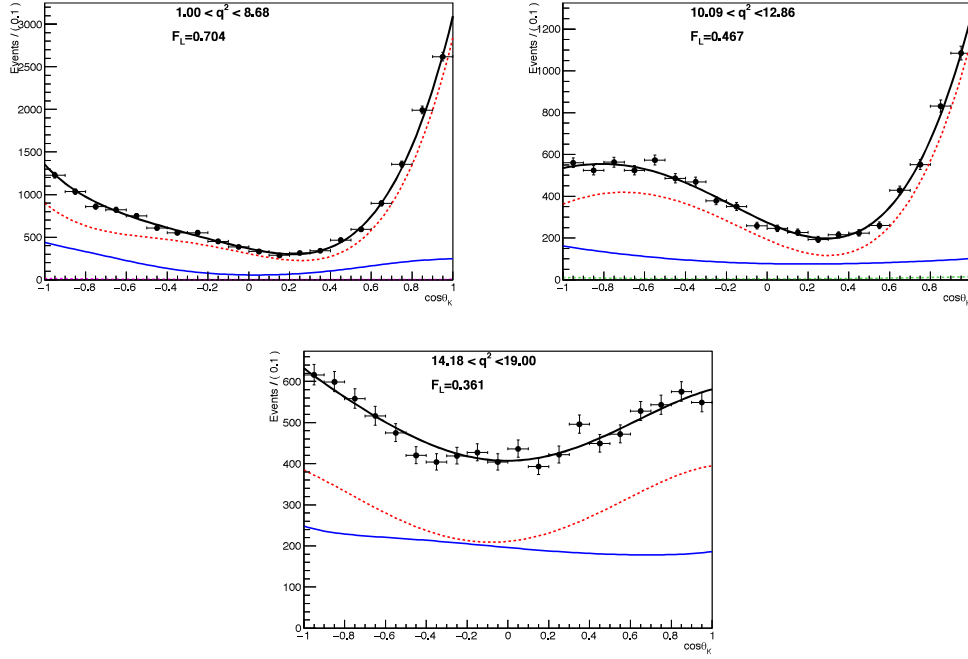
Figure 4.36: Projection of fitting results from mixing MC in $\cos\theta_K$ distribution in each q^2 bin(left to right)
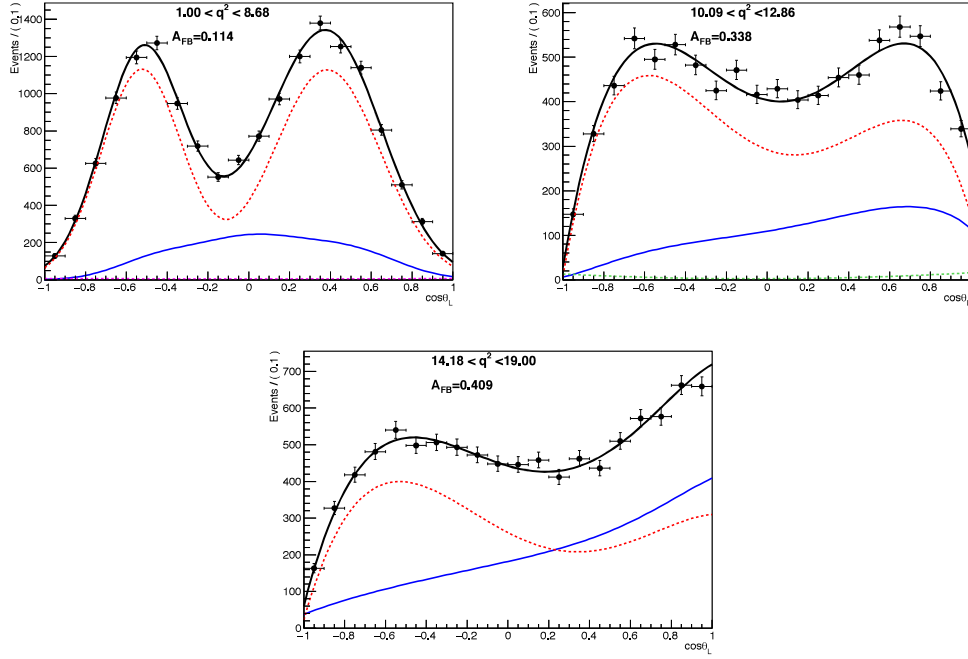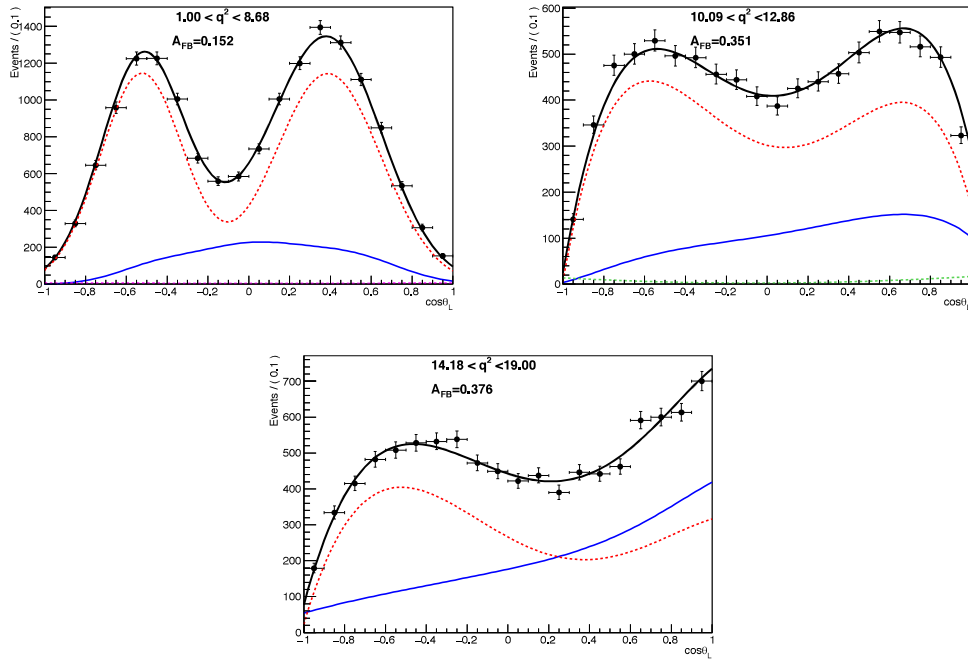

Figure 4.37: Projection of fitting results from mixing MC in $\cos\theta_L$ distribution in each q^2 bin(left to right)
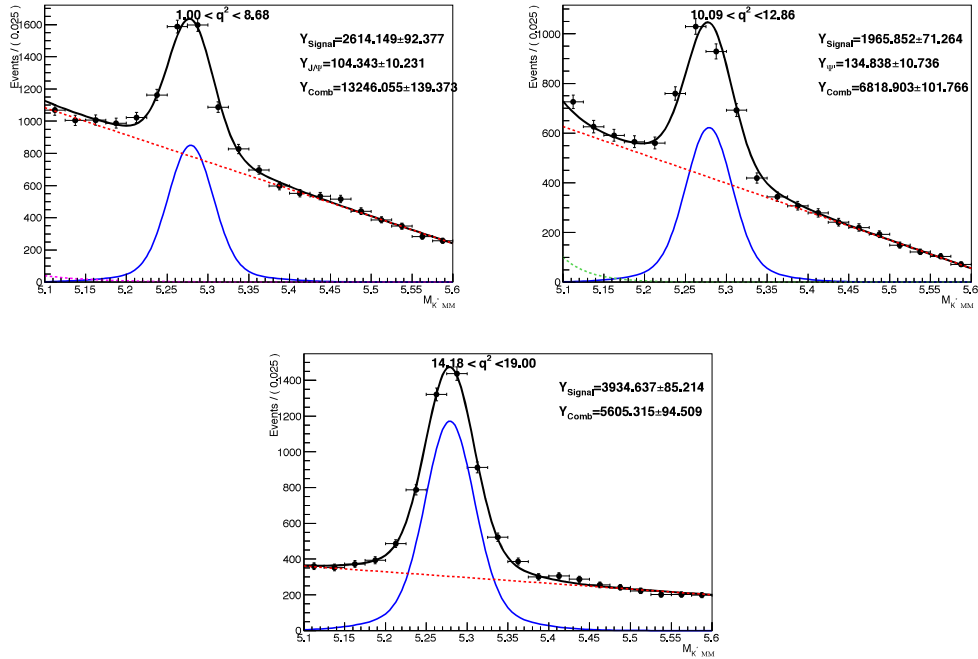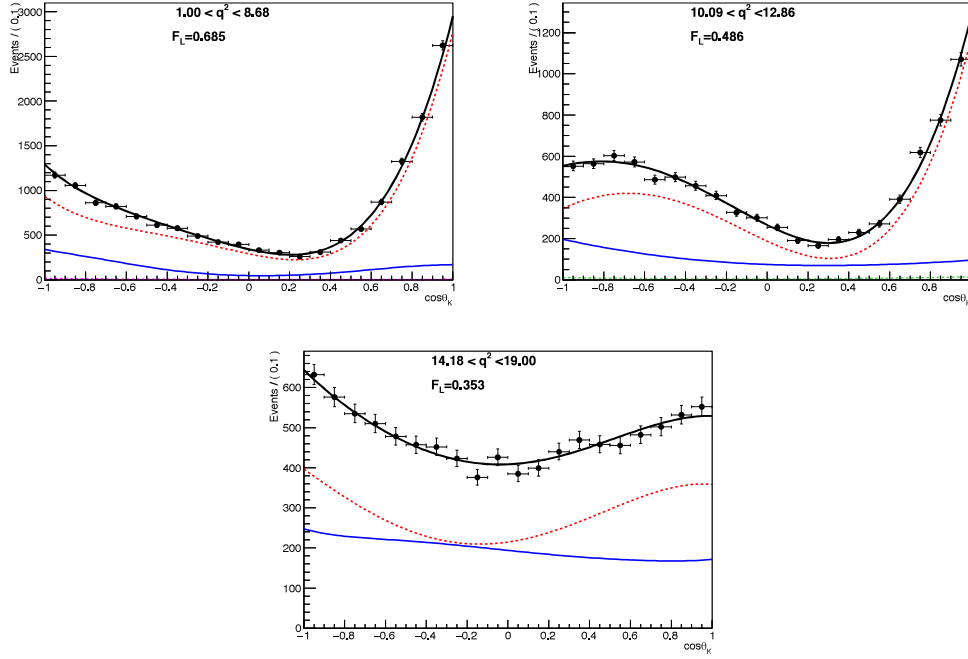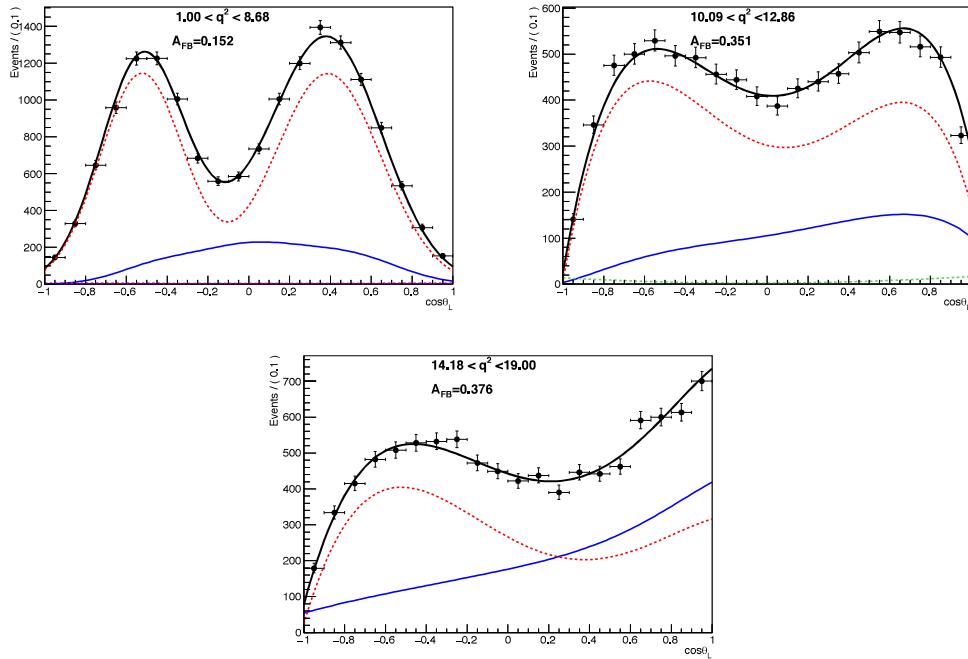
4.9   Fitting Results from data

We need to measure the fraction of longitudinal polarization of the K^{*+}, F_L, and the forward-backward asymmetry of the muons, A_{FB}, as a function of q^2 for the decay $B^+ \rightarrow K^{*+}\mu^+\mu^-$.

The q^2 binning, the PDF used, fitting steps, the strategy and its quality control are described in detail in Sec. 4.4.2. Procedures used are validated after fitting in Sec. 4.8, the full fitting procedures are applied to the data in order to get the results. The final fitting to the data is performed in several steps. The procedures and major steps in sequence are already described in Sec. 4.4.2.

In this section, we show the details and show results from each of the fitting components and steps. The section 4.9.1 described all the input components required by the final fitting of data. The results of the measurements are presented in Sec. 4.9.4.

4.9.1   Components of the fitting to data

We are now ready to obtain and check each item of the PDF for the angular fitting as described in Sec. 4.4.2.

4.9.1.1   Signal Shape

$S_i^M(m)$ describes the signal shape for signal events as function of $K^*\mu\mu$ invariant mass. It is parameterized with double gaussian with shared mean (namely m_0). Figure 4.38 shows this shape from signal simulation.

4.9.1.2   Peaking background shape

$B_i^{Mp}(m)$, $B_i^{\theta_K p}(\theta_K)$, $B_i^{\theta_l p}(\theta_l)$ describes the peaking background shape for B invariant mass, $\cos\theta_k$ and $\cos\theta_l$ respctively. The details about the parameterization is explained in Sec. 4.4.2. The corresponding shapes are shown in Figure 4.39-4.42.
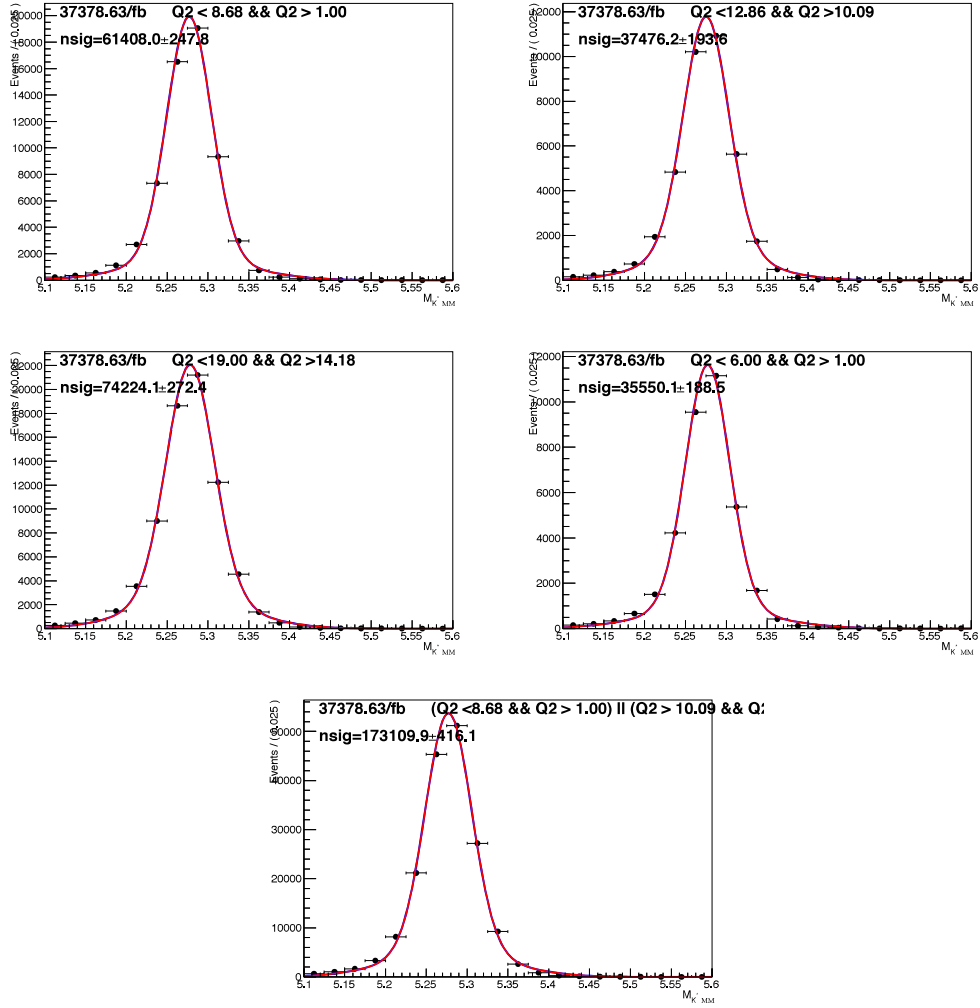
Figure 4.38: B invariant mass of the signal shape from simulation in each q^2 bin in Table 4.1 except bin 1 and 3. The fit results are used to get the $S_i^M(m)$ component of the p.d.f. The degrees of freedom to compute the fit χ^2 are simply the number of bins. The numbering goes from left to right and from top to bottom.
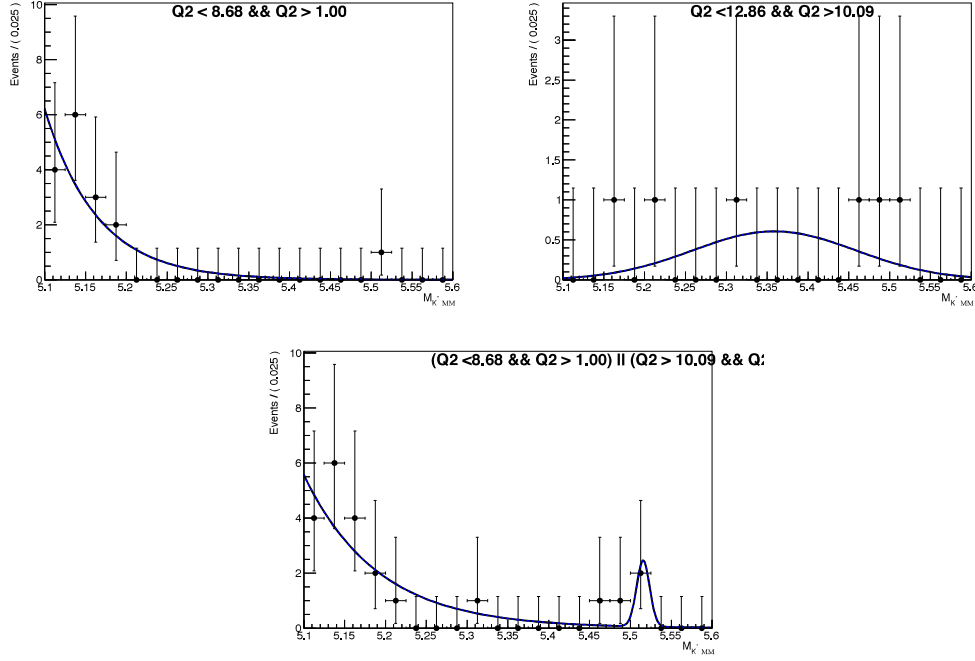
Figure 4.39: B invariant mass of $B^+ \to K^{*+}J/\psi$ peaking background sample from simulation for q^2 bin 0,2 and 6(from left to right). No contributions in bin 5.
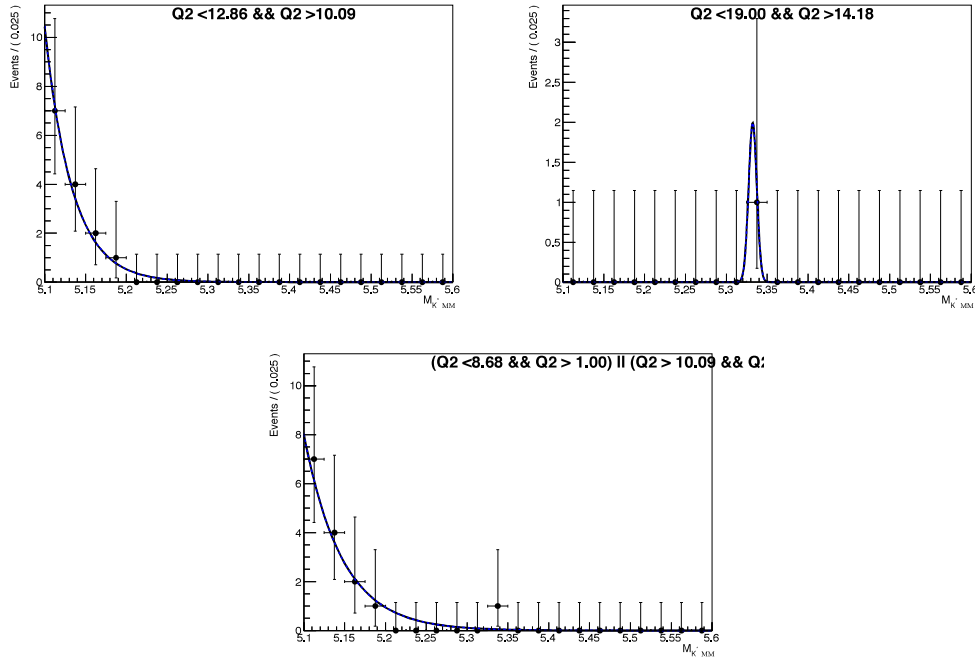
Figure 4.40: B invariant mass of $B^+ \to K^{*+}\psi'$ peaking background sample from simulation for q^2 bin 2,4 and 6(from left to right). No contributions in bin 5.
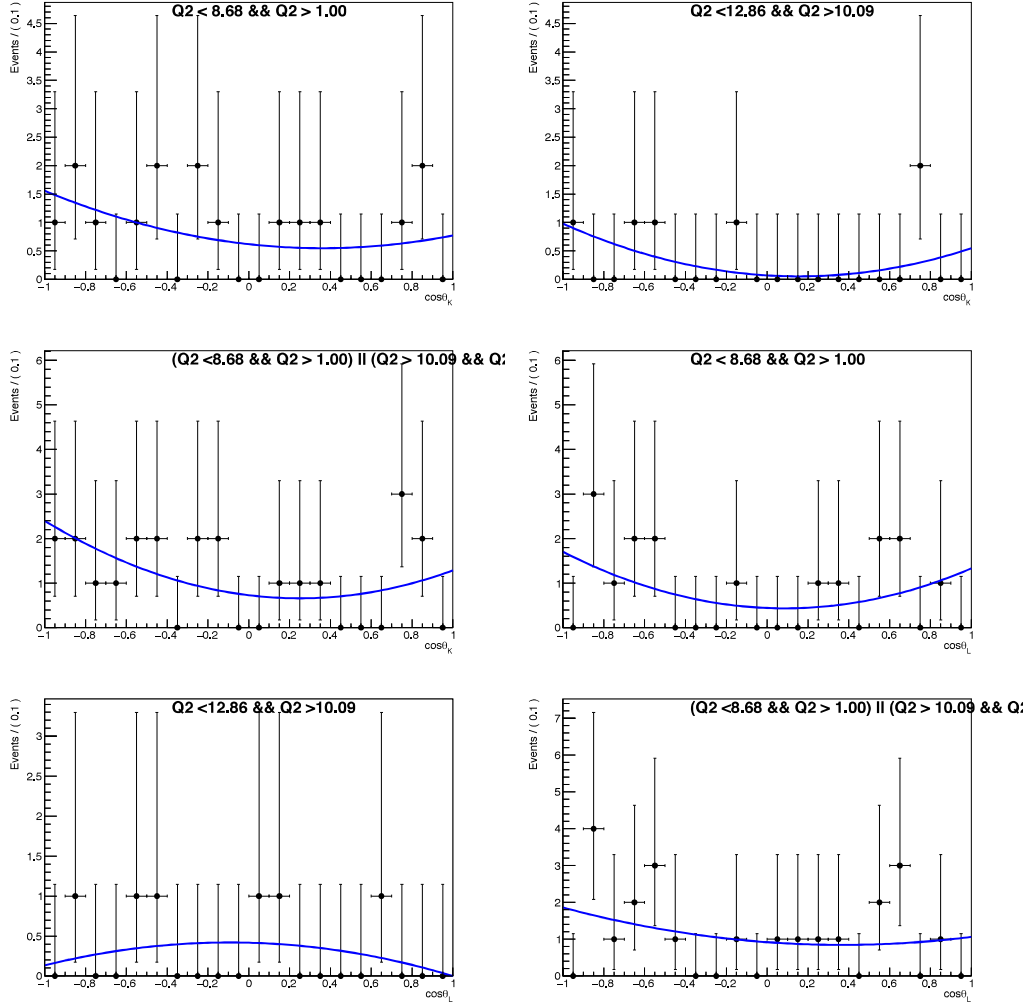
Figure 4.41: $\cos\theta_k$, $\cos\theta_l$ distribution of $B^+ \to K^{*+}J/\psi$ peaking background sample from simulation for q^2 bin 0,2 and 6(from left to right). No contributions in bin 5.
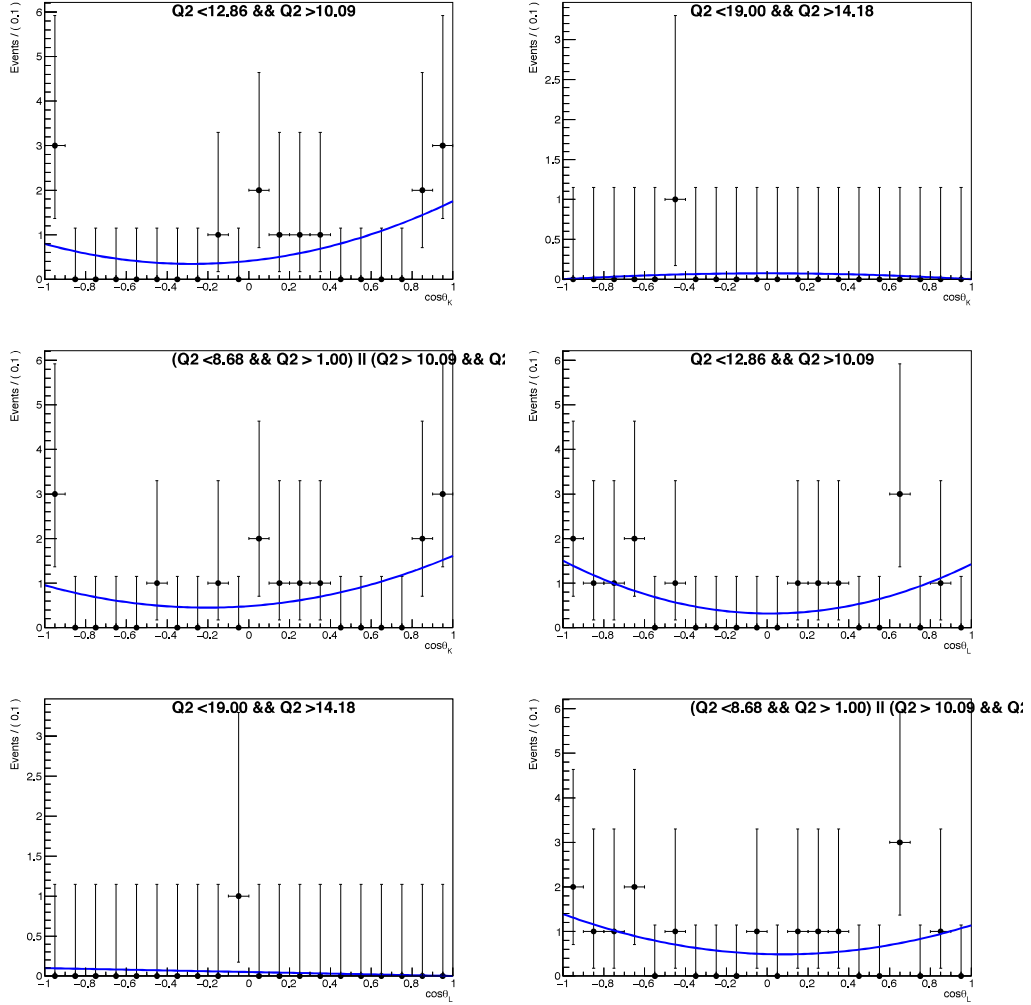
Figure 4.42: $\cos\theta_k$, $\cos\theta_l$ distribution of $B^+ \to K^{*+}\psi'$ peaking background sample from simulation for q^2 bin 2,4 and 6(from left to right). No contributions in bin 5.

4.9.1.3 Combinatorial background shape

$B_i^{Mc}(m)$, $B_i^{\theta_K c}(\theta_K)$, $B_i^{\theta_l c}(\theta_l)$ describes the combinatorial background shape for B invariant mass, $\cos\theta_k$ and $\cos\theta_l$ respctively. The details about the parameterization is explained in Sec. 4.4.2. The corresponding shapes for angular variables $\cos\theta_l$ and $\cos\theta_k$ are shown in Figures 4.43, 4.44.
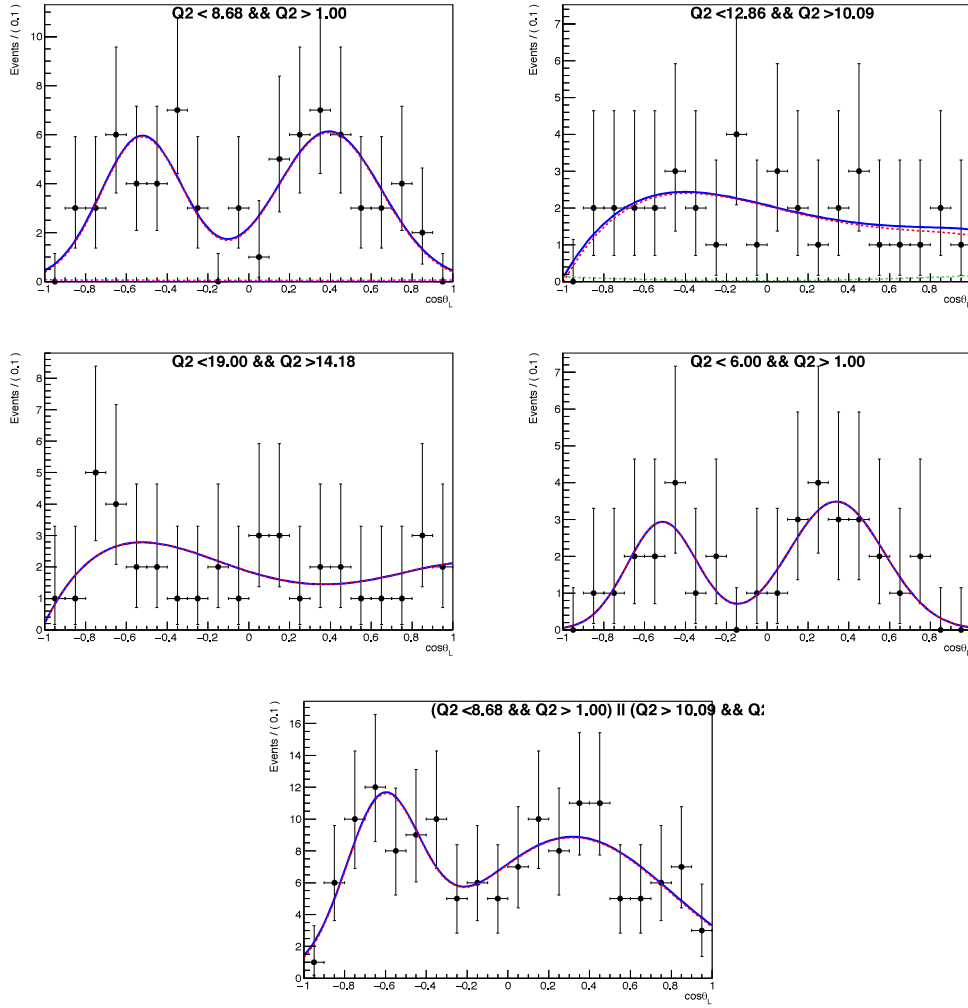
Figure 4.43: $\cos\theta_l$ distribution from data sideband for each q^2 (from left to right). The red dashed line represents combinatorial background whereas pink and green dashed lines represent peaking backgrounds.

115
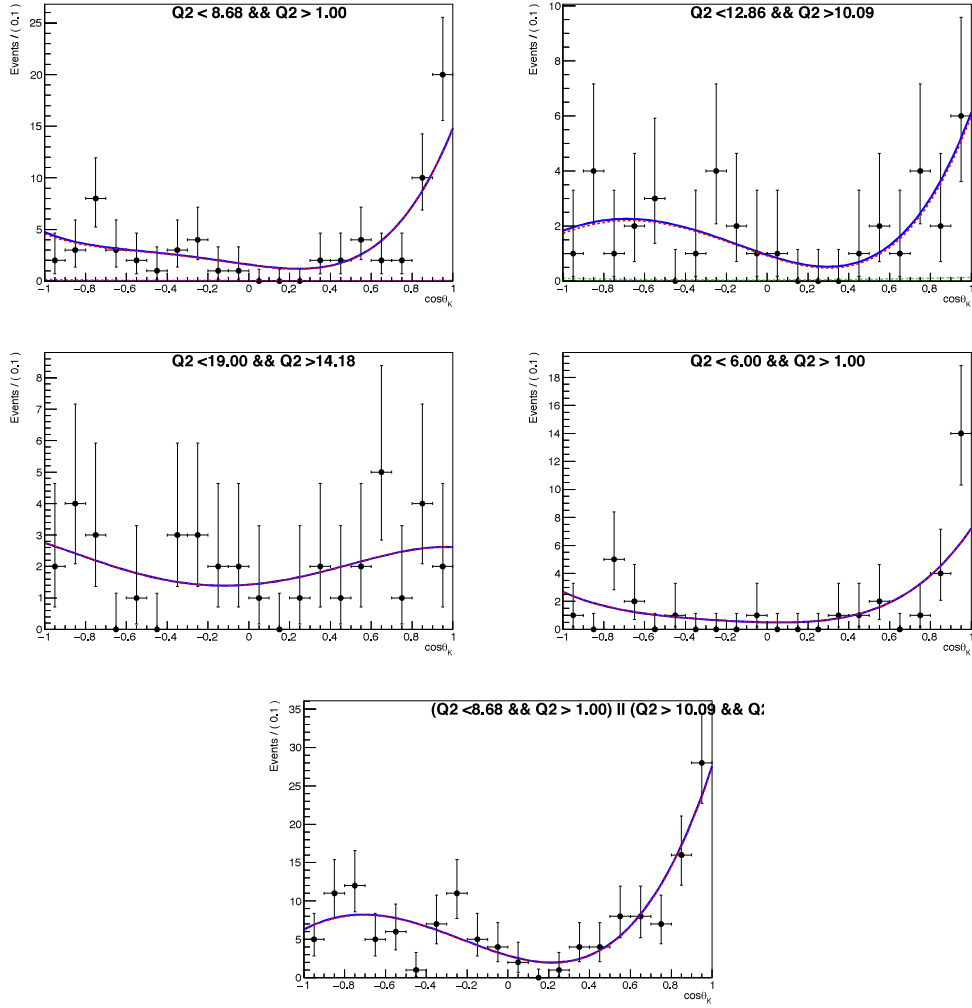
Figure 4.44: $\cos\theta_k$ distribution from data sideband for each q^2 (from left to right). The red dashed line represents combinatorial background whereas pink and green dashed lines represent peaking backgrounds.

q^2 bin	Y_S	Y_B^C	$Y_B^P(J/\psi)$	$Y_B^P(\psi')$
0	24.6 ± 5.7	132.5 ± 8.9	1.0 ± 0.7	0
2	27.8 ± 6.9	59.8 ± 9.1	0	1.3 ± 1.1
4	42.3 ± 7.7	52.7 ± 8.4	0	0
5	11.3 ± 4.9	61.7 ± 8.2	0	0
6	96.5 ± 12.3	242.1 ± 15.2	1.6 ± 1.0	1.5 ± 0.9

Table 4.6: Yields for both signal and background. Errors are purely statistical.

4.9.2 Yields and projection plots from the fitting

After putting all the components into the final fitting step, we could obtain the final fitting results in data. The signal and background yields are summarized in Table 4.6.

The projection plots from 3D fits are made for all q^2 bins. Figure 4.45 shows the projection in B mass distribution. Figures 4.46, 4.47 show the projections in angular $\cos\theta_l$, $\cos\theta_k$ distributions.

From these we could further obtain the measured values of F_L and A_{FB} with data for the decay $B^+ \to K^{*+}\mu^+\mu^-$, in the dimuon q^2 bins. The results will be shown in Sec. 4.9.4.

4.9.3 F&C method for statistical error estimation

While performing the fit to data to get the fitting results for both A_{FB} and F_L in different q^2 bins, MINOS is failing to give the correct estimation of the statistical error for both A_{FB} and F_L because the central values of the fitting results lie very close to the physical boundary. Then how to estimate the statistical error in a correct way ? We have followed a method aka **"Feldman-Cousins method"** as described in [54]. In this method, we run many different sets of pseudo-experiments created at many different "true"(generated) values of $A_{FB}(F_L)$. For each generated value of $A_{FB}(F_L)$, we create a 68.4% acceptance interval. This acceptance interval is a range in measured value of $A_{FB}(F_L)$ for a given true(generated) value of $A_{FB}(F_L)$ so that 68.4% of the pseudo-experiments are included. For each generated value of $A_{FB}(F_L)$ chosen, we plot horizontally the associated accep-
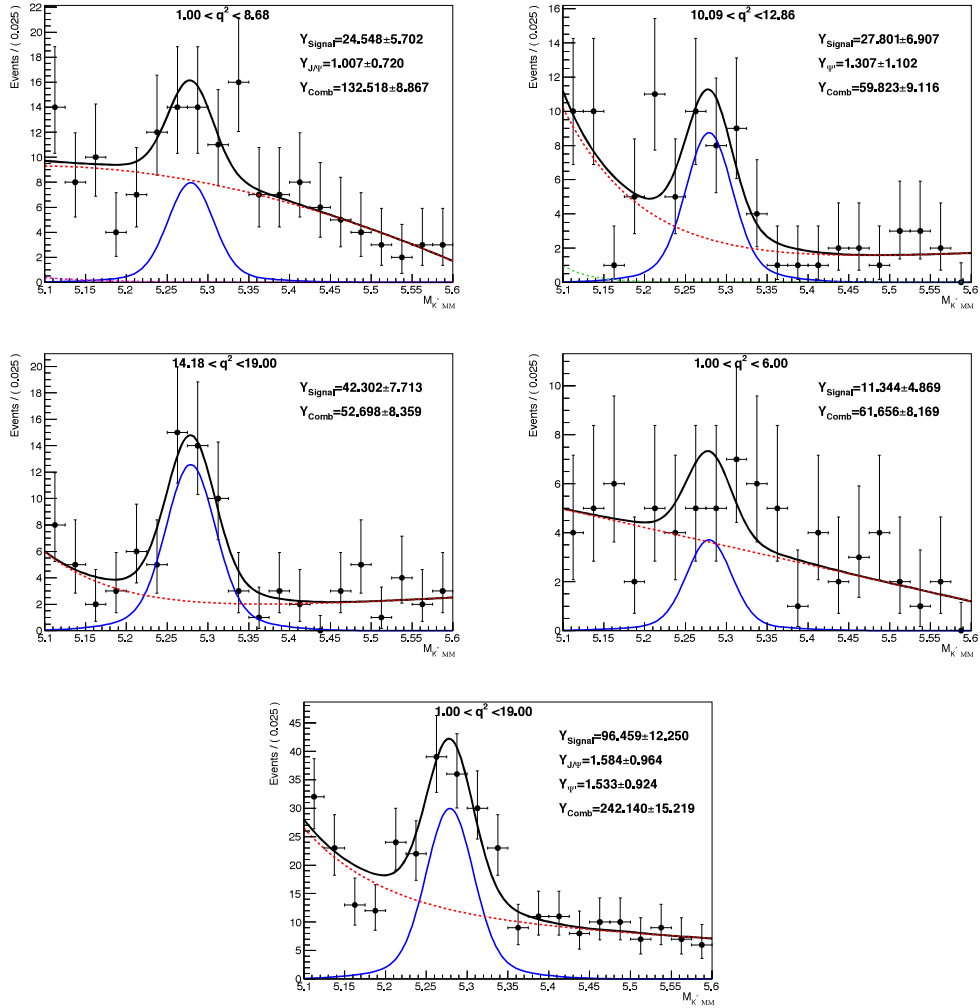
Figure 4.45: Projection of fit results from data in B mass distribution for each q^2 (from left to right).
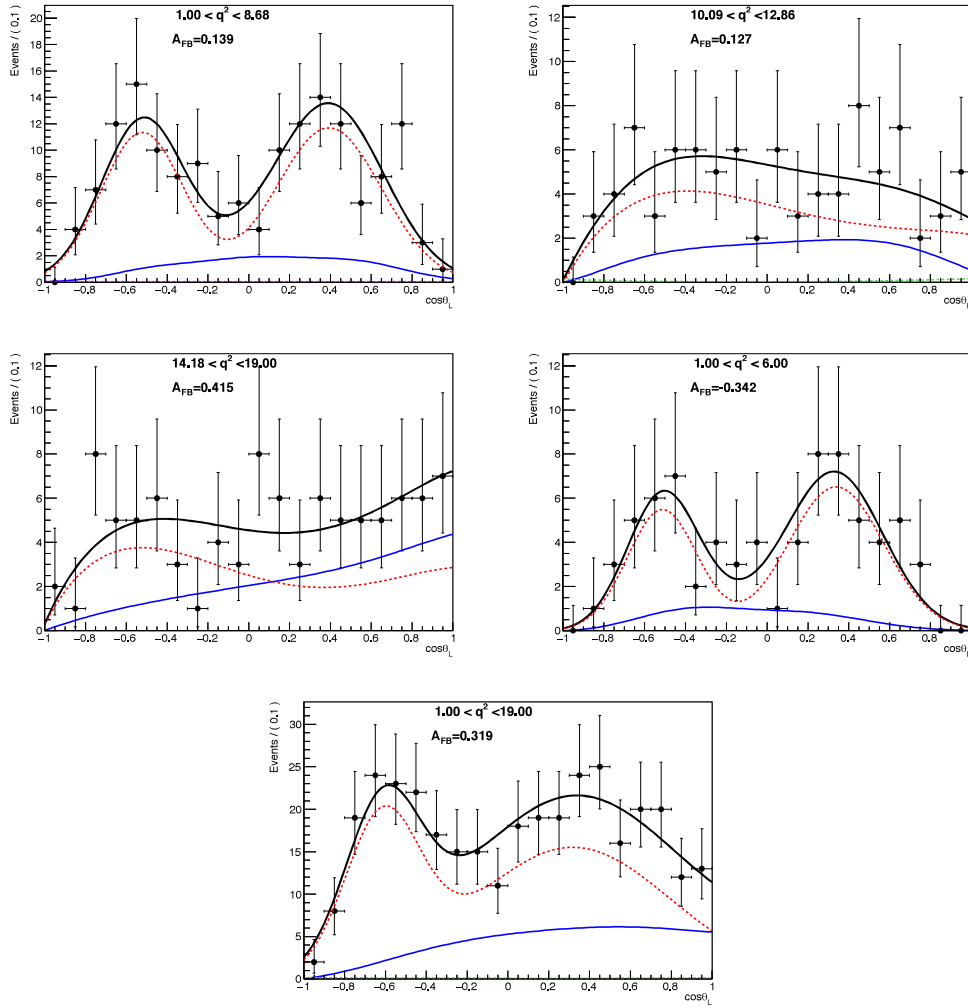
Figure 4.46: Projection of fit results from data in $\cos\theta_l$ distribution for each q^2 (from left to right).

119
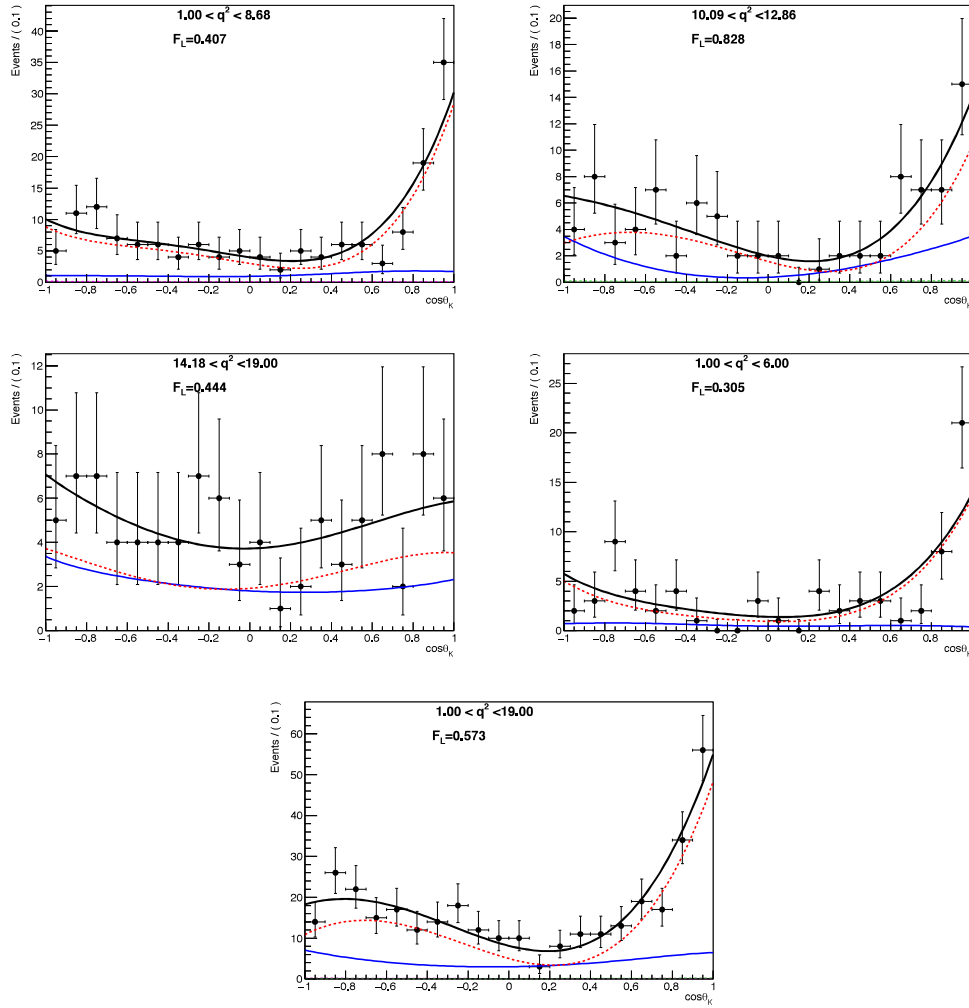
Figure 4.47: Projection of fit results from data in $\cos\theta_k$ distribution for each q^2 (from left to right).

q^2 bin	A_{FB}	A_{FB}(SM)	F_L	F_L(SM)
0	$0.139^{+0.296}_{-0.301}$	0.077 ± 0.097	$0.407^{+0.191}_{-0.204}$	0.673 ± 0.306
2	$0.127^{+0.000}_{-0.106}$	N.A	$0.828^{+0.000}_{-0.248}$	N.A
4	$0.415^{+0.000}_{-0.159}$	0.366 ± 0.030	$0.444^{+0.001}_{-0.152}$	0.346 ± 0.035
5	$-0.342^{+0.329}_{-0.173}$	-0.034 ± 0.039	$0.305^{+0.000}_{-0.305}$	0.716 ± 0.269
6	$0.319^{+0.000}_{-0.079}$	N.A	$0.573^{+0.000}_{-0.138}$	N.A

Table 4.7: Results of the measurement of the forward-backward asymmetry of the muons, A_{FB} and fraction of longitudinal polarization of the K^{*+}, F_L which are reported in 2nd and 4th columns whereas the SM predictions [55–58] are reported in 3rd and 5th columns. The errors are purely statistical.

tance interval. For quoting the value for two-sided intervals, a vertical line is placed at the measured value. If the vertical line intercepts both sides of the acceptance interval and then we quote a two sided interval as quoted in Figure 4.49.

4.9.4   Results for A_{FB} and F_L in data

The results of the measurement of forward-backward asymmetry of the muons, A_{FB} and the fraction of the longitudinal polarization of K^{*+}, F_L for the decay $B^+ \rightarrow K^{*+}\mu^+\mu^-$, are shown in Figure 4.48. The statistical errors for both A_{FB} and F_L in each q^2 bin have been calculated using **F&C method**, the details about this method can be found in Sec. 4.9.3 and the corresponding plots are shown in Figure 4.49.

The numerical results are tabulated in Table 4.7.

4.10   Systematic Uncertainties

In this section, the systematic uncertainties that affect the results are listed, described and evaluated. The possible sources of systematic uncertainties investigated are:

simulation mismodelling: pure signal-simulation with a large number of events is checked to validate the capability of the analysis to measure the interesting observables;

efficiency shape: the shape of the efficiency is validated by measuring the interesting
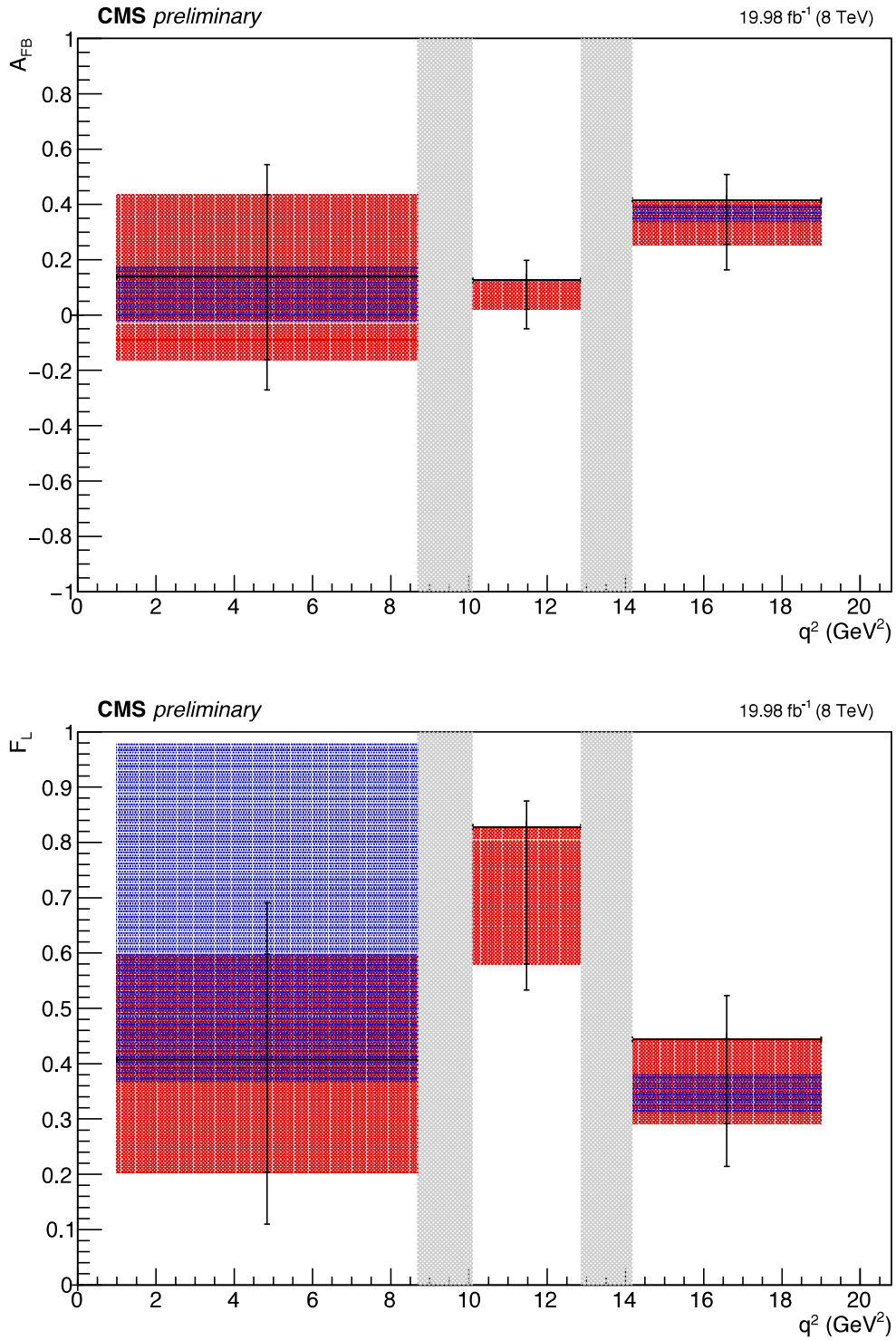
Figure 4.48: Results of the measurement of A_{FB} (top plot) and F_L (bottom plot) in data. The plots show the values as a function of the dimuon mass squared (q^2). The red shaded region represents the statistical uncertainty. the systematic uncertainties are represented by black vertical error bars with edges. The standard model predictions are represented by blue shaded region. The grey shaded regions represent two resonance regions.
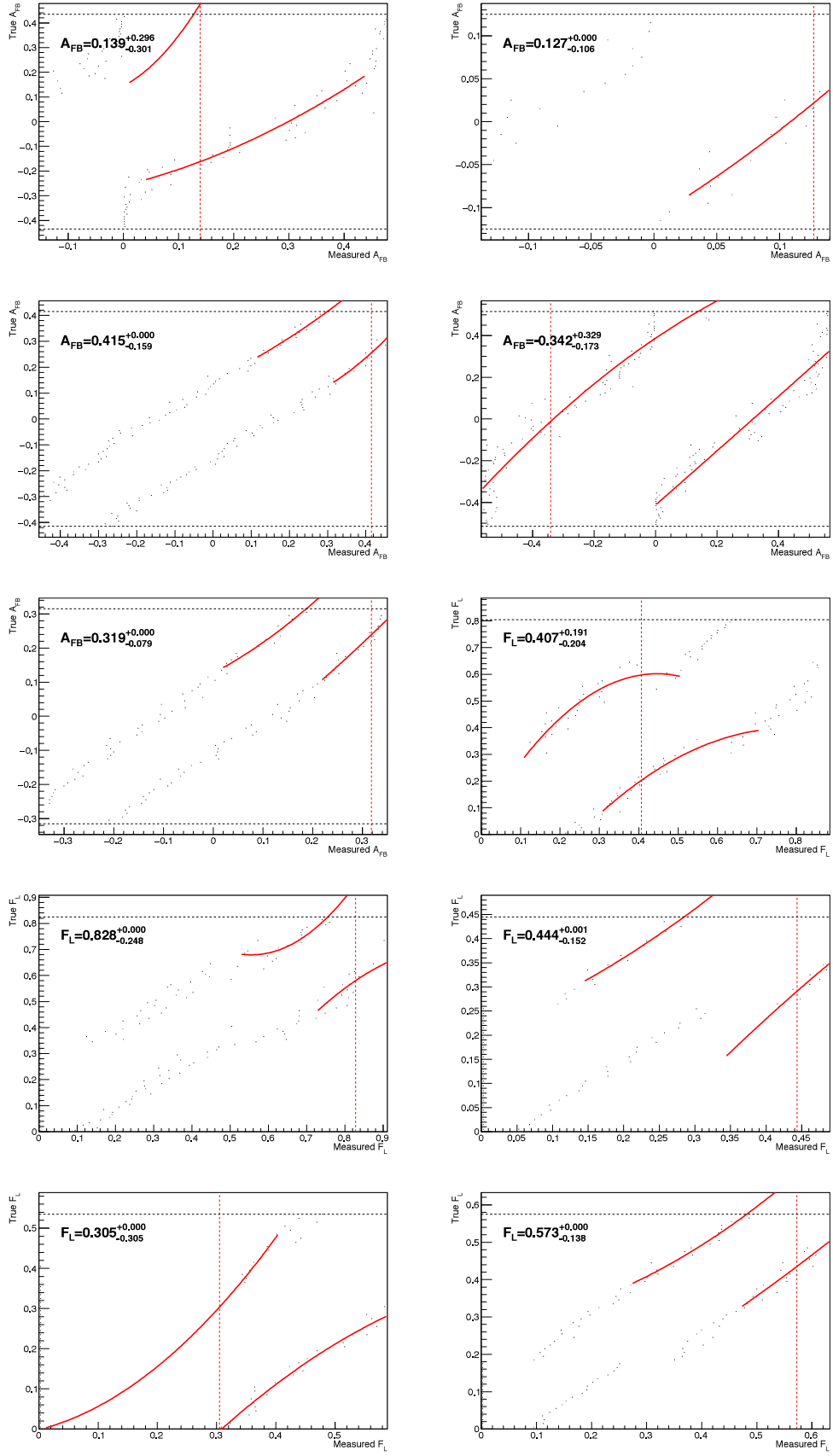
Figure 4.49: F&C Plots for both A_{FB} and F_L in each q^2 bin.

observables with data control channels;

background mismodelling: the particular functional form chosen to fit the background events might affect the final results of the analysis;

angular resolution: the angular variables have finite resolution which might affect the final result of the analysis.

S-*P* **wave interference:** the $K_S - \pi$ in the final state can be either generated from the vector meson K^{*+} decay, they would be therefore in a *P*-wave state, or not generated from such a resonance, they would be therefore in an *S*-wave state. The two final states have different angular distributions.

4.10.1 Simulation Mismodelling

The signal simulation samples are used to validate the procedures to extract the interesting observables in extremely favorable conditions, namely with a large number of events as described in Sec. 4.8.1.

The angular fitting results between using private unfiltered signal simulation sample and the official signal sample at reconstruction level are compared and the comparison plots are shown in Figure 4.21. The difference between them are evaluated as the uncertainties due to simulation mismodelling. The results are summarized in Tables 4.8, 4.9 as "simu. mismodel".

4.10.2 Efficiency Shape

The efficiency shapes used in fitting are based on signal MC samples. The validation described in Sec. 4.8.1 shows the cosistency between GEN and RECO level results, which also reflects consistency of private sample and official MC sample.

To evaluate the uncertainty due to efficiency parametrization, we changed the efficiency shape from the default description to alternative one, and check the differences of results

124

obtained and use it as an estimation of systematic uncerinties caused by efficiency shapes.

The default efficiency in fitting are 6th order polynomial or 3 gaussians depending on q^2 bin as described in Sec. 4.7.3 and the alternative form of efficiency used was 7th order polynomial for all q^2 bins. The plots of alternative efficiency descriptions that are used to get the estimation of systematic uncertainty are shown in Figure 4.50.

The systematic uncertainties caused by efficiency description are listed in Tables 4.8, 4.9 with the label "efficiency shape".

4.10.3 Background Mismodelling

In order to evaluate the systematic uncertainty introduced by a particular background shape used in this analysis, we used different form of background shapes to evaluate the effects.

Data are alternatively fitted with polynomial or gaussian increased by one order w.r.t the nominal pdf used. The values of A_{FB}, F_L are compared with the results obtained using nominal pdf. The difference on the measurement of interesting variables is considered as the systematic uncertainty and they are considered to be symmetric.

Firstly, we increased the combinatorial background angular shape function to 3 gaussian for $\cos\theta_L$ and 5th order polynomial for $\cos\theta_K$. This uncertainty is labelled as "comb. bkg. shape" in Tables 4.8, 4.9.

Secondly, to evaluate the systematic uncertainty due to peaking background, the angular shape function is changed from 4th to 5th order polynomial. And the corresponding results are listed in Tables 4.8, 4.9 as "pkg. bkg. shape".

4.10.4 Angular Resolution

The angular variables θ_K,θ_L have finite resolution which might affect the fit results. The comparison is performed with the results of the interesting observables A_{FB} and F_L by
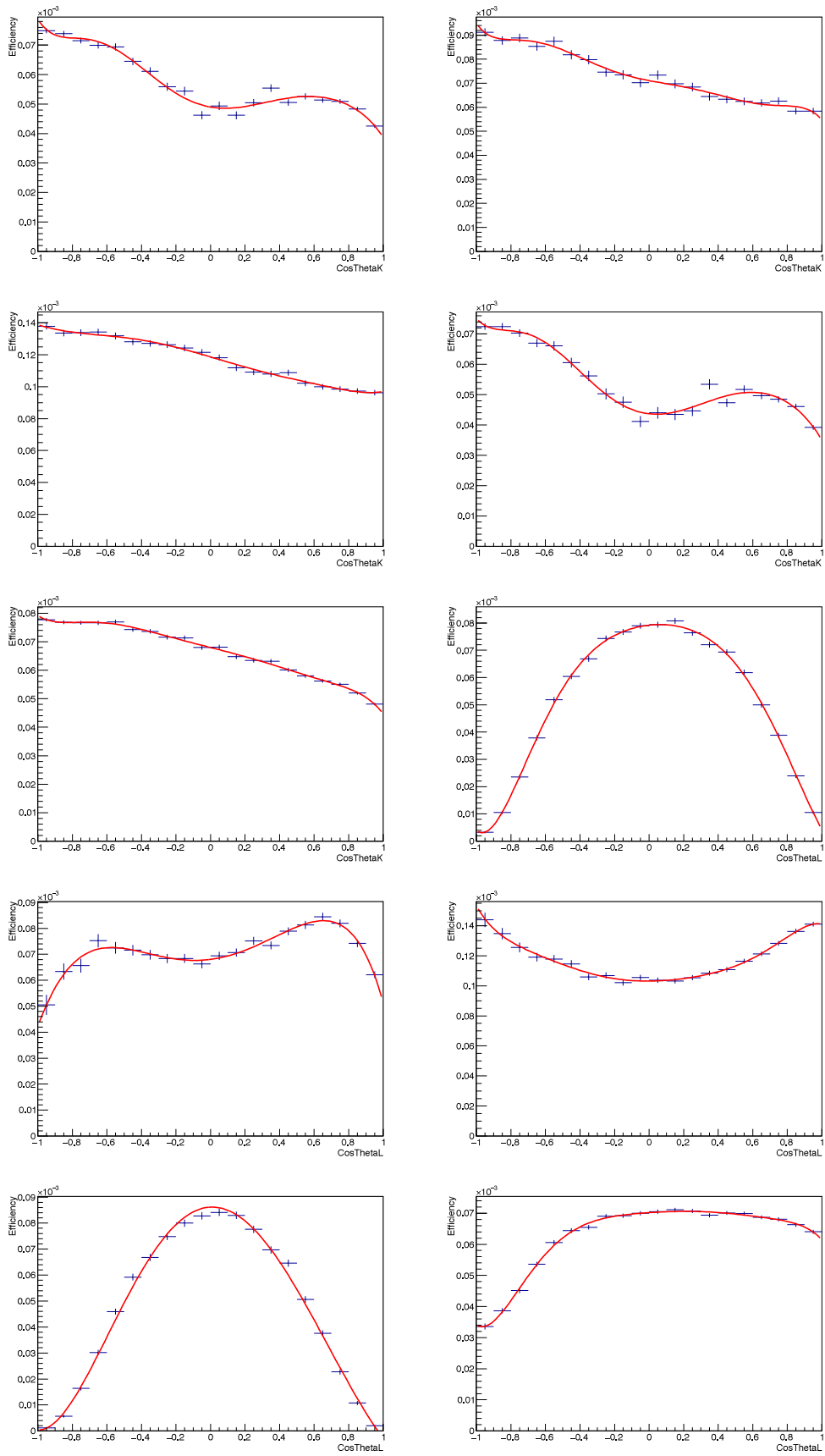
Figure 4.50: Projection of total efficiency shape fitted with alternative functions of 7th order polynomial onto $\cos\theta_K$, $\cos\theta_L$ angular axes for q^2 bins 0,2,4,5 and 6 for signal simulation and fitting results.

126

using the reconstructed and generated angular values on RECO signal sample simulation. The discrepancies are considered symmetric systematic uncertainties. The results are shown in Figure 4.51 whereas the numbers are quoted in Tables 4.8, 4.9 as "angular resolution".
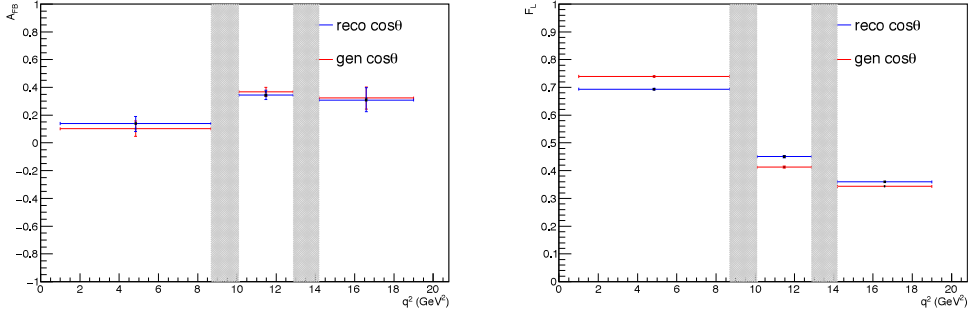
Figure 4.51: Comparison between the results obtained with reconstructed (blue) and generated (red) values of the angular variables on the RECO signal sample. The left and right plots show the values of A_{FB} and F_L as a function of dimuon mass squared(q^2). The grey shaded regions correspond to resonance regions.

4.10.5 S-P Wave Interference

Together with the decays of interest, $B^+ \to K^{*+}\mu^+\mu^-$, $B^+ \to K^{*+}J/\psi$, and $B^+ \to K^{*+}\psi'$, for which the $K_s - \pi$ are generated from the vector meson K^{*+}, there also exist counterpart decays for which the $K_s - \pi$ are not generated from such a resonance. The two cases differ with each other by the angular distribution of the decay products, in the former the $K_s - \pi$ are in a P-wave state, while in the latter the $K_s - \pi$ are in an S-wave state. To perform the measurements of the interesting variables A_{FB} and F_L which is the aim of this analysis, it is therefore in principle important to disentangle P-wave from S-wave decays. On the other hand it is known that the S-wave contribution is small with respect to the P one [52, 59], and its effect can be neglected with the current amount of data.

In order to evaluate the systematic uncertainty associated with this approach, the data are fit with the P-wave only p.d.f. and the difference of the values of F_L and A_{FB} are used as asymmetric systematic uncertainties as reported in Tables 4.8, 4.9.

Syst. err. \ q^2 bin	0	2	4	5	6
Uncorrelated systematic uncertainties					
simu. mismodel	0.0008	0.0031	0.0051	0.0020	0.0114
eff. mapping	0.0025	0.0012	0.0009	0.0000	0.0025
comb. bkg. shape	0.0438	0.0214	0.0756	0.0442	0.0194
pkg. bkg. shape	0.0000	0.0085	0.0013	0.0000	0.0197
angular resolution	0.0457	0.0378	0.0164	0.0527	0.0128
S-P wave interf.	0.0683	0.0161	0.0013	0.1862	0.0042
Total	0.0931	0.0472	0.0776	0.1985	0.0329

Table 4.8: Systematic uncertainty contributions for each q^2 bin, as from Table 4.2, for the measurement of F_L. No correlated systematic uncertainties are accounted for the measurement of this observable. The bins #1 and #3 are intended for the measurement of the control channels J/ψ and ψ'.

Syst. err. \ q^2 bin	0	2	4	5	6
Uncorrelated systematic uncertainties					
simu. mismodel	0.0702	0.0302	0.0888	0.0117	0.0433
eff. mapping	0.0040	0.0009	0.0007	0.1455	0.0280
comb. bkg. shape	0.0445	0.0578	0.0231	0.0462	0.0250
pkg. bkg. shape	0.0000	0.0064	0.0016	0.0000	0.0290
angular resolution	0.0371	0.0248	0.0142	0.0423	0.0168
S-P wave interf.	0.0596	0.0121	0.0016	0.0380	0.0027
Total	0.1089	0.0711	0.0929	0.1633	0.0664

Table 4.9: Systematic uncertainty contributions for each q^2 bin, as from Table 4.2, for the measurement of A_{FB}. No correlated systematic uncertainties are accounted for the measurement of this observable. The bins #1 and #3 are intended for the measurement of the control channels J/ψ and ψ'.

4.10.6   Total Systematic Uncertainty

The contributions from the above investigated sources of systematic uncertainties are shown in Tables 4.8, 4.9. Given the nature of the systematic uncertainties involved and the way they are investigated, the hypothesis of independence is reasonable. Hence, all contributions are added in quadrature and we obtained the total systematic uncertainties as summarized in the last rows of the tables.

q^2 bin	A_{FB}	A_{FB}(SM)	F_L	F_L(SM)
0	$0.139^{+0.296}_{-0.301} \pm 0.109$	0.077 ± 0.097	$0.407^{+0.191}_{-0.204} \pm 0.093$	0.673 ± 0.306
2	$0.127^{+0.000}_{-0.106} \pm 0.071$	N.A	$0.828^{+0.000}_{-0.248} \pm 0.047$	N.A
4	$0.415^{+0.000}_{-0.159} \pm 0.093$	0.366 ± 0.030	$0.444^{+0.001}_{-0.152} \pm 0.078$	0.346 ± 0.035
5	$-0.342^{+0.329}_{-0.173} \pm 0.163$	-0.034 ± 0.039	$0.305^{+0.000}_{-0.305} \pm 0.199$	0.716 ± 0.269
6	$0.319^{+0.000}_{-0.079} \pm 0.066$	N.A	$0.573^{+0.000}_{-0.138} \pm 0.033$	N.A

Table 4.10: Results of the measurement of the forward-backward asymmetry of the muons, A_{FB} and fraction of longitudinal polarization of the K^{*+}, F_L. In the second and fourth column are reported the fit results whereas the SM predictions are reported in third and fifth column respectively. The first error is statistical whereas the second is systematic(only uncorrelated, see Sec. 4.10 for more details).

4.11 Discussion and Conclusions

In summary, using 19.98 fb^{-1} of data recorded with the CMS detector during 2012 pp collision, the angular analysis of the decay $B^+ \rightarrow K^{*+}\mu^+\mu^-$ has been carried out. We observed around 100 signal events in the full 8 TeV data analysed and also measured the forward-backward asymmetry of the muons, A_{FB} and the fraction of longitudinal polarization of the K^{*+}, F_L as a function of the dimuon invariant mass squared, q^2. The observables A_{FB}, F_L show good agreement with the SM predictions [55–58] within the errors of the measurement.

Chapter 5

Conclusions

The standard model (SM) gives a very accurate prediction for the Branching Fraction (BF) of the $B_s \to \mu^+\mu^-$ decay and makes its measurement very sensitive to new physics. Any possible small deviation from the SM prediction allows to observe new contributions coming from New Physics (NP), thanks to the small SM theoretical uncertainty. On the other hand, the same very small SM expectation value of the BF and the huge background expected at the LHC are major challenges for the observation and the extraction of the BF measurement for this decay.

In first part of thesis we presented the first measurement of the $B_s \to \mu^+\mu^-$ BF and also the most recent upper limit of the $B_d^0 \to \mu^+\mu^-$ BF, performed with the CMS experiment at the CERN LHC. The 25 fb^{-1} sample of collected data corresponds to the total 2011 and 2012 LHC runs for pp collisions at the center-of-mass energies of 7 TeV and 8 TeV, respectively.

Signal selections and efficiencies are evaluated with Monte Carlo (MC) simulations and validated with many data-driven methods. The $B_s \to J/\psi\phi \to \mu^+\mu^-K^+K^-$ decay is used to validate the B_s MC simulation. The $B^\pm \to J/\psi K^\pm \to \mu^+\mu^-K^\pm$ decay is used as the normalization channel, to avoid a dependence on the uncertainties of the $b\bar{b}$ production cross section and luminosity measurements and to cancel out to first order many systematic un-

130

certainties related to the analysis efficiencies. Systematic effects due to the analysis and detector efficiencies are evaluated on data to be below 10%.

Different background sources can mimic the signal topology. Events in which two uncorrelated muons come from two different B decays represent the largest background, combinatorial in nature, five orders of magnitude larger than the SM expected signal yield. A Boosted Decision Tree (BDT) method is used to separate the $B^0_{s(d)}$ candidates from this combinatorial background. Variables related to the displaced secondary vertex topology and to the isolation of the muon and dimuon candidates are used to train the BDT classifier.

Rare two and three-body B decays, like $\Lambda^0_b \rightarrow pK^-$ and $B^0 \rightarrow \pi^-\mu^+\nu_\mu$, can be wrongly selected as signals due to misidentified muons. A BDT multivariate technique is used to optimize the muon identification against kaons, pions and protons, coming from these B decays, forming the rare peaking and semileptonic backgrounds. We obtained a further 50% misidentification rejection at the cost of 10% of muon efficiency, on top of the standard CMS tight muon selection. The B^0_d upper limit is extracted with a counting experiment with the CL_s method in the B^0_d invariant mass window.

The $B_s \rightarrow \mu^+\mu^-$ BF is measured with a simultaneous unbinned maximum likelihood fit on twelve independent data categories. This method allowed a 4.3σ discovery of this decay. The final $B_s \rightarrow \mu^+\mu^-$ and $B^0_d \rightarrow \mu^+\mu^-$ BF measurements and upper limits are:

$$\mathcal{B}(B_s \rightarrow \mu^+\mu^-) = (3.0^{+1.0}_{-0.9}) \times 10^{-9}$$
$$\mathcal{B}(B^0_d \rightarrow \mu^+\mu^-) \leq 1.1 \times 10^{-9} \text{ at } 95\% \text{ CL}$$

The $B_s \rightarrow \mu^+\mu^-$ branching fraction is fully compatible with the SM predictions. Its relative uncertainty, about 30%, is the most precise up-to-date and it is at the same level of the LHCb results, showing the ability of CMS to perform high precision measurements in B-physics with muons. Since the $B_s \rightarrow \mu^+\mu^-$ BF measurement does not present deviations from the SM expectation, it sets stringent limits on new physics parameters. For instance,

131

this result gives important constraints on the supersymmetry phase space, as relevant as those coming from the direct searches. New physics effects on the $B_s \to \mu^+\mu^-$ BF, if any, are small. Precise measurements of the BFs for $B_s \to \mu^+\mu^-$, $B_d^0 \to \mu^+\mu^-$ and of their ratio, have become essential to distinguish possible deviations of these decays from the SM expectations.

The CMS and LHCb measurements are statistically limited, therefore new data will improve the experimental precision for both decays, for both experiments. In this prospect, the next few years look encouraging as the CMS detector will have the possibility to collect data having integrated luminosity of hundred of inverse femtobarn. The main challenge will be the pileup. Better measurements can be obtained if the detectors will be able to live with an average of up to 140 primary vertices per bunch crossing. Under this aspect, the expected CMS upgrades, especially those for the inner tracker sub-detector, seem promising.

Given these results, the $B_s \to \mu^+\mu^-$ and $B_d^0 \to \mu^+\mu^-$ BF high precision measurements can be considered critical for the indirect searches of new physics in the next future.

In the second part of the thesis we presented the angular analysis of another FCNC (and also rare) decay $B^+ \to K^{*+}\mu^+\mu^-$ where the interesting observables A_{FB} and F_L were measured as a function of q^2 with the full 2012 data collected by CMS experiment corresponding to an integrated luminosity of $19.98 fb^{-1}$. We observed about 100 $B^+ \to K^{*+}\mu^+\mu^-$ signal events in the full 8 TeV data. The measured values of the observables were in agreement with the standard model predictions within experimental measurement errors. No indication of new physics was found.

The main challenge in the analysis was to reduce the vast amount of combinatorial background, at the same time peaking background contribution too. The main source of the combinatorial background are the wrongly reconstructed events which have the same final state particles as $B^+ \to K^{*+}\mu^+\mu^-$. The peaking background contribution are mainly coming from resonance states $B^+ \to K^{*+}J/\psi$ and $B^+ \to K^{*+}\psi'$ where the final state particles

132

are same as the signal *i.e.* $B^+ \to K^{*+}\mu^+\mu^-$ and the mother particle is also same *i.e.* B^+.

The signal selection in this analysis was based upon the few discriminating variables which were helpful in signal and background discrimination. The optimization process was performed for those variables to find out the optimal value. The whole procedure was completely data driven.

The main goal of this analysis was to measure A_{FB} and F_L in different q^2 bins. These two observables had been extracted by performing the unbinned maximum likelihood (UML) fits in each q^2 bin. The probability density function (PDF) used in the UML fit consists of the components from signal, peaking and combinatorial backgrounds. Then the fits were performed in different stages during which some components were taken from the simulation where rest were taken from the data directly. And finally the 3D fit (containing m, $\cos\theta_L$ and $\cos\theta_K$ as its three dimensions) were performed in data to extract the A_{FB} and F_L values in different q^2 bins. In this step, we have only included statistical uncertainty.

The final measurement of A_{FB} and F_L including both statistical and systematic errors were compared to the standard model predictions. Both theretical predictions and measured values agreed well within measured uncertainties.

The CMS measurements are still statistically limited, therefore we expect that the experimental precision for this decay will be improved a lot by the new data coming in Run2. In this respect, the next few years look encouraging as CMS will collect data having integrated luminosity of hundreds of inverse femtobarn.

Bibliography

[1] S. L. Glashow, Nucl. Phys. 22, 579 (1961); A. Salam and J. C. Ward, Phys. Lett. 13, 168 (1964); S. Weinberg, Phys. Rev. Lett. 19, 1264 (1967).

[2] Introduction to elementary particles - by David Griffiths.

[3] P. W. Higgs, Phys. Lett. 12, 132 (1964); P. W. Higgs, Phys. Rev. Lett. 13, 508 (1964); F. Englert and R. Brout, Phys. Rev. Lett. 13, 321 (1964).

[4] G. Aad *et al.* (ATLAS Collaboration), Phys. Lett B 716, 1 (2012); W. Adam *et al.* (CMS Collaboration), Phys. Lett B 716, 30 (2012).

[5] G. Arnison *et al.*, "Experimental Observation of Isolated Large Transverse Energy Electrons with Associated Missing Energy at $\sqrt{s}$ = 540 GeV". Phys.Lett. B122 (1983), pp. 103–116.

[6] G. Arnison *et al.*, "Experimental Observation of Lepton Pairs of Invariant Mass Around 95 GeV/c^2 at the CERN SPS Collider". Phys.Lett. B126 (1983), pp. 398–410.

[7] M. Banner *et al.*, "Observation of Single Isolated Electrons of High Transverse Momentum in Events with Missing Transverse Energy at the CERN anti-p p Collider". Phys.Lett. B122 (1983), pp. 476–485.

[8] P. Bagnaia *et al.*, "Evidence for $Z^0 \rightarrow e^+ e^-$ at the CERN anti-p p Collider". Phys.Lett. B129 (1983), pp. 130–140.

[9] S. Abachi *et al.*, "Observation of the Top Quark," Phys. Rev. Lett., vol. 74, pp. 2632–2637, 1995.

[10] A. J. Buras, J. Girrbach, D. Guadagnoli, and G. Isidori, Eur. Phys. J. C **72**, 2172 (2012)

[11] K. De Bruyn, R. Fleischer, R. Knegjens, P. Koppenburg, M. Merk, A. Pellegrino, and N. Tuning, Phys. Rev. Lett. **109**, 041801 (2012)

[12] J. R. Ellis, K. A. Olive, Y. Santoso, and V. C. Spanos, J. High Energy Phys. **05** (2006) 063.

[13] S. Davidson and S. Descotes-Genon, J. High Energy Phys. **11** (2010) 073

[14] S. R. Choudhury, A. S. Cornell, N. Gaur, and G. C. Joshi, Int. J. Mod. Phys. A **21**, 2617 (2006).

[15] J. K. Parry, Nucl. Phys. B **760**, 38 (2007)

[16] J. R. Ellis, J. S. Lee, and A. Pilaftsis, Phys. Rev. D **76**, 115011 (2007)

[17] "The LHC Design Report v.1: the LHC Main Ring", CERN-2004-003-V-1 `http://cdsweb.cern.ch/record/782076`.

[18] ALICE Collaboration, "Technical Proposal for a Large Ion Collider Experiment at the CERN LHC", CERN-LHCC-95-71 (1995).

[19] ATLAS Collaboration, "Detector and Physics Performance Technical Design Report, vol. 1", CERN-LHCC-99-14 (1999).

[20] R. Adolphi *et al.* (CMS Collaboration), "The CMS experiment at the CERN LHC", JINST 0803:S08004, (2008).

[21] LHCb Collaboration, "LHCb Technical Proposal", CERN-LHCC-98-04 (1998).

[22] CMS collaboration, "Physics Technical Design Report", Volume I : Detector Performance and software, CMS/LHCC 2006-001, CMS TDR 8.1.

[23] CMS collaboration, "Physics Technical Design Report", Volume II : Physics performance, CMS/LHCC 2006-021, CMS TDR 8.2.

[24] C. Seez, "The CMS trigger system", Eur Phys J C 34, s01, s151–s159 (2004).

[25] The CMS Offline Workbook `https://twiki.cern.ch/twiki/bin/view/CMSPublic/WorkBook`.

[26] R. Aaij *et al.*, "Measurement of the fragmentation fraction ratio f_s/f_d and its dependence on B meson kinematics", JHEP **04** (2013) 001

[27] J. Beringer *et al.*, "Review of Particle Physics (RPP)". Phys. Rev. D **86** (2012) 010001

[28] CMS collaboration, "CMS Luminosity Based on Pixel Cluster Counting", CMS-PAS-LUM-13-001

[29] CMS collaboration, "Tracking and Vertexing Results from First Collisions", CMS-PAS-TRK-10-001

[30] A. Hoecker *et al.*, "TMVA - Toolkit for Multivariate Data Analysis", PoS ACAT:040, 2007

[31] A.L. Read. "Modified frequentist analysis of search results (The CL_s method)". CERN-OPEN-2000-205 (2000)

[32] S.S. Wilks. "The Large-Sample Distribution of the Likelihood Ratio for Testing Composite Hypotheses". Annals Math.Statist. 9.1 (1938), pp. 60–62.

[33] R. Aaij *et al.* [LHCb Collaboration], "Updated average f_s/f_d b-hadron production fraction ratio for 7 TeV pp collisions", LHCb-CONF-2013-011.

[34] R. Aaij *et al.* [LHCb Collaboration], "Measurement of the $B_s \to \mu^+\mu^-$ branching fraction and search for $B_d^0 \to \mu^+\mu^-$ decays at the LHCb experiment", Phys.Rev.Lett. 111 (2013), p.101805.

[35] V. Khachatryan *et al.* [CMS and LHCb Collaborations], "Observation of the rare $B_s^0 \to \mu^+\mu^-$ decay from the combined analysis of CMS and LHCb data", Nature 522, 68 (2015).

[36] A. Ali, T. Mannel, and T. Morozumi, "Forward-Backward asymmetry of dilepton angular distribution in the decay $b \to s\ell^+\ell^-$", Phys. Lett. B **273** (1991) 505-512

[37] U. Egede, "Angular correlations in the $\overline{B}^0 \to \overline{K}^{*0}\mu^+\mu^-$ decay", CERN-LHCb-057 (2007)

[38] A. Ali, G. Kramer, and G-.h. Zhu, "$B \to K^*\ell^+\ell^-$ in soft-collinear-effective-theory", Eur. Phys. J. C **47** (2006) 625-641

[39] C. Bobeth, G. Hiller, and G. Piranishvili, "CP asymmetries in $B^0 \to \overline{K}^*(\to \overline{K}\pi)\overline{\ell}\ell$ and untagged $\overline{B}_s$, $B_s \to \phi(\to K^+K^-)\overline{\ell}\ell$", JHEP **07** (2008) 106

[40] A. Khodjamirian, T. Mannel, A.A. Pivovarov, Y.-M. Wang, "Charm-loop effect in $B \to K^{(*)}\ell^+\ell^-$ and $B \to K^*\gamma$", arXiv: 1006.4945 [hep-ph]

[41] C. Bobeth, G. Hiller, and D. van Dyk, "The benefits of $B \to K^*\ell^+\ell^-$ decays at low recoil", arXiv: 1006.5013 [hep-ph]

[42] C. Bobeth, G. Hiller, D. van Dyk, and C. Wacker, "The decay $B \to K\ell^+\ell^-$ at low hadronic recoil and model-independent delta $B = 1$ constraints", arXiv: 1111.2558 [hep-ph]

[43] B. Aubert *et al.*, "Angular distributions in the decays $B \to K^*\ell^+\ell^-$", Phys. Rev. D **79** (2009) 031102

[44] J.T. Wei *et al.*, "Measurement of the differential branching fraction and forward-backward asymmetry for $B \to K^{(*)}\ell^+\ell^-$", Phys. Rev. Lett. **103** (2009) 171801

[45] T. Aaltonen *et al.*, "Measurements of the angular distributions in the decays B → K(*)$\mu^+\mu^-$ at CDF", Phys. Rev. Lett. **108** (2012) 081807

[46] S. Chatrchyan *et al.*, "The CMS experiment at the CERN LHC", JINST **3** (2008) S08004

[47] S. Chatrchyan *et al.*, "CMS Absolute calibration of the luminosity measurement at CMS: winter 2012", CMS-PAS-SMP-12-008

[48] E. Barberio, and Z. Was, "Photos - a universal Monte Carlo for QED radiative corrections in decays", CERN-TH-7033-93 (1993)

[49] GEANT4 Collaboration, "GEANT4 — a simulation toolkit", Nucl. Instrum. Meth. A **506** (2003) 250-303

[50] CMS Collaboration, "Angular analysis of the decay $B^0 \to K^{*0}\mu^+\mu^-$ from pp collisions at $\sqrt{s} = 8$ TeV", Phys. Lett. B **753** (2016) 424-448

[51] CMS Collaboration, "Measurement of the B^+ production cross-section in pp collisions at $\sqrt{s} = 7\ TeV$", Phys.Rev.Lett. **106** (2011) 112001

[52] T. Blake, U. Egede, and A. Shires, "The effect of S-wave interference on the $B^0 \to K^{*0}\ell^+\ell^-$ angular observables", JHEP **03** (2013) 027

[53] F. James, and M. Winklerc, "MINUIT user's guide", `http://seal.web.cern.ch/seal/work-packages/mathlibs/minuit/doc/doc.html`

[54] Feldman, Gary J. and Cousins, Robert D., "A Unified approach to the classical statistical analysis of small signals", Phys. Rev. D **57** (1998) 3873-3889

[55] S. Descotes-Genon, L. Hofer, J. Matias and J. Virto, "Global analysis of $b \to s\ell\ell$ anomalies", JHEP **06** (2016) 092

[56] S. Descotes-Genon, L. Hofer, J. Matias and J. Virto, "On the impact of power corrections in the prediction of $B \to K^*\mu^+\mu^-$ observables", JHEP **12** (2014) 125

[57] S. Descotes-Genon, J. Matias and J. Virto, "Understanding the $B \to K^* \mu^+ \mu^-$ Anomaly", Phys. Rev. D **88** (2013) 074002

[58] S. Descotes-Genon, J. Matias, M. Ramon and J. Virto, "Implications from clean observables for the binned analysis of $B \to K^* \mu^+ \mu^-$ at large recoil", JHEP **01** (2013) 048

[59] B. Aubert *et al.*, "Measurement of decay amplitudes of B $\to J/\psi$ K*, $\psi(2S)$K*, and χ_{c1}K* with an angular analysis", Phys. Rev. D **76** (2007) 031102